UC San Diego
UC San Diego Electronic Theses and Dissertations

Title

Electron transport and plasmons in Dirac materials and in two-dimensional materials

Permalink

https://escholarship.org/uc/item/0sc8h6cq

Author

Wu, Jhih-Sheng

Publication Date

2016

Peer reviewed|Thesis/dissertation

UNIVERSITY OF CALIFORNIA, SAN DIEGO

**Electron transport and plasmons in Dirac materials and in
two-dimensional materials**

A dissertation submitted in partial satisfaction of the
requirements for the degree
Doctor of Philosphy

in

Physics

by

Jhih-Sheng Wu

Committee in charge:

Professor Michael Fogler, Chair
Professor Dimitri Basov
Professor Shaya Fainman
Professor Michael Holst
Professor Congjun Wu

2016

The Dissertation of Jhih-Sheng Wu is approved, and
it is acceptable in quality and form for publication on
microfilm and electronically:

_____

_____

_____

_____

_____

Chair

University of California, San Diego

2016

DEDICATION

To my parents, Feng-Chu and Gui-Tian, for their endless support for my persuit of

being a sceintist.

EPIGRAPH

"Make the best efforts with a beautiful mind."

—anonymous

TABLE OF CONTENTS

LIST OF FIGURES

ACKNOWLEDGEMENTS

First, I would like to acknowledge my advisor Professor Michael Fogler for his guidance in this dissertation. He has put much effort in introducing interesting physics, sharpening my skills, writing papers and accessing important problems. I am glad to learn from him through the past five years.

I also want to thank Prof. Dimitri Basov, with whom we have the joint group meeting every Friday. The Friday meeting brought up people from both the theoretical and experimental groups, talking and discussing fascinating physics in the aspect of near-field optics. I have learned so much from every talk by our experimental friends, which also played an important role in the direction of my dissertation. The collaborations ended up with the fruitful results. With Ted, we had theoretical analyzed the collective superfluid excitations and proposed the imaging method. With Kirk, we had analyzed the optical response of the surface states of a topological insulators. With Guangxin, we had explained how the graphene plasmon propagation is affected by the Moiré patterns.

I want to thank my friends, whom I met in San Diego. Hung-Wei and Yen-Shan took care of me when I first arrived in the States. During these years, Yen-Shan and Guannan helped me a lot in taking me to many places. My roommates and I lived together for the past four years, during which we had fun in the party with the hot pots and the board games, cheered each others and shared the big moments in our life. My basketball friends and I enjoyed playing basketball every Sunday, which released my pressure much. I want to thank our department staffs, especially Sharmila, who is always kind and heartwarming. She cares the international students and has helped me a lot.

I want to express my heartfelt gratitude to my family. My parents always love and support me in pursuing my degree. They give me the greatest strength whenever I have difficulty. They often warm my heart as they show their care from oversea. I want to thank my sisters for their encouragements and supports. I am grateful and fortunate to have met my girlfriend, Jiadi, at the end of my PhD life, who has been by my side.

VITA

2006	B.S., in Physics, National Taiwan University
2010	M.S., in Physics, National Taiwan University
2016	Ph.D., in Physics, University of California, San Diego

PUBLICATIONS

- Fei, Zhe; Goldflam, Michael; **Wu, Jhih-Sheng**; Dai, Siyuan; Wagner, Martin; McLeod, Alex; Liu, Mengkun; Post, Kirk; Zhu, Shou-En; Janssen, Guido; Fogler, Michael; Basov, Dimitri, *Edge plasmons and plane plasmons in graphene nanoribbons"*, Nano Lett., 2015, 15 (12), pp 82718276

- **Jhih-Sheng Wu**, D. N. Basov, and M. M. Fogler, *Topological insulators are tunable waveguides for hyperbolic polaritons*, Phys. Rev. B 92, 205430 (2015)

- G. X. Ni, H. Wang, **J. S. Wu**, Z. Fei, M. D. Goldflam, F. Keilmann, B. Özyilmaz, A. H. Castro Neto, X. Xie, M. M. Fogler, D. N. Basov, *Plasmons in Graphene Moiré Superlattices*, Nature Materials 14, 12171222 (2015)

- K. W. Post, B. C. Chapler, M. K. Liu, **J. S. Wu**, H. T. Stinson, M. D. Goldflam, A. R. Richardella, J. S. Lee, A. A. Reijnders, K. S. Burch, M. M. Fogler, N. Samarth, and D. N. Basov, *Sum-rule constraints on the surface state conductance of topological insulators*, Phys. Rev. Lett. 115, 116804 (2015)

- **Jhih-Sheng Wu** and Michael M. Fogler, *Scattering of two-dimensional massless Dirac electrons by a circular potential barrier*, Phys. Rev. B 90, 235402 (2014)

- H. T. Stinson, **J. S. Wu**, B. Y. Jiang, Z. Fei, A. S. Rodin, B. C. Chapler, A. S. McLeod, A. Castro Neto, Y. S. Lee, M. M. Fogler, and D. N. Basov, *Infrared nanospectroscopy and imaging of collective superfluid excitations in anisotropic superconductors*, Phys. Rev. B 90, 014502 (2014)

- Jian-Yuan Chang, **Jhih-Sheng Wu**, and Ching-Ray Chang, *Exact Hamiltonians with Rashba and cubic Dresselhaus spin-orbit couplings on a curved surface*, Phys. Rev. B 87, 174413, (2013)

- Ming-Hao Liu, **Jhih-Sheng Wu**, Son-Hsien Chen, and Ching-Ray Chang, *Spin and charge transport in U-shaped one-dimensional channels with spin-orbit couplings*, Phys. Rev. B 84, 085307 (2011)

ABSTRACT OF THE DISSERTATION

**Electron transport and plasmons in Dirac materials and in
two-dimensional materials**

by

Jhih-Sheng Wu

Doctor of Philosphy in Physics

University of California, San Diego, 2016

Professor Michael Fogler, Chair

Two-dimensional materials are one-atom-thick crystals, which are stable under
ambient conditions. Heterostructures by stacking of two-dimensional (2D) crystals
via the van der Waals force provide a versatile platform for investigation of emergent
properties of composite materials. In this thesis, I studied three 2D materials, graphene,
Bi_2Se_3 and hexagonal boron nitride (hBN), of which the first two materials host 2D
Dirac fermions. The core of this thesis is to study the transport and optical properties
of 2D Dirac fermions interacted with their three-dimensional (3D) environments.

In Chapter 2, we consider electron transport of graphene, adsorbing clusters

of charged impurities. We model the clusters as circular barriers. We calculate the differential, total, and transport cross-sections for scattering of two-dimensional massless Dirac electrons by a circular barrier. For scatterer of a small radius, the cross-sections are dominated by quantum effects such as resonant scattering that can be computed using the partial-wave series. Scattering by larger size barriers is better described within the classical picture of reflection and refraction of rays, which leads to phenomena of caustics, rainbow, and critical scattering. Refraction can be negative if the potential of the scatterer is repulsive, so that a p-n junction forms at its boundary. Qualitative differences of this case from the n-N doping case are examined. Quantum interference effects beyond the classical ray picture are also considered, such as normal and anomalous diffraction, and also whispering-gallery resonances. Implications of these results for transport and scanned-probe experiments in graphene and topological insulators are discussed.

In Chapter 3, we consider how the Dirac plasmons of Bi_2Se_3 are coupled with its phonon polaritons. Layered topological insulators, for example, Bi_2Se_3 are optically hyperbolic materials in a range of THz frequencies. Such materials possess deeply subdiffractional, highly directional collective modes: hyperbolic phonon-polaritons. In thin crystals the dispersion of such modes is split into discrete subbands and is strongly influenced by electron surface states. If the surface states are doped, then hybrid collective modes result from coupling of the phonon-polaritons with surface plasmons. The strength of the hybridization can be controlled by an external gate that varies the chemical potential of the surface states. Momentum-dependence of the plasmon-phonon coupling leads to a polaritonic analog of the Goos-Hänchen effect. Directionality of the polaritonic rays and their tunable Goos-Hänchen shift are

observable via THz nanoimaging.

Chapter 1

Overview and introduction

Two-dimensional (2D) materials have attracted tremendous research interests in both fundamental science and application during the past decade [GG13, NMCCN16] since the isolation of graphene in 2004 by the Nobel Laureates Andre Geim and Konstantin Novoselov. The graphene-related studies lead to ten thousands papers every year. Although 'simple graphene' has been well studied and explored, composite materials by stacking of different 2D crystals bring up abundant new research directions. On the other hand, many of 2D materials, such as graphene and Bi_2Se_3 appear to be described by Dirac fermions. The materials, having Dirac nodes in the spectrum, are called "Dirac materials", which share many universal properties.[WBSB14] This thesis focuses on the transport and optical properties of 2D Dirac fermions interacted with their three-dimensional environments, which hopefully shed light on understanding composite materials of 2D crystals.

1.1　2D Dirac fermions and plasmons

In 2D, the Dirac Hamiltonian has the form

$$H_D = v\boldsymbol{\sigma} \cdot \boldsymbol{p} + m\sigma_z, \tag{1.1}$$

where $\boldsymbol{\sigma} = (\sigma_x, \sigma_y)$ and σ_z are the Pauli matrices. The term $m\sigma_z$ gives rise to a gap of $2m$ in the sprectrum. Quasiparticles described by this Hamiltonian are called "Dirac fermons". More and more condensed matter systems are found to be described by the Hamiltonian (see Table 1 of [WBSB14]). In the context of condensed matters, the velocity v is the Fermi velocity v_F.

In the case of $m = 0$, the Hamiltonian has a linear and gapless sprectrum, which results in distinct physical properties compared with those materials of parabolic bands. The peculiarities of Driac fermions are attributed to the two features: (i) spinor and (ii) constant velocity, regardless of Fermi energy. For example, the momentum is locked to the spin, that is, the direction of momentum determines the allowed spin. Such spin-momentum locking leads to the famous Klein tunneling, which states that there is no back scattering for a massless Dirac fermion encountering a barrier. Due to the spinor structure, it is inevitable to introduce the Berry phase in order to describe the quasiparticles semiclassically. In Chapter 2, we use the ray picture, incorporating the Berry phase, to understand scattering of Dirac fermions by a large charged cluster. We also discuss the regimes where the ray picture is not valid.

Plasmons are the collective modes of charged particles due to their Coulomb interactions. Due to the gapless spectrum, the Coulomb interactions can occur via two channels: (i) the intraband electron-hole excitations and (ii) the interband electron-
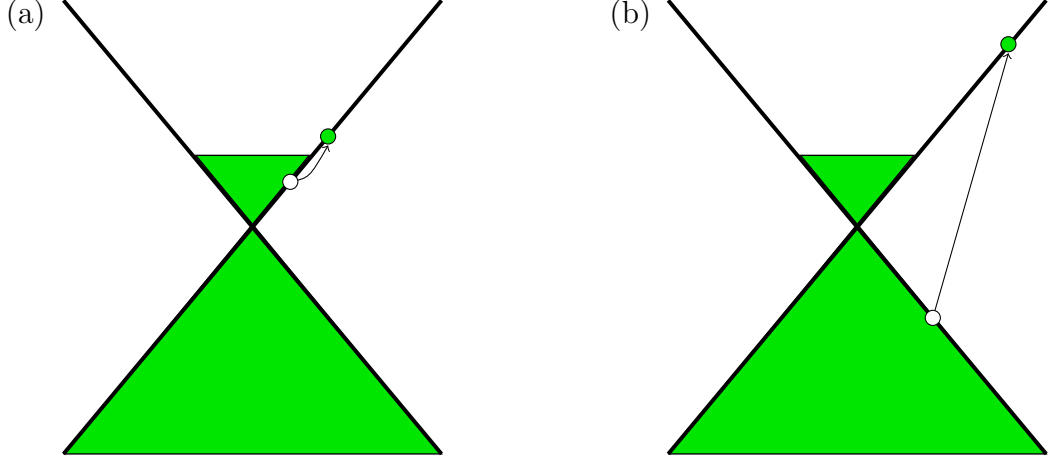
Figure 1.1: Electron-hole excitations of Dirac fermions via (a) the intraband transition and (b) the interband transition.

hole excitations (Fig. 1.1). These electron-hole excitations create a dynamic and nonlocal dielectric function $\epsilon(q, \omega)$. The relation between the dielectric function $\epsilon(q, \omega)$ and the 2D conductivity $\sigma(q, \omega)$ is

$$\epsilon(q, \omega) = 1 + \frac{2\pi i q \sigma(q, \omega)}{\kappa(q, \omega)\omega}, \tag{1.2}$$

where $\kappa(q, \omega)$ is the effective dielectric function of the 3D environment. The plasmon dispersions are given by solving $\epsilon(q, \omega) = 0$. Without considering $\kappa(q, \omega)$ and in the small q limit, the conductivity $\sigma(q, \omega)$ is of the Drude form, and the plasmon has the typical dispersion of 2D electron gas, $\omega \sim \sqrt{q}$. The role of $\kappa(q, \omega)$ is to modify the Coulomb interation between 2D Dirac fermions. In Chapter 3, we study the case, where $\kappa(q, \omega)$ arises from the anisotropic optical phonons of Bi_2Se_3 and hBN. We show that the interplay between Dirac plasmons and the phonon polaritons is analogous to the optical phenomenon, "Goos-Hächen effect".
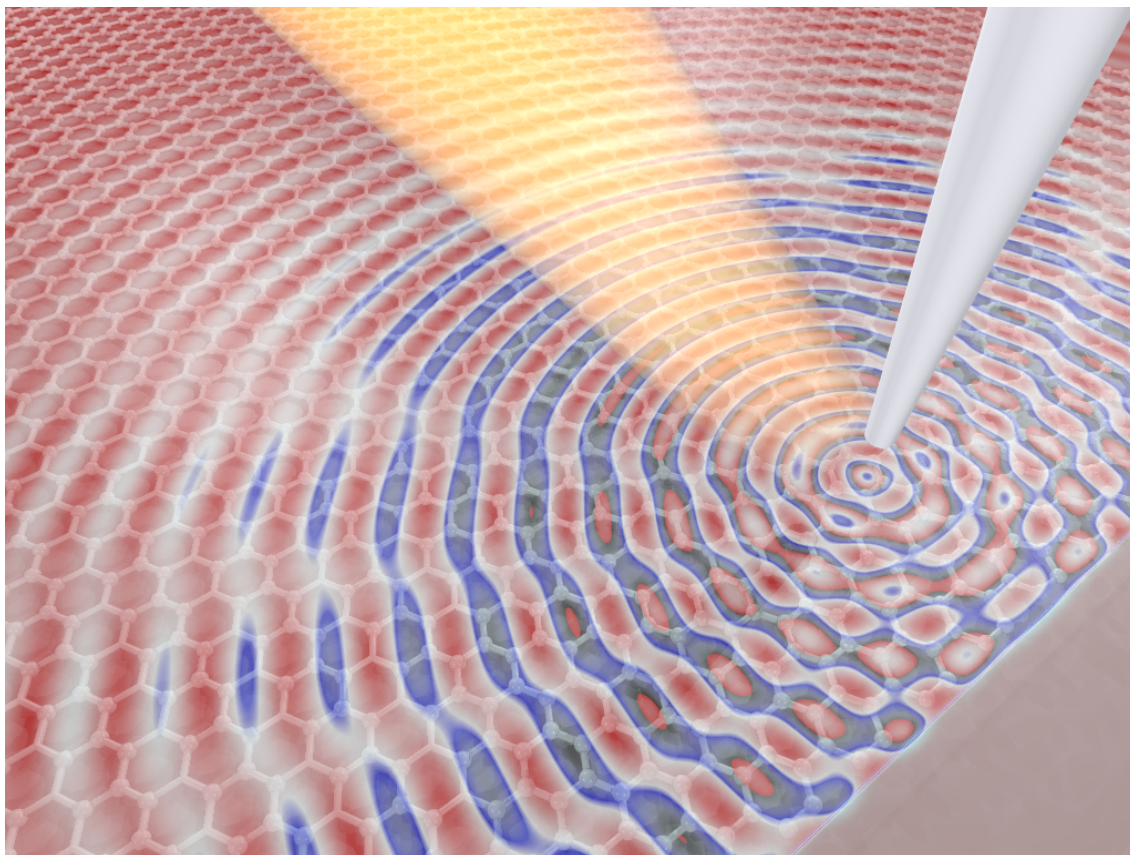
Figure 1.2: Artistic diagram of how to experiemntally launch Dirac plasmons by scattering-type near-field optical microscopy, where light is scattered by a metalic tip.

Chapter 2

Scattering of two-dimensional massless Dirac electrons by a circular potential barrier

2.1 Introduction

Recently, much interest has been attracted by electronic properties of materials where quasiparticles behave as massless two-dimensional (2D) Dirac fermions. Examples of such materials include graphene [CNGP+09] and surface states of topological insulators. [FKM07, HK10] Graphene has been studied more extensively because of advances in sample fabrication and a number of exceptional virtues, including a wide tunability of doping level and superior transport properties. The latter are characterized by mean-free paths approaching several microns and the corresponding transport times τ_{tr} in the range of picoseconds. [CNGP+09, Per10, DSAHR11, BFL+14a] However, scattering mechanisms limiting the transport mobility of graphene are still not

fully understood. For instance, a weak dependence of the mobility on the impurity density found in some experiments [SGM$^+$07] remains an open problem. It was argued that this weak dependence could be due to correlations in impurity positions. Both negative, i.e., repulsive [LHRDS11] and positive, i.e., attractive correlations could impact the mobility. An example of the latter is aggregation of impurities into clusters of size of tens of nanometers. Modelled as circularly symmetric potential barriers with sharp boundaries, such finite-size scatterers were predicted [KGG09] to degrade the mobility much less compared to random uncorrelated impurities. Another observable signature of finite-size scatterers is a significant difference between the transport time τ_{tr} and the quantum lifetime τ_q. (The latter can be extracted from magnetotransport measurements.) Although the ratio

$$\eta \equiv \tau_{\mathrm{tr}}/\tau_q \qquad (2.1)$$

varies widely among different experiments, it can be as high as a factor of six. [Gor09] For massive 2D fermions scattered by random sharp barriers, η should approach $3/2$ when the barriers become impenetrable. [YM07] Since graphene quasiparticles behave as massless fermions, they can penetrate arbitrary high potential barriers (lower than the total energy bandwidth) via the process of Klein's tunneling and associated negative refraction. [KNG06, CFA07, CPP07] Therefore, the dependence of η on the barrier parameters is another open problem. For these and other reasons, scattering of quasiparticles by finite-size defects warrants further qualitative and quantitative investigation in order to better understand transport and magnetotransport properties of graphene. While there have been already a number of previous studies of circular potential barriers in graphene, [KN07, CPP07, Gui08, MP08, HA08, BTB09, KGG09,
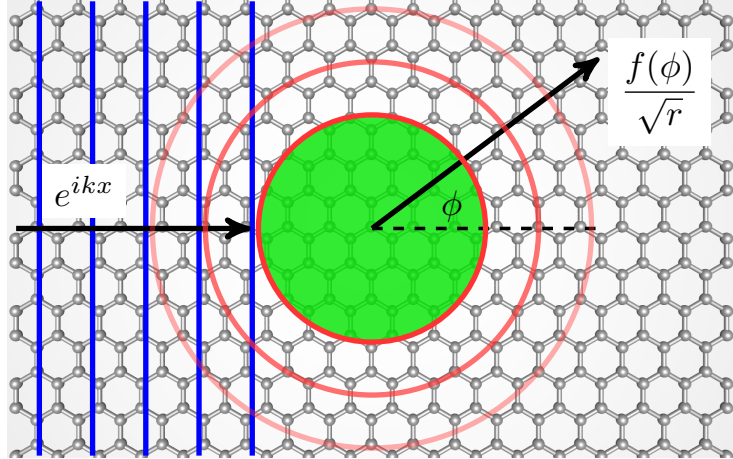
Figure 2.1: (Color online) Electron plane wave scattered by a circularly symmetric step-like potential in a Dirac metal such as graphene or a surface of a topological insulator.

HBF13] they have not elucidated in a comprehensive way how scattering by such a barrier depends on its size and strength. Furthermore, some of this prior work contains minor errors. In this paper, we correct, refine, and extend these investigations.

The question of what limits the surface electron conduction in topological insulators is even more wide open. There are few studies that examined scattering of Dirac fermions by circular potential barriers in this context although other types of scattering defects have been considered. [PLV$^+$11, FZWL11, PCG$^+$14] Most of our results for this problem should also apply to Dirac fermions at the surface of topological insulators.

The effective low-energy Hamiltonian of the model we study is [KN07, CPP07, Gui08, MP08, HA08, BTB09, KGG09, HBF13]

$$H = v_F \left(\sigma_x p_x + \sigma_y p_y \right) + V(r) , \qquad (2.2)$$

where p_ν are the momentum operators, σ_ν are the Pauli matrices, and $v_F \sim 10^8$ cm/s
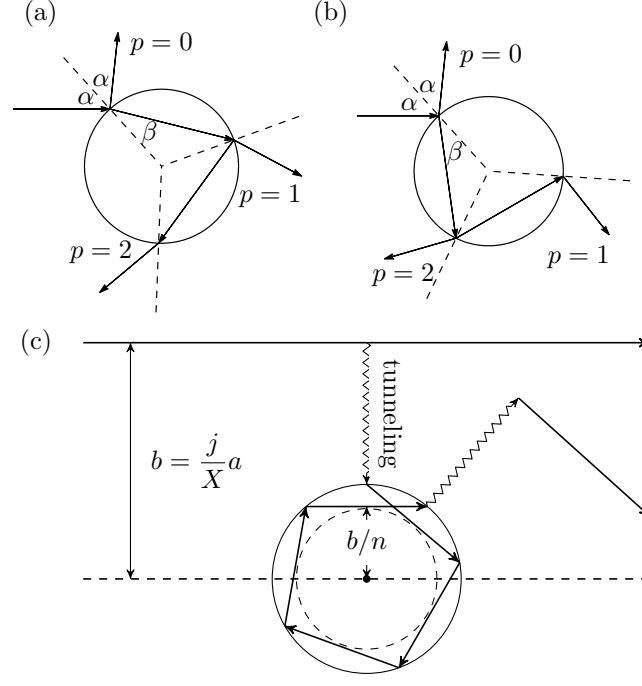
Figure 2.2: (a) The first three rays $p = 0$, 1, 2 in the ray series for an n-N junction (b) Same for an n-p junction. (c) Ray tunneling and a whispering gallery mode inside the scatterer.

is the Fermi velocity. The potential $V(r)$ is assumed to be step-like,

$$V(r) = V_0 \, \theta(a - r), \tag{2.3}$$

where $\theta(r)$ is the unit step function and a is the radius of the disk. The scattering of an electron with energy $E > 0$ by this potential is characterized by two dimensionless parameters,

$$X = \frac{Ea}{\hbar v_F} \equiv ka \quad \text{and} \quad \rho = -\frac{V_0 a}{\hbar v_F}, \tag{2.4}$$

which specify the size and the strength of the barrier, respectively; X also gives an estimate of the maximum angular momentum involved in the scattering.

Consider a plane wave incident on the scatterer. The problem is to find the far-field scattering amplitude $f(\phi)$ as a function of the deflection angle ϕ, see Fig. 2.1. The differential cross-section is then calculated from

$$\frac{d\sigma}{d\phi} = |f(\phi)|^2 \,. \tag{2.5}$$

The formal solution of this problem is given by the standard partial-wave decomposition (PWD)

$$f(\phi) = -\frac{i}{\sqrt{2\pi k}} \sum_j \left(e^{2i\delta_j} - 1\right) e^{i(j-1/2)\phi}, \tag{2.6}$$

where δ_j is the phase shift for angular momentum j. The well-known peculiarity of Dirac fermions is that j's are not integers but half-integers, see Appendix 2.8.

Integrating the differential cross-section over ϕ, we can express the total and the transport cross-sections in terms of the phase shifts [SKL07]

$$\sigma = \frac{4}{k} \sum_j \sin^2 \delta_j \,, \tag{2.7}$$

$$\sigma_{\mathrm{tr}} = \frac{4}{k} \sum_{j>0} \sin^2(\delta_{j+1} - \delta_j) \,. \tag{2.8}$$

The total cross-section obeys the optical theorem

$$\sigma = \sqrt{\frac{8\pi}{k}} \, \mathrm{Im} f(0) \,. \tag{2.9}$$

For $X \ll 1$ the PWD is dominated by a first few terms and the result has an intuitive interpretation in terms of resonant scattering. Conversely, for $X \gg 1$, PWD suffers

from slow convergence and lacks a transparent physical meaning. In fact, it appears that numerical results reported in a previous work on this problem [KGG09] are inaccurate [See the second paragraph below Eq. (2.25).]. The main effort in this paper is devoted to treating this difficult $X \gg 1$ regime by alternative methods. Especially instructive one is the semiclassical approximation. This approach leads to the so-called ray series, which accounts for most of the observable features of the $X \gg 1$ regime and has an intuitive representation in terms of ray paths (Fig. 2.2). In this context it is convenient to introduce another dimensionless parameter, the refractive index:

$$n = \frac{X'}{X} = 1 + \frac{\rho}{X},$$ (2.10)

where X' is defined as

$$X' \equiv X + \rho.$$ (2.11)

The refractive index n can be of either sign. If it is positive (negative), we deal with, respectively, n–N and n-p junction at $r = a$. In the latter case, realized for $\rho < -X$, the Dirac quasiparticles exhibit the aforementioned negative refraction.[CFA07] This modifies the ray trajectories qualitatively,[CPP07] cf. Figs. 2.2(a) and 2.2(b) and Sec. 2.3.

The remainder of the paper is organized as follows. In Sec. 2.2 we classify the regimes of scattering according to X and ρ. We present the global regime diagram (Fig. 2.3) and give the formulas for the cross-sections in each regime. We find the most feature-rich case to be $X \gg 1$. In Sec. 2.3, we study this case using the semiclassical method. In Sec. 2.4, we discuss phenomena beyond the semiclassical approximation.
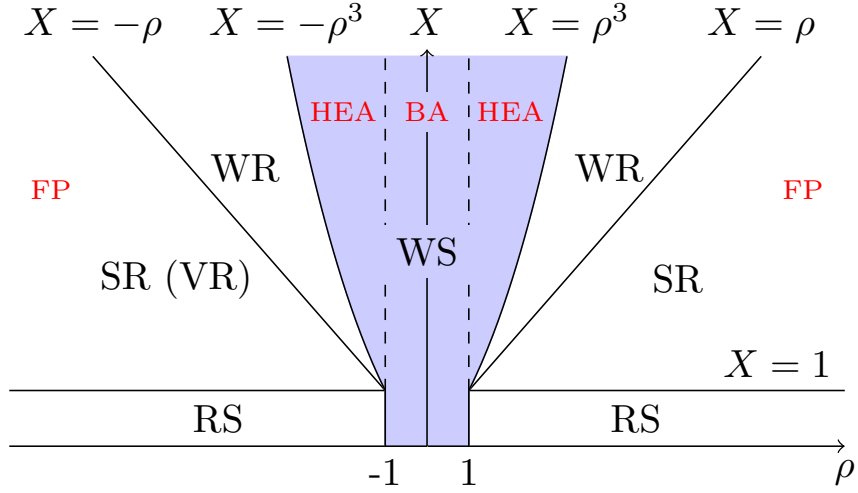
Figure 2.3: (Color online) Regime diagram of the scattering. RS: resonant scatterer, SR: strong reflector, FP: Fabry-Pérot resonator, WR: weak reflector, WS: weak scatterer, HEA: high energy approximation, BA: Born approximation. VR: Veselago reflector, where negative refraction occurs.

In Sec. 2.5, the angular dependence of the differential cross-section in various large-X regimes is analyzed. Besides far-field scattering, we also consider the structure of the electron wavefunctions near the scatterer. In Sec. 2.6, we briefly discuss implications of these near-field effects for scanned-probe experiments with graphene and topological insulators. In Sec. 2.7, we summarize our contributions and comment on possible future extensions of our study. The general outline of our analytical derivations is presented in Secs. 2.3–2.5, with the additional details provided in the Appendices.

2.2 Main results

We start with a brief overview of different scattering regimes indicated in Fig. 2.3. These regimes are classified according to the behavior of the cross-sections as functions of X and ρ. The horizontal line $X = 1$ partitions Fig. 2.3 into two domains. In the upper one, $X \gg 1$, the scattering has a predominantly semiclassical character.

Except for the region of small deflection angles $\phi < 1/X$, which is governed by diffraction, the scattering amplitude is obtained by summing the ray series (Fig. 2.2), expressed mathematically by the Debye expansion. [Nus69, Gra00] In the lower domain, $X \ll 1$, scattering is dictated by quantum effects and the ray picture generally does not apply.

In the strong reflector (SR) and weak reflector (WR) regimes of Fig. 2.3, the interference between the rays and the diffraction can be neglected. As a consequence of the Babinet principle, each of the two contributes $2a$ to the total cross-section,[YM07] and so the total cross-section is

$$\sigma \simeq 4a \quad \text{(SR and WR regimes)} . \tag{2.12}$$

In contrast, in the weak scatterer (WS) regime of Fig. 2.3, where most of the rays are scattered by small angles, the interference of the ray and diffraction amplitudes becomes important. In this "anomalous diffraction" (AD) regime [vdH57] the ray picture fails. Instead, the scattering can be dealt with the perturbation theory, such as the high energy approximation (HEA) and the Born approximation (BA). As discussed below, Eq. (2.12) becomes replaced by more complicated expressions, Eqs. (2.17a) and (2.20), that predict oscillations of σ as a function of ρ. The BA in fact describes the entire $|\rho| \ll 1$ strip in Fig. 2.3, including the $X \ll 1$ part.

In the rest of the quantum domain $X \ll 1$, $|\rho| \gg 1$, the cross-sections σ and σ_{tr} are determined by resonant scattering (RS), see Fig. 2.3. These cross-sections can be efficiently computed by summing the partial-wave series, Eqs. (2.7) and (2.8). Unlike the $|\rho| \ll 1$ case, where the lowest angular momenta [KN07] $j = \pm 1/2$ dominate, here significant contributions arise from certain high j for which the resonant tunneling
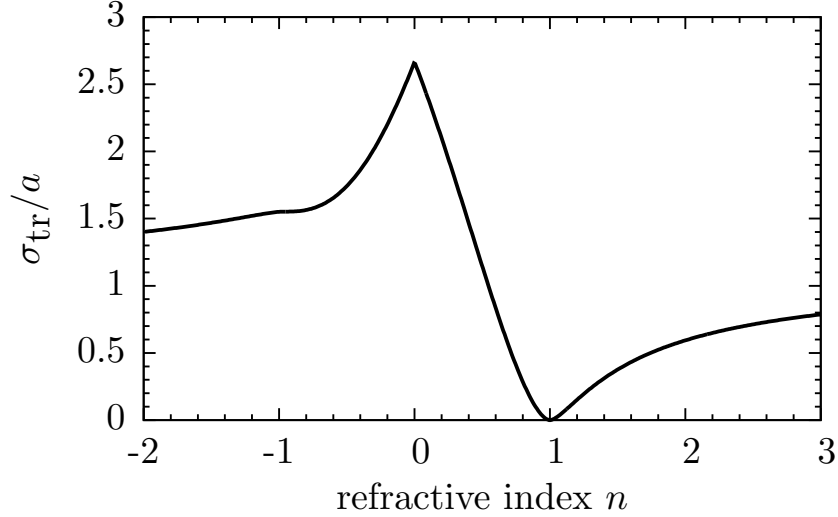
Figure 2.4: Analytical approximation [Eq. (2.13)] for the transport cross-section as a function of the refractive index.

condition is satisfied.

Let us now give more detailed information about each of the regimes. The transport cross-sections in the SR and WR regimes are dominated by the ray series, since the diffraction is restricted to small angles. Neglecting interference among different rays, we obtained the result

$$\frac{\sigma_{\text{tr}}}{a} = \frac{8}{3} - \text{sgn}(n)\varsigma(n)\,, \tag{2.13}$$

$$\varsigma(n) = 4 \int\limits_{0}^{\min(1,|n|)} db \frac{(2n-1)b^2 - n}{n^2 - (2n-1)b^2} \sqrt{n^2 - b^2}\sqrt{1 - b^2} \tag{2.14}$$

(SR and WR regimes).

The correction term $\varsigma(n)$ can also be written as a linear combination of the complete elliptical integrals, see Sec. 2.3. Equation (2.13) predicts the following asymptotic

behavior of the transport cross-section:

$$\frac{\sigma_{\text{tr}}}{a} \simeq \begin{cases} 3(n-1)^2 \ln \left| \dfrac{1}{n-1} \right|, & n \simeq 1, \\[2ex] \dfrac{8}{3} - 2\pi(\sqrt{2}-1)|n|, & |n| \ll 1, \\[2ex] \dfrac{8}{3} - \dfrac{\pi}{2}, & |n| \gg 1 \end{cases} \qquad (2.15)$$

(SR and WR regimes).

Notable features include the zero of σ_{tr} at $n = 1$ and the plateau-like inflection point at $n = -0.96$ (see Fig. 2.4). The left SR regime in Fig. 2.3 corresponds to the negative refractive index $n < 0$, and so we gave it an additional appellation of "Veselago reflector" (VR). The typical ray trajectories are shown in Fig. 2.2(b). The left diagonal line $X = -\rho$ separating the WR and the SR(VR) regimes corresponds to $n = 0$. Along this line the ray formalism predicts a cusp in σ_{tr}, see Fig. 2.4 and the second line of Eq. (2.15). (In reality, the cusp is rounded and shifted by $\mathcal{O}(1/X)$ quantum corrections, cf. Fig. 2.7 below.) On the other hand, transport cross-section varies smoothly across the right diagonal line $X = \rho$ (or $n = 2$) in Fig. 2.3 separating the WR and the SR regimes.

Another analytical result can be derived in the limit $|n| \to \infty$, which describes the leftmost and rightmost parts of the SR regimes in Fig. 2.3. The rays pass almost through the center of the disk in this limit, and so it is possible to sum the ray
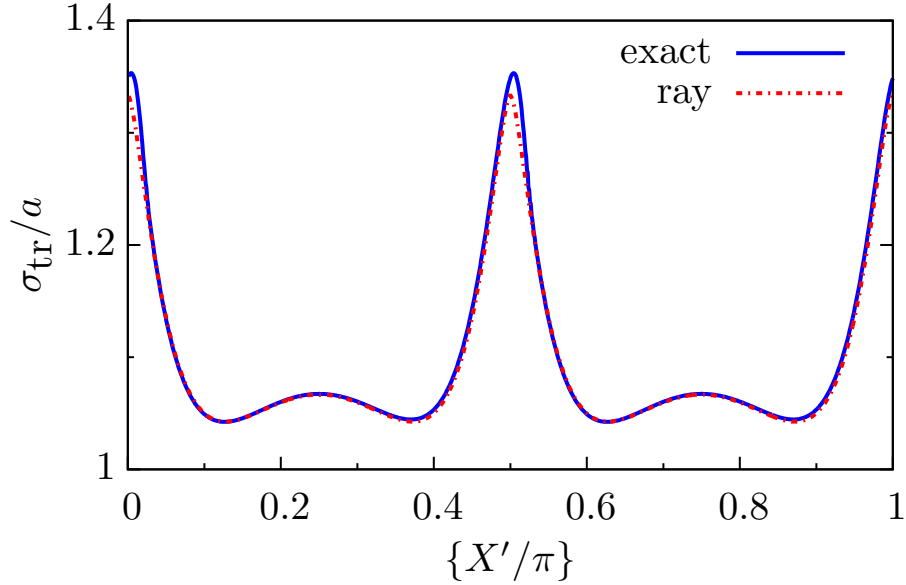
Figure 2.5: (Color online) Transport cross-section for $|n| \gg 1$ case as a function of $\{X'/\pi\}$, the fractional part of X'/π. The line labelled "exact" represents Eq. (2.8) evaluated for a fixed $X = 10^3$ and $\{X'/\pi\} = X'/\pi - 10^7$. The line labelled "ray" is Eq. (2.16).

amplitudes fully taking into account their interference and obtain

$$\frac{\sigma_{\text{tr}}}{a} \simeq \frac{8}{3} + \sec^5 2X' \left[\cos 2X' - \frac{7}{3} \cos 6X' \right.$$
$$\left. + \frac{1}{4} \left(-8 \cos 4X' + \cos 8X' + 7 \right) \ln \tan^2 X' \right] \qquad (2.16)$$

(SR regime, $|n| \to \infty$ limit).

This expression is $\pi/2$-periodic in X' and if ρ is fixed, also in X, as expected for the Fabry-Pérot (FP) resonator of length $2a$. Figure 2.5 shows the transport cross-section and the comparison between the exact result and Eq. (2.16).

The border of the WS regime in Fig. 2.3 is defined by the curves $X^3 = \pm\rho$ at $X > 1$ and $\rho = \pm 1$ at $X < 1$. The $X > 1$ part is described by the HEA. More

precisely, the HEA describes the small-angle part of the scattering amplitude; however, it is sufficient for computing both the total and transport cross-sections in the WS regime. The total cross-section is given by

$$\frac{\sigma}{a} = 2\pi H_1(2\rho) \tag{2.17a}$$

$$\simeq \begin{cases} \dfrac{16}{3}\rho^2, & \rho \ll 1\,, \\[2ex] 4\left[1 - \dfrac{\pi}{4\rho}\cos\left(2\rho - \dfrac{\pi}{4}\right)\right], & \rho \gg 1 \end{cases} \tag{2.17b}$$

(HEA regime),

where $H_1(z)$ is the Struve function. The transport cross-section has the form

$$\frac{\sigma_{\mathrm{tr}}}{a} \simeq \frac{2\rho^2}{X^2}\ln X \quad \text{(HEA regime).} \tag{2.18}$$

The $|\rho| \ll 1$ part of the HEA domain is alternatively described by the BA. Additionally, the BA gives the form of the differential cross-section for arbitrary angles ϕ:

$$\frac{d\sigma}{d\phi} = \frac{\pi}{2}\frac{\rho^2 a}{X}\cot^2\left(\frac{\phi}{2}\right)J_1^2\left(2X\sin\frac{\phi}{2}\right) \quad \text{(BA).} \tag{2.19}$$

Integrating Eq. (2.19) over ϕ, we obtain

$$\frac{\sigma}{a} \simeq \begin{cases} \dfrac{16}{3}\rho^2, & X \gg 1, \\[2ex] \dfrac{\pi^2}{2}\rho^2 X, & X \ll 1, \end{cases} \tag{2.20}$$

$$\frac{\sigma_{\mathrm{tr}}}{a} \simeq \begin{cases} \dfrac{2\rho^2}{X^2}\ln X, & X \gg 1, \\[2ex] \dfrac{\pi^2}{4}\rho^2 X, & X \ll 1 \end{cases} \tag{2.21}$$

$$\text{(BA regime)}.$$

The upper lines in these equations agree with the HEA. The formulas on the lower lines differ from Eq. (12) of Ref. [Gui08] and Eq. (51) of Ref. [KN07] proposed earlier for the same regime. We believe ours to be the correct ones. Unlike in the SR and WR domains, the cross-sections in the WS regime (both HEA or BA) cannot be written solely in terms of the classical quantities n and a.

A component missing in the ray series is the resonant tunneling of the rays with impact parameters b larger than the radius of the disk [Fig. 2.2(c)]. These rays correspond to the partial wave with $j = kb > X$. Within the semiclassical picture the region $a < r < b$ is classically forbidden due to the "centrifugal" potential barrier. The tunneling through such a barrier is usually exponentially small unless the resonance condition is met. For certain values of ρ and X, tunneling of the waves with specific $\pm j_r$ becomes strongly enhanced, which creates sharp maxima of the cross-sections.[Gra00] The resonant tunneling may be encountered for either type of doping. A necessary condition for the resonance is that some of disk interior is classically allowed. This is possible if $n > 1$ or $n < -1$, so that the interval $X < |j| < |X'|$

exists. The condition for the zth resonance $(z = 1, 2, \ldots)$ can be derived from the Bohr-Sommerfeld quantization rule valid for $X \gg 1$. This condition has the form

$$2\sqrt{X'^2 - j^2} - 2|j| \cos^{-1} \frac{|j|}{X'} + 2\Theta_+ - \frac{\pi}{2} = 2\pi z, \qquad (2.22)$$

where $\Theta_+ \sim 1$ is the phase shift of the inner reflection at the disk boundary, cf. Sec. 2.4.1. Since Eq. (2.22) is invariant under the sign change of j, a pair $j = \pm j_r$ would resonate simultaneously. From Eq. (2.7) we see that each resonant partial wave with $|j| > X$ contributes up to $4a/X$ to the cross-section, so each resonant pair contributes up to $8a/X$. This amount is parametrically small compared to the collective contributions $\sim a$ of all the $j < X$ partial waves. Hence, the resonances produce only a small "ripple structure" in the cross-section.[Chý76] In contrast, at $X \ll 1$ and $\rho \gg 1$, the RS is the dominant effect. In this regime, the cross-sections are given by the approximate formulas [HA08, BTB09] (see Sec. 2.4.1)

$$\frac{d\sigma}{d\phi} \simeq \sum_{j \geq 1/2} \frac{\sigma_j}{\pi} \cos^2 j\phi, \qquad (2.23)$$

$$\sigma_j = \frac{8a}{X} \sum_{z=1}^{\infty} \frac{\gamma^2}{(\rho - \rho_{j,z})^2 + \gamma^2}, \qquad (2.24)$$

$$\sigma \simeq \sum_{j \geq 1/2} \sigma_j, \quad \sigma_{\text{tr}} \simeq \frac{\sigma_{1/2}}{2} + \sum_{j \geq 3/2} \sigma_j \qquad (2.25)$$

(RS regime)

with $\rho_{j,z}$ and γ defined by Eqs. (2.53) and (2.56) in Sec. 2.4.

Let us now illustrate some of the above formulas by specific examples. The RS behavior is depicted in Fig. 2.6, which shows the differential cross-sections for $X = 0.3$
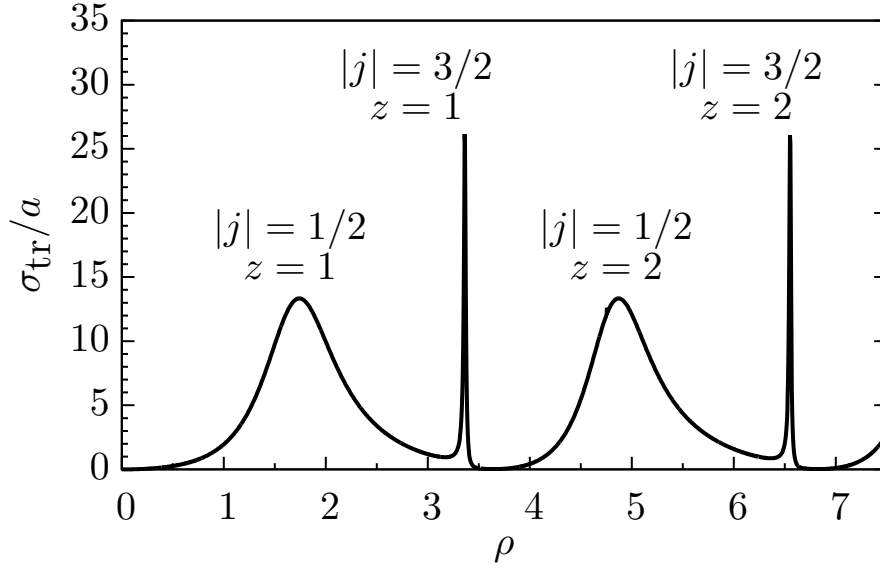
Figure 2.6: Transport cross-section in the BA and RS regimes, $X = 0.3$. Labels j and z denote the angular momentum of the resonant partial waves and index of the quasibound state in the disk.

and varying ρ. Note that $j = 3/2$ resonance is much more narrow that $j = 1/2$, in agreement with the formula $\gamma \sim X^{2j}$ [Eq. (2.56)] for the linewidth. The BA behavior $\sigma_{\mathrm{tr}} \propto \rho^2$ [Eq. (2.21)] is seen to occur at small ρ.

Next, consider the dependence of the cross-section as a function of the electron density, $n_e = k^2/\pi = X^2/(\pi a^2)$ for a fixed potential strength V_0 in SR and WR regimes. Figure 2.7(a) shows the transport cross-section for $V_0 = -0.5\,\mathrm{eV}$, which models the effect of Al, Ag, or Cu adsorbates weakly coupled to graphene.[GKB$^+$08] In this case, the system is always a n-N junction, i.e., $n > 0$. The dashed-dotted curve in Fig. 2.7(a) is given by the ray formula, Eq. (2.13). It fits well with the (numerically) exact results from PWD, especially for $a = 100\,\mathrm{nm}$. For $a = 20\,\mathrm{nm}$, the deviations of the PWD curve from the ray formula are larger. However, they almost never exceed $8a/X$, the vertical shift between the dashed-dotted and dotted curves.

(a)

(b)
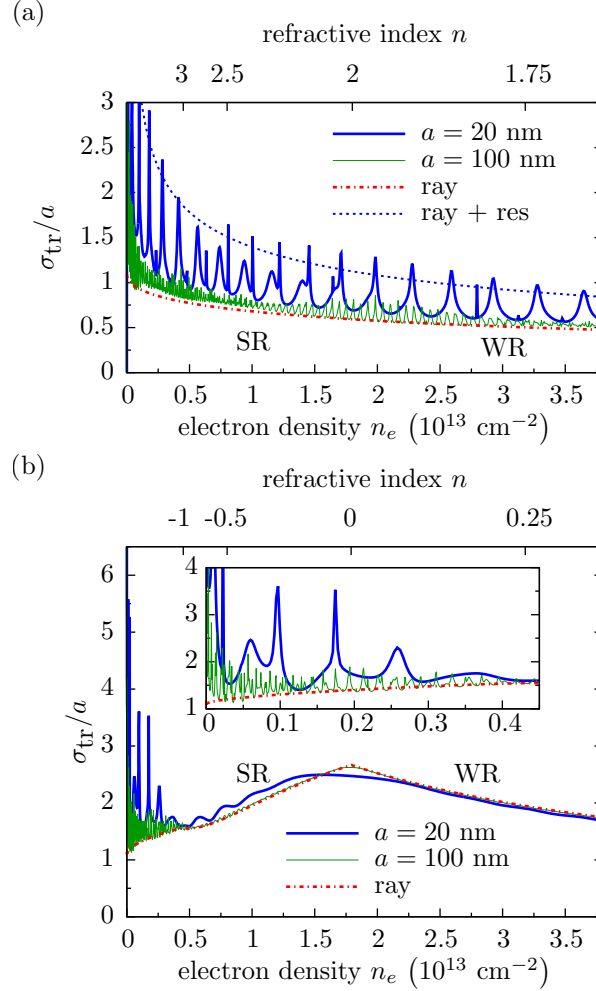
Figure 2.7: (Color online) Transport cross-section as a function of electron density. (a) $V_0 = -0.5\,\text{eV}$ or $\rho \approx +300\,\text{nm}/a$. (b) $V_0 = +0.5\,\text{eV}$ or $\rho \approx -300\,\text{nm}/a$. Thick solid curves: the exact result from PWD for $a = 20\,\text{nm}$. Thin solid curves: the exact result from PWD for $a = 100\,\text{nm}$. Dashed-dotted curves: Eq. (2.13), from the ray picture. Dotted curves: the sum of the ray term [Eq. (2.13)] and a single resonance $8a/X$ for $a = 20\,\text{nm}$. The inset of (b) shows the effect of the resonances at small density where $n < -1$.

This shows that this contribution comes predominantly from a single resonant pair; bunching of the resonances is atypical. We checked that the positions of the resonances are rather well described by Eq. (2.22). Figure 2.7 also shows that as n_e increases, the resonance contribution becomes smaller compared to the ray term, as expected because X increases. The curve marked $a = 20$ nm in Fig. 2.7(a) is computed for the same parameters as in Fig. 2 of Ref. [KGG09]. The results are clearly different both in magnitude and periodicity. The reason for the disagreement is unknown because the same mathematical formula [Eq. (2.8)] was used both in our calculation and in Ref. [KGG09]. We believe our results are correct because they are consistent with our analytic formulas.

In Fig. 2.7(b), we consider $V_0 = +0.5$ eV, where the system changes from an n-p junction to a n-N junction as the electron density increases. The ripple structure exists only at $n < -1$, in agreement with the condition discussed above. It is worth noting that in the limit $|n| \ll 1$, the transport cross-section, σ_{tr} approaches the value of $8a/3$, the known result for an impenetrable disk.[YM07] This is the maximum transport cross-section one can get for massless Dirac fermions at $X \gg 1$. However, in the opposite limit $|n| \gg 1$, which would also correspond to impenetrable disk for massive fermions, Eq. (2.15) predicts a different and significantly smaller value $\sigma_{\mathrm{tr}} = (8/3 - \pi/2)a \approx 1.1a$. This highlights the ability of massless Dirac to penetrate high barriers via Klein's tunneling.

Consider now graphene with many randomly positioned identical disks of low enough concentration $n_c \ll 1/a^2$. Our results can be used to compute the conductivity G of such a system if its size is larger than the mean-free path $l = v_F \tau_{\mathrm{tr}}$. The

(a)

(b)

(c)
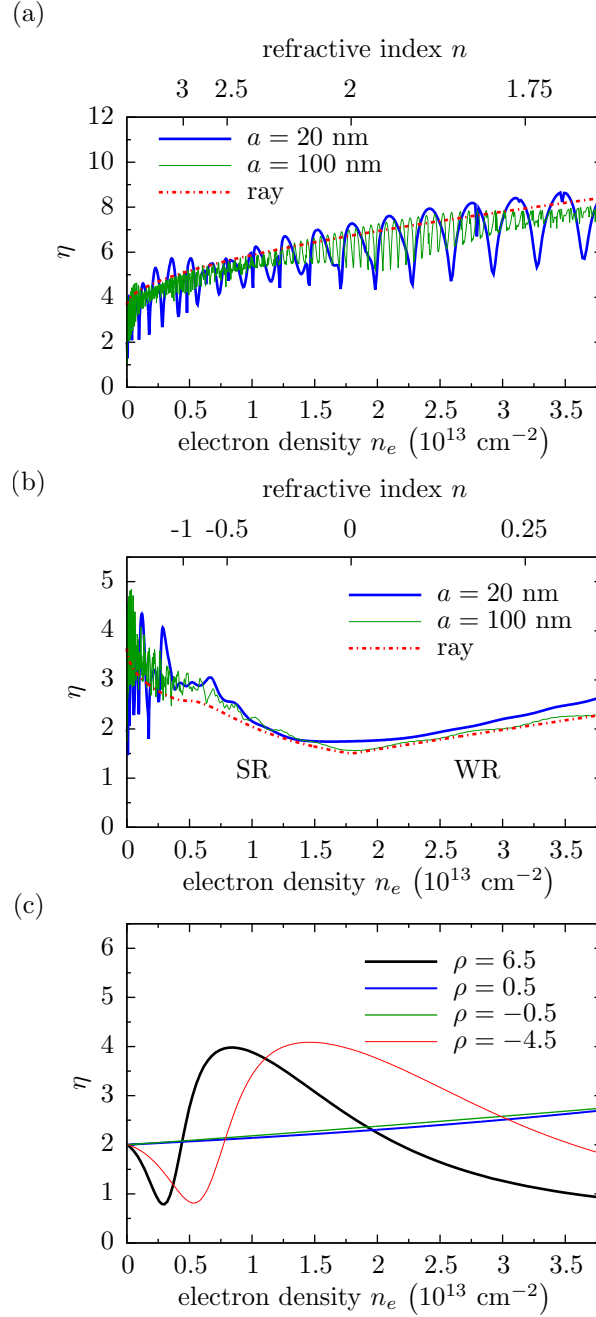
Figure 2.8: (Color online) The ratio η of the quantum and transport times as a function of the electron density n_e. (a) $V_0 = -0.5\,\mathrm{eV}$ or $\rho \approx +300\,\mathrm{nm}/a$, same as in Fig. 2.7(a). (b) $V_0 = +0.5\,\mathrm{eV}$ or $\rho \approx -300\,\mathrm{nm}/a$, same as in Fig. 2.7(b). (c) "Point-like" scatterer, $a = 1\,\mathrm{nm}$.

conductivity is related to the transport cross-section by

$$G = \frac{2e^2}{h} k_F v_F \tau_{\text{tr}} = 2\sqrt{\pi} \frac{e^2}{h} \frac{\sqrt{n_e}}{n_c \sigma_{\text{tr}}} \,. \tag{2.26}$$

Note that Eq. (2.26) neglects logarithmic corrections due to multiple scattering effects. [AE06, OGM06] If the disks are slightly different in size or shape or the system is at finite temperature, we expect the ripple structure in σ_{tr} to be washed out leaving only the overall trends. For example, for parameters used in Fig. 2.7, the disorder-averaged transport cross-section should change slowly with the carrier concentration n_e, remaining close to $\sim a$. Hence, the conductance will have an approximately $\sqrt{n_e}$ dependence. Such a dependence is different from those for both the charged impurities and the short-ranged defects computed within the BA in Ref. [HDS08], which are, respectively, linear and constant in n_e.

An important parameter η characterizing the spatial structure of impurities is the ratio of the transport time τ_{tr} and the quantum lifetime τ_q [Eq. (2.1)]. This parameter is related to the cross-sections via

$$\eta = \frac{\tau_{\text{tr}}}{\tau_q} = \frac{\sigma}{\sigma_{\text{tr}}}. \tag{2.27}$$

Experimentally, τ_{tr} can be extracted from the conductivity measured in the absence of magnetic field [Eq. (2.26)] whereas τ_q can be obtained from the damping rate of the Shubnikov-de Haas oscillations in magnetotransport. A large η indicates that scattering is predominantly in the forward direction while a small η indicates that scattering by large angle is possible. The former is a feature of long-range impurities. The latter may indicate either that the impurities are short-range or they are have

sharp boundaries.

In Fig. 2.8(a) and Fig. 2.8(b), we compute η for large scatterers and $V_0 = \pm 0.5$ eV, respectively. For the n-type scatterers ($V_0 < 0$) in Fig. 2.8(a), η increases from 4 to 7 with the electron density, which is a range of values found in the experiment.[Gor09] The ray formula is basically the envelope of the exact results. The ripple structure exists everywhere since $|n| > 1$ for all the electron density. For the p-type scatterers ($V_0 > 0$) in Fig. 2.8(b), the ray formula fits even better except again for the ripple structure at $n < -1$. Parameter η exhibits a minimum at $n = 0$, which is due to the maximum of the transport cross-section at such n, Fig. 2.7(b).

In Fig. 2.8(c), we show η computed for disks of small radius $a = 1$ nm. Note that two scattering regimes are possible for small impurities, RS ($\rho \gg 1$) and WS ($\rho \ll 1$). In the WS regime, the scattering dominated by the partial waves with $|j| = 1/2$, so that $\eta \approx 2$, cf. Eqs. (2.24) and (2.25). In the RS regime, partial waves with $|j| > 1/2$ can also contribute due to the resonant tunneling. These higher-j partial waves can interfere with $|j| = 1/2$ partial waves to form Fano-like resonance, see the $\rho = 6.5$ and -4.5 curves in Fig. 2.8(c). The Fano-like resonance leads to $\eta < 2$ at some electron density. It is worth noting that η can be smaller than unity ($\sigma_{\mathrm{tr}} > \sigma$) at the Fano-like resonance, which is unusual: it implies that the backscattering dominates the forward scattering. Similar physics is discussed in Ref. [HBF13]. However, as mentioned earlier, small randomness in size or shape of the disks unavoidable in practice would cause the ripple structure in η, including the Fano-like resonances, to be suppressed.

2.3   Semiclassical ray picture

In this Section we outline the derivation of the ray series, which is a useful tool for investigating the $X \gg 1$ regimes, where the PWD series [Eq. (2.6)], although formally exact, suffers from slow convergence and does not give much physical insight. We label the rays by integer p. Figure 2.2 shows schematically a first few rays in the series: the reflected ray $p = 0$, the directly transmitted ray $p = 1$, and the ray transmitted after one internal reflection $p = 2$. The higher-order rays undergo $p - 1$ internal reflections. The refraction angle β is related to the incidence angle α (Fig. 2.2) by Snell's law

$$\sin \beta = \frac{\sin \alpha}{n} . \tag{2.28}$$

As in optics, the ray series can be derived from the PWD via an intermediate step of the so-called Debye series, where the summation over j, Eq. (2.6), is transformed into an integral and evaluated by the saddle-point approximation. We applied a similar procedure to our problem, see Appendix 2.9 for details. The final result has the form

$$f(\phi) = \sum_{p=0}^{\infty} f_p(\phi) + i \sqrt{\frac{2}{\pi k}} \frac{\sin X\phi}{\phi} , \tag{2.29a}$$

$$f_p(\phi) = e^{-\frac{i\pi}{4}} \sum_{\alpha} \left| \frac{d\phi_p}{db} \right|^{-\frac{1}{2}} C_p(\alpha) e^{i\varphi_o + i\varphi_c}, \tag{2.29b}$$

where ϕ_p is the total deflection angle of ray p given by

$$\phi_p = \pi - 2\alpha - p(\pi - 2\beta) . \tag{2.30}$$

Each scattering angle ϕ may correspond to multiple, single, or none of the rays, depending on the number of real solutions of the equation

$$\phi = \phi_p + 2\pi l , \tag{2.31}$$

where l is some integer. If the dependence of ϕ_p on α is nonmonotonic, there may be several solutions for α even for the same l, in which case they all need to be included in the calculation of f_p.

Since the impact parameter (Fig. 2.2) is given by

$$b = a \sin \alpha, \tag{2.32}$$

the derivative $d\phi_p/db$ in Eq. (2.29b) can be written as

$$\frac{d\phi_p}{db} = \frac{1}{a \cos \alpha} \frac{d\phi_p}{d\alpha} . \tag{2.33}$$

For now, we assume that this derivative is nonvanishing. Later in Sec. 2.4.2 we explain how to modify Eq. (2.29b) if this is not the case. The ray amplitude $C_p(\alpha)$ in Eq. (2.29b) is expressed in terms of the plane-wave reflection and transmission

coefficients of the ray at a flat interface:[KN07]

$$C_p(\alpha) = \begin{cases} R_\text{out} & , \quad p = 0 \,, \\ T_\text{out} T_\text{in} R_\text{in}^{p-1} & , \quad p > 0 \,, \end{cases} \tag{2.34}$$

$$R_\text{out} = i e^{i\alpha} \frac{\sin\left(\dfrac{\alpha - \beta}{2}\right)}{\cos\left(\dfrac{\alpha + \beta}{2}\right)} \,, \tag{2.35}$$

$$T_\text{out} = 1 + R_\text{out} \,, \tag{2.36}$$

and R_in (T_in) are obtained from R_out (T_out) by interchanging α and β. The two phases appearing in the exponential in Eq. (2.29b) are

$$\varphi_o = -2X \cos\alpha + 2pX' \cos\beta \,, \tag{2.37}$$

$$\varphi_c = -\frac{\pi}{2}\left[p - \frac{1}{2}\left(1 + \operatorname{sgn}\frac{d\phi_p}{db}\right)\right] \equiv -\frac{\pi}{2} N_c \,. \tag{2.38}$$

Here φ_o represents the phase due to the optical path length and φ_c is the phase shift due to passing of the caustics,[LL75] which occurs N_c times. Finally, the last term of $f(\phi)$ in Eq. (2.29a) is the usual Kirchhoff diffraction contribution.

The ray series converge much more rapidly than the PWD because for most rays R_in and R_out are appreciably less than unity. (Recall that for the normal incidence the reflection vanishes exactly.) In particular, for small ρ, it suffices to consider only $p = 0$, 1, and 2 terms. To the leading order in ρ the solutions for $\alpha = \alpha(\phi)$ and $\beta = \beta(\phi)$ can be analytically. Substituting these into Eq. (2.29b), we obtain the first

three terms of the ray series as follows:

$$f_0(\phi) = -\frac{\rho}{X}\sqrt{\frac{a}{8}}\,\frac{\cos\dfrac{\phi}{2}}{\sin^{3/2}\dfrac{\phi}{2}}\exp\left[-i\left(\frac{\pi}{4}+\frac{\phi}{2}+2X\sin\frac{\phi}{2}\right)\right], \tag{2.39}$$

$$f_1(\phi) = \sqrt{\frac{X}{\rho}}\sqrt{\frac{a}{2}}\left[1+\left(\frac{X\phi}{2\rho}\right)^2\right]^{-3/4}\exp\left[i\left(-\frac{\pi}{4}+\sqrt{4\rho^2+X^2\phi^2}\right)\right], \tag{2.40}$$

$$f_2(\phi) = -\frac{\rho}{X}\sqrt{\frac{a}{8}}\,\frac{\cos\dfrac{\phi}{2}}{\sin^{3/2}\dfrac{\phi}{2}}\exp\left[i\left(\frac{\pi}{4}-\frac{\phi}{2}+2X\sin\frac{\phi}{2}\right)\right]. \tag{2.41}$$

These formulas will be important for the discussion of the differential cross-sections in Sec. 2.5.

The summation of the full ray series is possible using certain approximations. Consider the calculation of the transport cross-section. Neglecting the ray interference and the diffraction term (which is important only for forward scattering), we arrive at

$$\sigma_{\text{tr}} = \int_{-a}^{a} db(1-\cos\phi)\sum_p |A_p|^2, \tag{2.42}$$

with b defined by Eq. (2.32) and A_p given by

$$A_p = C_p(\alpha)e^{i\varphi_o+i\varphi_c}. \tag{2.43}$$

Using Eqs. (2.30), (2.34)–(2.36), we obtain

$$\sigma_{\text{tr}} = 2a + a\int_{-\pi/2}^{\pi/2} d\alpha \cos\alpha \left[R^2\cos 2\alpha - \text{Re}\frac{e^{i(2\beta-2\alpha)}}{1+R^2e^{2i\beta}}\right], \tag{2.44}$$

where $R = |R_{\text{out}}| = |R_{\text{in}}|$. After some changes of variable Eq. (2.44) can be transformed

to Eqs. (2.13) and (2.14). It is possible to express the correction $\varsigma(n)$ in the latter in terms of $K(m)$, $E(m)$ and $\Pi(z, m)$, which are the complete elliptic integrals of, respectively, the first, the second, and the third kind. The result is

$$\varsigma(n) = -\frac{4}{3} \frac{\text{sgn}(n)}{(2n-1)^2} \text{Re}\left[c_1 E\left(\frac{1}{n^2}\right) + c_2 K\left(\frac{1}{n^2}\right)\right.$$
$$\left. + c_3 \Pi\left(\frac{2n-1}{n^2}, \frac{1}{n^2}\right)\right], \tag{2.45a}$$

$$c_1 = -n(2n-1)\left(2n^3 - 4n^2 + 5n - 1\right), \tag{2.45b}$$

$$c_2 = (n-1)(4n^4 - 6n^2 + 7n - 3), \tag{2.45c}$$

$$c_3 = -6(n-1)^4. \tag{2.45d}$$

Another tractable limit is $n \to \infty$, where $\beta \to 0$ so that all the odd-p rays scatter into the same final direction and interfere with each other, and similar for all the even-p rays. Equation (2.42) is modified to

$$\sigma_{\text{tr}} = \int_{-a}^{a} db(1 - \cos\phi)\left|\sum_p A_p\right|^2, \tag{2.46}$$

while the ray amplitudes are found to be

$$\left|\sum_p A_p\right|^2 = \left|\sum_{p \text{ odd}} A_p\right|^2 + \left|\sum_{p \text{ even}} A_p\right|^2, \tag{2.47a}$$

$$\left|\sum_{p \text{ odd}} A_p\right|^2 = \frac{\cos^2 \frac{\phi}{2}}{1 - \sin^2 \frac{\phi}{2} \cos^2 \Phi}, \tag{2.47b}$$

$$\left|\sum_{p \text{ even}} A_p\right|^2 = \frac{\sin^2 \frac{\phi}{2} \sin^2 \Phi}{1 - \cos^2 \frac{\phi}{2} \cos^2 \Phi}. \tag{2.47c}$$

Substituting Eqs. (2.47a)–(2.47c) into Eq. (2.46), we obtain Eq. (2.16) by an elementary integration.

2.4   Beyond the ray picture

In the previous sections, we have shown the benefits of the ray series for understanding the primary features of the scattering amplitudes in the large-X semiclassical regime. Here we address some interesting secondary effects that are beyond the ray picture. Technically, the ray series is derived using the saddle-point approximation to evaluate the contour integral leading to the Debye series (Appendix 2.9). The additional effects can be, in principle, derived by a more accurate approximation of the same contour integral. Thus, the resonances that produce the ripples (Sec. 2.2) can be accounted for by including contributions from not only the saddle-point but also the poles in the complex j plane.[Nus69, Gra00] However, below we use a simpler derivation directly from the PWD.

The saddle-point approximation is also insufficient if the ray deflection angle ϕ_p is a nonmonotonic function of the impact parameter b, so that $d\phi_p/db$ may vanish. In this case Eq. (2.29b) cannot be used as it gives a divergent result. This problem is especially apparent for refraction index in the interval $1 < n < 2$ where the divergent contribution is not overshadowed by other, non-divergent terms. The same divergence is encountered in the theory of rainbow in optics[Gra00] and a common remedy for it is to replace the saddle-point approximation by a so-called uniform approximation.[CFU56] Similar issues arise for rays with incident angle α close to the critical angle. This regime is realized for $|n| < 1$ and is known as the near-critical scattering.[Gra00] Finally, the saddle-point approximation becomes inaccurate if the

optical phase shift ϕ_o [Eq. (2.37)] is small, which occurs when the scattering potential is weak. To handle this case we use an alternative approach based on perturbation theory, either the HEA or the BA. Let us now consider each of these special regimes in more detail.

2.4.1   Resonances

As explained in Sec. 2.1, the contribution to the cross-sections from a partial wave of a given angular momentum j is proportional to $\sin^2 \delta_j$, where δ_j is the scattering phase shift. This quantity can be written in the form

$$\sin^2 \delta_j = \frac{1}{1 + \left(\dfrac{\operatorname{Im} s_j}{\operatorname{Re} s_j}\right)^2} . \tag{2.48}$$

The exact expression for s_j given in Appendix A [cf. Eq. (2.83)] involves a combination of Bessel functions. It can be simplified in certain limits using suitable asymptotic expansions of these functions. Thus, for $X \gg 1$ we can use the Debye expansion to arrive, after some algebra, at

$$\frac{\operatorname{Im} s_j}{\operatorname{Re} s_j} \simeq \frac{\sin(\Phi_c + \Theta_+)}{\sin(\Phi_c + \Theta_-)} \exp\left(-2\sqrt{j^2 - X^2} + 2j \cosh^{-1} \frac{j}{X}\right), \tag{2.49}$$

$$\Phi_c \equiv \sqrt{X'^2 - j^2} - j \cos^{-1} \frac{j}{X'} - \frac{\pi}{4}, \tag{2.50}$$

$$\Theta_\pm = \frac{\pi}{2} + \tan^{-1}\left(\frac{\dfrac{\sqrt{X'^2 - j^2}}{X'}}{\dfrac{|j| \pm \sqrt{j^2 - X^2}}{X} - \dfrac{|j|}{X'}}\right). \tag{2.51}$$

The resonance occurs when $\sin^2 \delta_j$ attains a maximum, i.e., when the left-hand side of Eq. (2.49) is equal to zero. Therefore, the resonance condition is $\sin(\Phi_c + \Theta_+) = 0$,

which gives Eq. (2.22) and corresponds physically to the whispering-gallery modes.

To find the resonance condition in the opposite limit of $X \ll 1$, we use a Taylor expansion of the Bessel functions that have X as an argument. We obtain

$$\sin^2 \delta_j \simeq \left\{ 1 + \left[\frac{4^j \Gamma(1/2 + j)^2}{\pi X^{2j}} \frac{J_{j-1/2}(X')}{J_{j+1/2}(X')} \right]^2 \right\}^{-1} , \tag{2.52}$$

where $\Gamma(x)$ is the Euler Gamma-function. Let $Z_{j,z}$ be the zth zero of one of the remaining Bessel functions, $J_{j-1/2}(Z_{j,z}) = 0$. We define

$$\rho_{j,z} \equiv Z_{j,z} - X \tag{2.53}$$

and expand $J_{j-1/2}(X') = J_{j-1/2}(X + \rho)$ to the linear order in $\rho - \rho_{j,z}$:

$$J_{j-1/2}(X') \simeq -J_{j+1/2}(Z_{j,z})(\rho - \rho_{j,z}) . \tag{2.54}$$

From Eqs. (2.52)–(2.53), we obtain

$$\sin^2 \delta_j = \frac{\gamma^2}{(\rho - \rho_{jr})^2 + \gamma^2} , \tag{2.55}$$

$$\gamma = \frac{\pi}{4^j \Gamma(j + 1/2)^2} X^{2j} , \tag{2.56}$$

which leads to Eqs. (2.23)–(2.25). It is interesting to note that γ vanishes if the incident electron has zero energy ($X = 0$). Accordingly, the lifetime $1/\gamma$ of the resonance is infinite. Physical, it means that Dirac quasiparticles can be trapped indefinitely inside a locally doped region embedded in the otherwise undoped graphene. [HA08, BTB09, MP08]
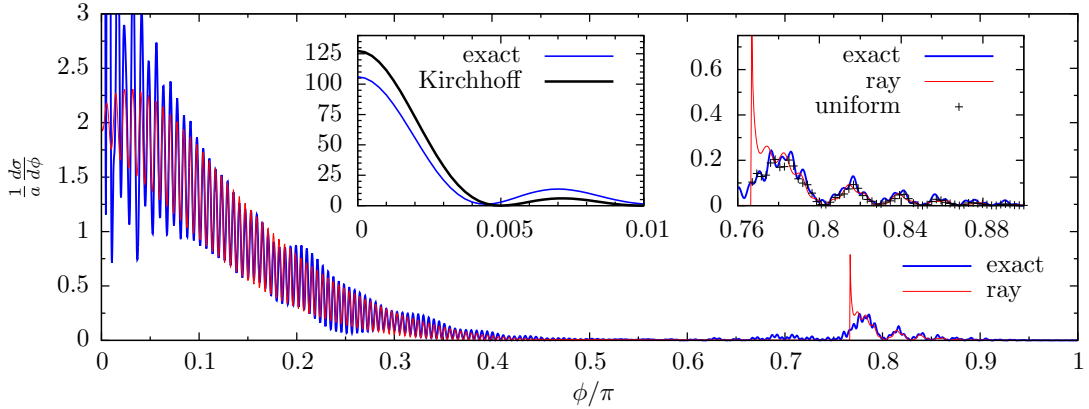
Figure 2.9: (Color online) Differential cross-section for $X = 200$ and $n = 1.33$. The main $p = 2$ rainbow appears at $\phi/\pi = 0.76$. The right inset shows the comparison among the uniform approximation, the ray formula, and the PWD. The left inset shows the comparison between the Kirchhoff diffraction and the PWD.

2.4.2 Dirac rainbow

If $\phi_p(\alpha)$ is a nonmonotonic function of α, there may exist α_r such that

$$\left.\frac{d\phi_p}{d\alpha}\right|_{\alpha=\alpha_r} = 0 \,. \tag{2.57}$$

The same condition corresponds to the rainbow phenomenon in optics. Near $\alpha = \alpha_r$, Eq. (2.30) has more than one root. Two of such roots, α_+ and α_-, coalesce at $\alpha \to \alpha_r$. At $\alpha = \alpha_r$, the ray formula Eq. (2.29b) diverges and cannot be used. The divergence is cured by the uniform approximation of the Debye series,[CFU56, Ber66, Nus69]

with which we obtain

$$f_p(\phi) = (-i)^p e^{i\overline{\varphi}} \left(-\zeta\right)^{1/4}$$

$$\times \sum_{\mu=\pm 1} \left(\mathrm{Ai}(\zeta) + i\mu \frac{\mathrm{Ai}'(\zeta)}{(-\zeta)^{1/2}} \right) \frac{\sqrt{-\mu\pi}}{\sqrt{\left. \dfrac{d\phi_p}{db} \right|_{\alpha_\mu}}} C_p(\alpha_\mu) , \qquad (2.58)$$

where $\mathrm{Ai}(\zeta)$ is the Airy function. $\alpha_\pm$ are chosen such that $\varphi_o(p, \alpha+) - \varphi_o(p, \alpha-) > 0$, and $\overline{\varphi}$ and ζ are defined by

$$\overline{\varphi} = \frac{1}{2} \left[\varphi_o(p, \alpha_+) + \varphi_o(p, \alpha_-) \right] , \qquad (2.59)$$

$$\zeta = \left\{ \frac{3i}{4} \left[\varphi_o(p, \alpha_+) - \varphi_o(p, \alpha_-) \right] \right\}^{2/3} . \qquad (2.60)$$

An advantage of the uniform approximation is that it can be used for both $\phi < \phi_r$ and $\phi > \phi_r$ if we allow the roots $\alpha_\pm$ to be complex numbers (which are always conjugate to each other). In doing so, the branch cut of $\zeta(\phi)$ should be chosen such that ζ is negative for real $\alpha_\pm$, and positive when they acquire imaginary parts.

In Fig. 2.9 we compare the results of the uniform approximation, the ray formula, and the PWD for the differential cross-sections computed for $n = 1.33$. The rainbow condition, Eq. (2.57), can be satisfied for $p \geq 2$ rays. The main $p = 2$ rainbow appears at $\phi = 0.76\pi$, and the secondary $p = 3$ rainbow is found at $\phi = 0.23\pi$. As one can see from Fig. 2.9, the ray formula strongly deviates from the exact PDW result at the rainbow angles. On the other hand, at such angle the uniform approximation agrees well with the PWD (right inset). In the left inset of Fig. 2.9 we show the differential cross-section for small ϕ where the ray formula also fails. However, the differential cross-section is adequately described by the Kirchhoff diffraction formula
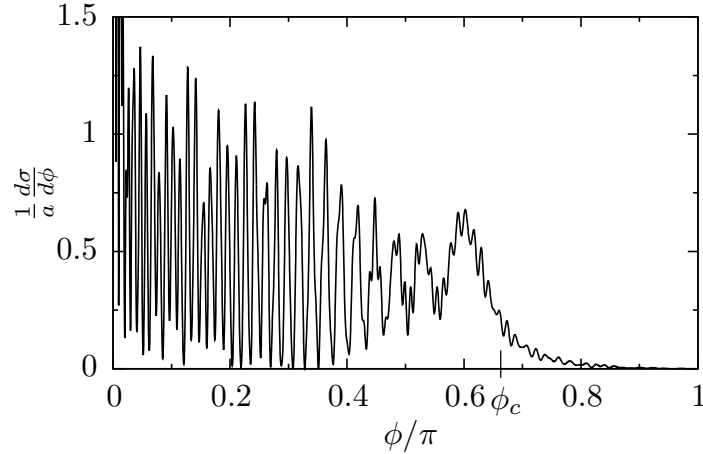
Figure 2.10: Differential scattering cross-section for $n = 0.5$ and $X = 200$ computed by the PWD. The critical angle $\phi_c = 2\pi/3$ [Eq. (2.61)] above which the $p = 0$ ray is totally reflected is labeled on the horizontal axis. Near this angle the cross-section exhibits oscillations similar to those near the rainbow angle in Fig. 2.9.

[the last term in Eq. (2.29a)].

2.4.3   Near critical scattering

Another phenomenon reminiscent of rainbow is the near critical scattering, which is realized at $|n| < 1$. At such n, the $p = 0$ ray is totally reflected for deflection angles larger than the critical angle [cf. Eq. (2.30)]

$$\phi_c = \pi - 2\arcsin n\,. \tag{2.61}$$

At $\phi < \phi_c$, the scattering enhanced due to the total reflection exhibits the "supernumerary" oscillation, while at $\phi > \phi_c$, the scattering rapidly decays. These Airy-function-like features are illustrated by Fig. 2.10.
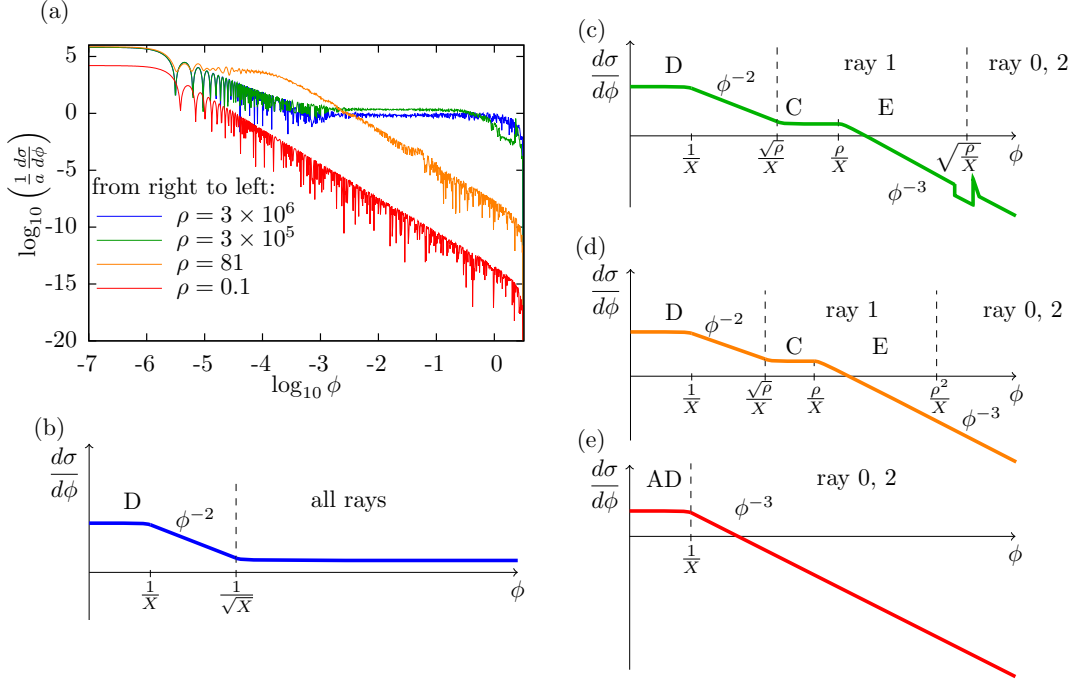
Figure 2.11: (Color online) Differential cross-section as a function of the deflection angle. The labels on the graphs stand for D: diffraction, C: central rays ($b \ll a$), E: edge rays ($|b| \approx a$), AD: anomalous diffraction. (a) The exact results for $X = 10^6$ and several ρ computed using the PWD. (b)–(e) are the schematic diagrams illustrating different regimes. (b) SR regime. At angles less than $1/\sqrt{X}$ the cross-section is dominated by diffraction. At larger angles, the cross-section can be computed from geometrical optics; however, accurate results require summing over many p in the ray series. (c) WR regime. Diffraction dominates at small angles, followed by the $p = 1$ ray and then by the $p = 0$ and 2 rays. A shallow dip followed by a peak exists in the narrow gap between the last two angular regions, at $\phi \sim \sqrt{\rho/X}$. The peak, which occurs on the ray-0,2 side, is the Dirac rainbow (Sec. 2.4.2). The dip between the ray-1 region and the rainbow exhibits another effect beyond the ray approximation — the Fock transition.[Gra00] (d) HEA regime. Diffraction dominates at small angles followed by the $p = 1$ ray and smoothly continued by the $p = 0, 2$ rays. (e) BA regime. Anomalous diffraction exists at angles smaller than $1/X$. At larger angles the scattering is dominated by the $p = 0$ and 2 rays.

2.4.4   Born approximation and high energy approximation

The development of the perturbation theory for the scattering begins with the exact Lippmann-Schwinger equation

$$\Psi(\mathbf{r}) = \frac{1}{\sqrt{2}} \begin{pmatrix} 1 \\ 1 \end{pmatrix} e^{ikx} + \int G_0(\mathbf{r} - \mathbf{r}')\widetilde{V}(\mathbf{r}')\Psi(\mathbf{r}')d^2\mathbf{r}', \tag{2.62}$$

where $\widetilde{V}(r) = V(r)/(\hbar v_F)$, $G_0(\mathbf{r})$ is the Green's function for the 2D Dirac equation,

$$G_0(\mathbf{r}) = -\frac{ik}{4} \begin{bmatrix} H_0^{(1)}(kr) & ie^{-i\phi}H_1^{(1)}(kr) \\ ie^{i\phi}H_1^{(1)}(kr) & H_0^{(1)}(kr) \end{bmatrix}, \tag{2.63}$$

and $H_j^{(1)}(x)$ is the Hankel functions of the first kind.   Following the standard route,[LL77] we seek the solution of Eq. (2.62) in the form

$$\Psi(\mathbf{r}) = \frac{1}{\sqrt{2}} \begin{pmatrix} 1 \\ 1 \end{pmatrix} e^{ikx} P(\mathbf{r}). \tag{2.64}$$

The corresponding scattering amplitude is

$$f(\phi) = -\sqrt{\frac{k}{2\pi}} e^{-i\phi/2} \cos\frac{\phi}{2} \int \widetilde{V}(\mathbf{r})P(\mathbf{r})e^{-i\mathbf{q}\cdot\mathbf{r}}d^2\mathbf{r}, \tag{2.65}$$

$$\mathbf{q} = k(\cos\phi - 1, \sin\phi). \tag{2.66}$$

One can show that for small angles and weak enough scattering potential, $\phi \ll \rho/X \ll 1$, function P is approximately equal to

$$P(x, y) = \exp\left(-i\int_{-\infty}^{x} \widetilde{V}(x', y)dx'\right).$$ (2.67)

This approximation [LL77] is known as the HEA. (The similar method called "paraxial approximation" optics was applied to graphene in Ref. [MMP11].) Since ϕ is always considered to be small within the HEA, we can achieve further simplification by writing the change in momentum [Eq. (2.66)] as

$$\mathbf{q} \simeq k\phi\hat{y}.$$ (2.68)

Substituting this into Eq. (2.65) and integrating over x, we obtain

$$f(\phi) = -i\sqrt{\frac{k}{2\pi}}e^{-i\phi/2}\cos\frac{\phi}{2}$$
$$\times \int_{-\infty}^{\infty} [P(\infty, y) - 1]\, e^{-ik\phi y}dy.$$ (2.69)

Furthermore, under the condition $\int \widetilde{V}dr \ll 1$, the quantity $P(\infty, y) - 1$ can be expanded to the first order in V, which leads to the first Born approximation (BA). Within the latter, the formula for the scattering amplitude can be simplified by integrating over the polar angle:

$$f(\phi) = -\sqrt{\frac{k}{2\pi}}e^{-i\phi/2}\cos\frac{\phi}{2}\int_{0}^{\infty} 2\pi\widetilde{V}(r)J_0(qr)rdr.$$ (2.70)

Although the HEA is valid only for small ϕ, the BA result holds for any ϕ as long as the potential V is weak, as specified above, and we use Eq. (2.66) for $\mathbf{q}$, i.e., $q = |\mathbf{q}| = 2k\sin(\phi/2)$. For the step potential [Eq. (2.3)], the calculations according to Eqs. (2.69), (2.70), and (2.9) yield the formulas for the total cross-sections presented in Sec. 2.2. Computing the transport cross-sections within the HEA and BA [Eqs. (2.18) and (2.21)] requires deriving the differential cross-sections first. These quantities are discussed in the next Section.

2.5 Differential cross-sections in each regime

In principle, numerical evaluation of the PWD series is not difficult even for large X as long as one keeps enough terms in the summation and uses reliable library subroutines for computing the requisite Bessel functions. The results of these calculations, which can be considered numerically exact, for $X = 10^6$ are presented in Fig. 2.11(a). While it is too high to be practical for graphene, choosing such a large X enables us to show more clearly the qualitative trends displayed by the differential cross-section $d\sigma/d\phi$ as a function of ϕ for four different fixed ρ. These trends are schematically illustrated in Figs. 2.11(b)–(e). In the rest of this Section we discuss how these trends can be understood based on the analytical approximations we developed above.

We begin with the SR regime where the ray series is accurate, and so Eqs. (2.29a) and (2.29b) can be used. At small angles, the last (diffraction) term in Eq. (2.29a) is the dominant one. It goes to a constant at $\phi = 0$ and decays as $d\sigma/d\phi \sim \phi^{-2}$ at $\phi \gg 1/X$. A crude sketch illustrating this behavior is shown in Fig. 2.11(b). It consists of a plateau at $\phi < 1/X$ and a straight line at $\phi > 1/X$. We label it by "D"

(for "diffraction"). The ray series dominates the diffraction at $\phi > 1/\sqrt{X}$, as shown schematically in Fig. 2.11(b). Since the scattering potential is strong, there is no particular restriction on the characteristic deflection angle of the rays. For any p, it can be as small as zero or as large as the maximum possible angle π. Therefore, the differential cross-section due to the ray contribution is shown to be flat in Fig. 2.11(b), meaning it does not vary much on the logarithmic scale. This is indeed the behavior exhibited by the $\rho = 3 \times 10^6$ curve in Fig. 2.11(a), which corresponds to the largest refraction index curve ($n = 4$) in that Figure.

In the WR regime, the "D" feature is also present, see Fig. 2.11(c). The ray contribution exceeds that of diffraction at $\phi > \sqrt{\rho}/X$. From Eqs. (2.39)–(2.41), one can show that the $p = 1$ ray dominates at $\sqrt{\rho}/X < \phi < \sqrt{\rho/X}$ and the $p = 0$ and $p = 2$ rays take over at $\phi > \sqrt{\rho/X}$. The contribution of the $p = 1$ ray to the cross-section decays at $\phi > \rho/X$ as $d\sigma/d\phi \sim \phi^{-3}$. This occurs because at such ϕ the $p = 1$ rays graze along the edge of the disk, $b \approx a$; hence, this domain is labeled "E" in Fig. 2.11(c). Note that a small dip in $d\sigma/d\phi$ exists at $\phi \sim \sqrt{\rho/X}$ that separates angular intervals dominated by $p = 1$ ray and the $p = 0$, 2 rays. Inside this dip no classical solutions exist for either $p = 1$ or 2 ray, while the contribution of $p = 0$ ray is already small. However, on the high-ϕ side of the dip there are two such solutions for $p = 2$. The interference between them gives rise to the Dirac rainbow, which was discussed in Sec. 2.4.2.

In the HEA and BA regimes, Figs. 2.11(d) and 2.11(e), respectively, the formulas from Sec. 2.4.4 apply. In the HEA regime, we use Eqs. (2.3) and (2.69) to

obtain

$$f(\phi) = i \sqrt{\frac{2}{\pi k}} \frac{\sin X\phi}{\phi} + I(\phi), \tag{2.71}$$

$$I(\phi) = -i \sqrt{\frac{k}{2\pi}} \int\limits_{-1}^{1} dy \, e^{-iX\phi y} \exp\left(2i\rho\sqrt{1-y^2}\right). \tag{2.72}$$

The first term of Eq. (2.71) is the same as the diffraction term in Eq. (2.29a). The second term $I(\phi)$ admits analytical approximations in some limits. At $\phi \ll \rho^2/X$, it can be calculated by the saddle-point approximation. The result is identical to $f_1(\phi)$ given by Eq. (2.40). At $\rho^2/X \ll \phi \ll 1$, the leading-order analytical approximation to $I(\phi)$ can be calculated by deforming the contour to a rectilinear path $(-1, -1 - i\nu\infty, 1 - i\nu\infty, 1)$, with $\nu = \mathrm{sgn}\,\rho$. The result is

$$I(\phi) \simeq -\frac{2\rho}{X} \sqrt{\frac{a}{\phi^3}} \cos\left(X\phi + \frac{\pi}{4}\right), \tag{2.73}$$

which is equal to the sum of $f_0(\phi)$ and $f_2(\phi)$, Eqs. (2.39) and (2.41). In the intermediate region, $\phi \sim \rho^2/X$, the two approximations match by the order of magnitude but none of them is quantitatively accurate. If desired, the integral $I(\phi)$ can be calculated numerically. The result would then provide a smooth connection between the $p = 1$ and $p = 0, 2$ ray formulas. Unlike in the WR regime, the differential cross-section has neither a dip nor a peak (rainbow) in this regime. Such geometrical optics features are smeared out in the HEA regime. Apart from this, it is remarkable that the HEA, which is typically considered a quantum theory, can be reproduced using the semiclassical ray picture. It is not very difficult to show that the crossover between the HEA and the WR occurs at $X \sim |\rho|^3$, see Fig. 2.3.

The differential cross-section of the HEA regime is shown schematically in Fig. 2.11(d). The $p = 1$ ray dominates over diffraction at $\phi > \sqrt{\rho}/X$. Its contribution to the cross-section behaves as ϕ^{-3} at $\phi > \rho/X$. The same trend is smoothly continued by the $p = 0, 2$ rays, which dominate at $\phi > \rho^2/X$.

Lastly, in the BA regime, we use Eqs. (2.3) and (2.70) to obtain

$$f(\phi) = \sqrt{2\pi X a}\, \rho\, e^{-i\phi/2} \cos\frac{\phi}{2} \frac{J_1\left(2X\sin\dfrac{\phi}{2}\right)}{2X\sin\dfrac{\phi}{2}}, \tag{2.74}$$

which entails Eq. (2.19). The differential cross-section in the BA regime is shown in Fig. 2.11(e). As mentioned in Sec. 2.2, the small-angle scattering in the BA regime is described by the anomalous diffraction, which originates from the destructive interference of the $p = 1$ rays with the usual diffraction. Consequently, the maximum value $\sigma'(0) = (\pi/2)a\rho^2 X$ of the differential cross-section is much smaller than the Kirchhoff result $\sigma'(0) = (2/\pi)aX$ [see the first term in Eq. (2.71)]. At $1/X \ll \phi \ll 1$, Eq. (2.74) agrees with Eq. (2.73) because the BA and the HEA are both valid at such angles, predicting the $d\sigma/d\phi \propto \phi^{-3}$ decay.

In summary, scattering of quasiparticles by large disks, $X \gg 1$, can be described by the ray series at all but very small deflection angles ϕ. At such small angles, there is a competition between the rays and diffraction. Diffraction dominates for the strong enough potential, $\rho \gg 1$. In the opposite case, the $p = 1$ rays nearly cancel the diffraction, making it "anomalous." As one can see from Fig. 2.11(a), the exact results for the differential cross-section at sufficiently large $X = 10^6$ agree very well with our schematic diagrams for all ρ pictured therein.

Based on the above results for the differential cross-sections, derivation of

the transport cross-sections within the HEA and BA [Eqs. (2.18) and (2.21)] is straightforward, and so we will not elaborate on it.

2.6 Near-field scattering

The previous Sections have been devoted to quantitative and qualitative discussion of far-field scattering amplitudes. In this Section, we turn our attention to the behavior of the electron wavefunction $\Psi(x, y)$ near the scatterer. As previously, we assume that electrons propagate ballistically before and after they collide with the disk. In such an idealized system, the incident plane wave can be created by injecting a small electric current in a particular direction. One quantity we will discuss is $|\Psi(x, y)|^2$, which determines the current-induced change in the local charge density (CCLCD). Additionally, having in mind Dirac fermions on a surface of a topological insulator, we will consider $\langle \sigma_z \rangle \equiv \langle \Psi | \sigma_z | \Psi \rangle$, which determines the current-induced change of the z-component of the local *spin* density (CCLSD). In graphene, the same expectation value defines pseudospin rather than spin density (and so it may be more difficult to probe experimentally). Our goal is to see how the qualitative features of the CCLCD and the CCLSD can be understood in terms of the concepts introduced in the previous Sections, in particular, partial wave resonances and semiclassical ray trajectories.

Figure 2.12 shows a suitably normalized CCLCD for six representative choices of X and ρ. The false color scale in this Figure is effectively nonlinear because we plot $|\Psi|^{1/8}$ instead of $|\Psi|^2$ to mitigate sharp contrast variations. The top left panel of Figure 2.12 pertains to the smallest-ρ $|j| = 3/2$ resonance in the RS regime. The resonance is seen to generate a dramatic enhancement of the CCLCD at the
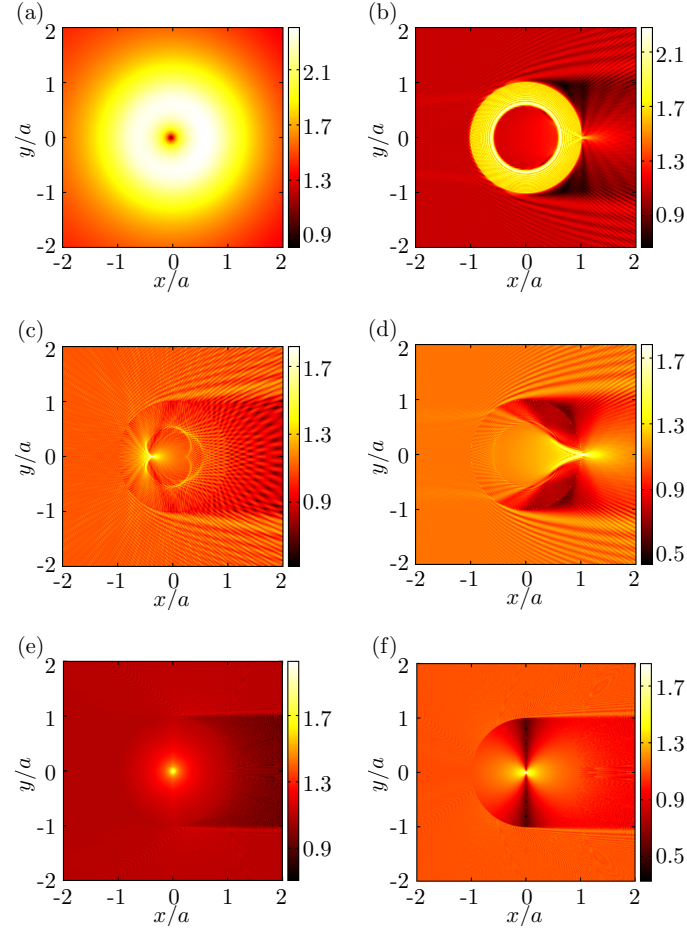
Figure 2.12: (Color online) Near-field features of the scattering wavefunction $\Psi(x, y)$ for several representative choices of X and ρ. In order to avoid drastic contrast variation in these false color diagrams, we plot $|\Psi|^{1/8}$ rather than $|\Psi|^2$. (a) A low angular momentum resonance occurring at $X = 0.3$, $\rho = 3.363$. The partial waves with $j = \pm 3/2$ are resonant. (b) A high angular momentum resonance ("whispering gallery mode") at $X = 100$, $\rho = 81.7762$. The partial waves with $j = \pm 165/2$ are resonant. (c) An example of negative refraction in the VR regime, $X = 100$, $\rho = -281$ ($n = -1.81$). (d) An example of caustic and lensing in the SR regime, $X = 100$, $\rho = 81$ ($n = 1.81$). (e), (f) FP regime $n \gg 1$ on and off the resonance, $\{X'/\pi\} = 0$ and 0.25, respectively (cf. Fig. 2.5).
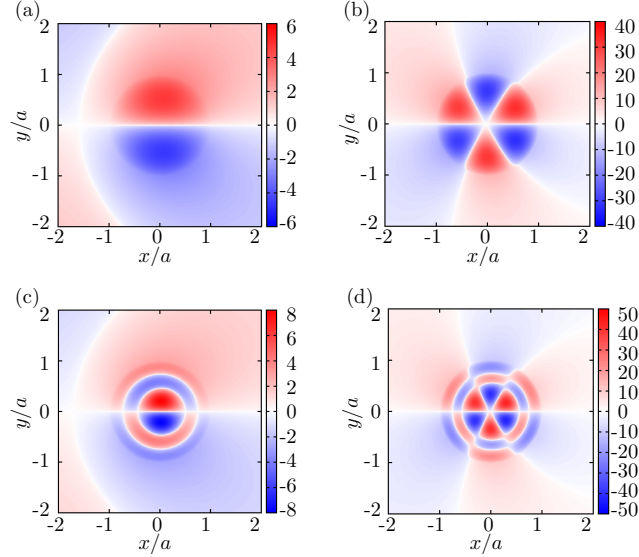
Figure 2.13: (Color online) Local z-component spin density $\langle\sigma_z\rangle \equiv \langle\Psi|\sigma_z|\Psi\rangle$ for the four resonances at $X = 0.3$ shown in Fig. 2.6. We plot $\mathrm{sgn}\langle\sigma_z\rangle|\langle\sigma_z\rangle|^{1/2}$ rather than $\langle\sigma_z\rangle$ to avoid too much contrast in these false color diagrams. (a) $\rho = 1.739$, the $j = 1/2$, $z = 1$ resonance. (b) $\rho = 3.363$, the $j = 3/2$, $z = 1$ resonance. (c) $\rho = 4.883$, the $j = 1/2$, $z = 2$ resonance. (d) $\rho = 6.555$, the $j = 3/2$, $z = 2$ resonance.

scatterer. It may be surprising that this enhancement is axisymmetric. This defies naive expectations that interference of $\pm j_r$ partial waves should produce an oscillatory angular dependence of the CCLCD. In fact, the lack of angular oscillations is peculiar to massless Dirac fermions. The states of angular momenta $\pm j_r$ are characterized by mutually orthogonal spinors; therefore, these states do not interfere with one another yielding a nearly axisymmetric CCLCD.

Resonances can also occur in the WR and SR regimes for the partial waves of high angular momenta $|j| \gg 1$, cf. Eq. (2.22). Such partial waves are analogous to the "whispering gallery" modes in optics. They produce ring-shaped CCLCD enhancement shown in Fig. 2.12(b). (Note that within the semiclassical picture the resonant states correspond to particles trapped inside the disk and orbiting in either direction around

its center.) In Figs. 2.12(c) and 2.12(d), we present examples of negative[CFA07] and positive refraction, respectively. Figure 2.12(c) depicts the CCLCD for $n = -1.81$, which is in the VR regime. The most notable features are the internal caustics that can be explained using the ray picture.[CPP07] Figure 2.12(d) shows CCLCD for $n = 1.81$. Here the refraction is positive and instead of the internal caustics, the rays exhibit focusing outside the disk. The narrowness of the whispering-gallery resonance can be appreciated by comparing Figs. 2.12(b) and 2.12(d). Although the refractive indices in the two cases differ by little more than 1%, their CCLCD look dramatically different. While in Fig. 2.12(d), the CCLCD is dominated by the focal point of the rays, in Fig. 2.12(b) it is almost completely overshadowed by the resonant partial waves. Thus, for the CCLCD a single pair of resonant partial waves can be more prominent than all other waves combined. This is in contrast to the far-field scattering quantities at $X \gg 1$, for which such a resonance typically gives only a small correction to the ray formula result [Eqs. (2.12) and (2.24)].

The last two panels in Fig. 2.12 illustrate the role of ray interference in the FP regime ($n \gg 1$), where the far-field cross-section exhibits periodic oscillations, see Fig. 2.5 in Sec. 2.2. We see in Figs. 2.12(e) and 2.12(f) that the ray interference also strongly influences the CCLCD, causing marked change in the CCLCD intensity along the vertical diameter of the disk on and off the resonance.

Let us now turn to the features of the local spin density. We have found that the CCLSD maps in the WR and SR regimes show qualitatively the same caustics and focal spots as the maps of the CCLCD. Therefore, these CCLSD maps do not seem to give much additional information and are not presented here. However, striking differences between the CCLCD and CCLSD appear in the RS regime. Figure 2.13

shows the CCLSD at the positions of the four resonances seen in Fig. 2.6. Unlike the CCLCD maps, the CCLSD shows strong angular variations. This can be seen from the comparison of Figs. 2.12(a) and 2.13(b), which have the same ρ and X. In order to avoid too drastic contrast variations in the false color, we again use nonlinear scaling and plot $\text{sgn}\langle\sigma_z\rangle|\langle\sigma_z\rangle|^{1/2}$ instead of $\langle\sigma_z\rangle$ in Fig. 2.13. The oscillations of the CCLSD are enabled by the discussed above interference of the $\pm j_r$ waves owing to the nonzero term $\langle\Psi_{-j_r}|\sigma_z|\Psi_{j_r}\rangle$. This interference causes the CCLSD to change its sign $2|j_r|$ times in the angular direction and z times in the radial direction.

One may wonder how the predicted CCLCD or CCLSD can be measured in experiments. We think it may be possible with modern scanned-probe techniques. However, this task would require probing a current-carrying system with a nanoscale spatial resolution. One somewhat indirect method is to utilize the scanned gate microscopy (SGM), in which the change of the conductance of the system is measured in response to a local gating by the scanned tip. With further analysis, this type of measurement can in principle reveal the CCLCD.[EBT$^+$96, TLS$^+$00, TLW$^+$01, BBHW10, SHP$^+$11, ManKanS14] A more direct method is the scanned tunneling potentiometry (STP) [MP86] recently implemented to study current-carrying graphene.[WMRB13] By incorporating magnetized scanned probes into the SGM and STP, it may also become possible to study the predicted patterns of the local spin density on a surface of a topological insulator.

2.7 Discussion and conclusions

Several remarks are in order before we conclude. First, the transport properties of graphene have provided a major motivation for this study. Since there have already

been numerous previous theoretical investigations of this subject, it may be worthwhile to draw attention to the points where we find qualitatively different results. Recall that the two most common models of scatterers in graphene are random (uncorrelated) charged impurities and random short-range defects. For the former, the theory predicts the linear dependence of the conductivity on the electron density n_e, for the latter the conductivity is roughly density-independent.[Per10, DSAHR11] Introducing some degree of correlations among the impurity positions into these basic models modifies the conductivity dependence quantitatively [LHRDS11] but preserves this main dichotomy. In contrast, in our model the conductance has an approximately $\sqrt{n_e}$ dependence [Eq. (2.26)] if the potential barrier is strong enough, $\rho > 1$. Let us give a specific example. Suppose the potential scatterers of our model are formed by aggregation of charged impurities with average density $10^{13}\,\mathrm{cm}^{-2}$ into circular clusters inside of which the distances between the impurities is about $1\,\mathrm{nm}$. From the conservation of the total impurity number one concludes that in this model there is an inverse relation between the density n_c of the clusters and their radius a:

$$n_c \sim 0.03 a^{-2} \,. \tag{2.75}$$

Substituting this formula into Eq. (2.26), we obtain an estimate of the conductivity

$$G \sim 100 \frac{e^2}{h} \sqrt{n_e} a \,, \tag{2.76}$$

which exhibits the $\sqrt{n_e}$-behavior. Since G is proportional to a, formation of clusters greatly increases the conductivity[KGG09] in comparison to the case of random isolated impurities. This conclusion is further strengthened by the large numerical factor in

Eq. (2.76).

The lifetime ratio η [Eq. (2.1)] is another fundamental parameter characterizing the transport properties of the system. Most of previous calculations of η have been limited to the perturbation theory (the Born approximation), which predicts $\eta \geq 2$ for the charged and $1 \leq \eta \leq 2$ for the short-ranged defects. As we point out in Sec. 2.2 and illustrate in Fig. 2.8(c), η can be less than 2 and even less than 1 for small-radius scatterers because of the resonant tunneling, a non-perturbative effect. Conversely, for large-radius scatterers, η can be very large, see Fig. 2.8(a). Note that the small lifetime ratio $\eta < 2$ observed in some experiments[HZZ09, TAT$^+$13] while large $\eta \sim 6$ is found in some others. [Gor09]

Next, we wish to address the validity of our step-like model of the potential barrier. If the potential is indeed created by a cluster of charged impurities, this model is oversimplified. The actual potential has no discontinuity. Instead, it sharply but continuously drops over a distance of the order of the screening length, which is usually comparable to the Fermi wavelength.[CNGP$^+$09] For such a smooth boundary, the reflection and transmission coefficients that enter the ray formula Eq. (2.29b) are modified, e.g., the reflection coefficient is enhanced.[CF06, ZF08] Therefore, the transport and total cross-sections should be greater than what we calculated for a sharp boundary. The correction is relatively small if both X and X' are large, so that the radius of the cluster is much larger than the Fermi wavelength on both sides of the boundary. However, if either exterior or interior of the cluster is doped weakly, a more accurate calculation will be necessary. Another omission of the step-like model is the long-range tail of the screened Coulomb potential induced by the cluster. For high Fermi energy the screening is strong and the effect of such a tail can be treated

perturbatively. A weak long-range potential tail would cause additional small-angle scattering, which should make only a small correction to the transport cross-section. The effect on the total cross-section could be more substantial. Within the HEA, the contribution of the long-range potential tail to the total cross-section is given by [LL77]

$$\Delta\sigma \simeq \frac{8a}{X} \int_0^\infty [\sin^2(\delta_j + \Delta\delta_j) - \sin^2\delta_j]\, dj\,, \tag{2.77}$$

$$\Delta\delta_j \simeq -\frac{1}{\hbar v_F} \int_{\max(a,b)}^\infty \frac{V(r)r\,dr}{\sqrt{r^2 - b^2}}\,, \quad b = \frac{ja}{X}\,. \tag{2.78}$$

It is well known that an external charge screened by a gas of 2D electrons (either massive or massless) produces the potential that behaves as $V(r) \propto r^{-3}$ at distances much larger than the screening length. It is then easy to see that the integral in Eq. (2.77) converges. Thus, there should be a range of parameters where neglecting $\Delta\sigma$ is legitimate. However, for massless Dirac fermions, large enough total charge of the cluster, and low enough Fermi energy, the screened potential would exhibit a slower decay $V(r) \propto r^{-3/2}$ over a range of intermediate distances.[FNS07] According to Eq. (2.77), this may yield logarithmic corrections to the total cross-section. This interesting problem warrants further study.

In conclusion, we studied in some depth scattering of massless Dirac fermions by a step-like circular potential. We unified many possible scattering regimes into a single global diagram (Fig. 2.3) and presented analytical and numerical results for the scattering amplitude in each of the individual regimes. We verified that the semiclassical ray formalism accounts for most of the scattering properties in the large-X regimes and at the same time provides an intuitive physical description of both the

far-field and near-field scattering. We showed that the ray picture applies even for weak scattering potentials, which is the case where the semiclassical method is usually eschewed in favor of quantum scattering theory. We also discussed phenomena beyond the ray picture, such as the regularization of the divergence of the scattering amplitude at the rainbow angle and the quantization of the whispering-gallery resonances. While the perfect axial symmetry and the step-like discontinuity of the potential barrier that enabled us to make progress in terms of analytical theory are not fully realistic, some of our non-perturbative semiclassical techniques can be extended to barriers of more general shapes and profiles. It will be intriguing to apply our non-perturbative semiclassical techniques to other graphene systems, such as bilayer graphene and graphene with mass barriers.[MP08, RMVP11, RMMP11, RMP13] We expect that substantially different results for bilayer graphene and graphene with mass barriers because their gapped band structures suppress the Klein tunneling. The approach and the types of regimes will be the same. However, the positions of the regime boundaries and the angular dependence of the differential cross-sections will change. Finally, we hope that our results may stimulate future transport and scanned-probe experiments with graphene and topological insulators.

2.8   Partial wave decompostion

In order to make the paper self-contained, in this Appendix we review the partial wave series. Using the notations of Ref. [CPP07] we denote by $h_j^{(2)}$ and $h_j^{(1)}$, respectively, the incoming and the outgoing waves of angular momentum j. At $r > a$,

where $V(r) = 0$, such waves are given by

$$h_j^{(d)}(r, \phi) = \begin{pmatrix} H_{j-1/2}^{(d)}(kr)e^{-i\phi/2} \\ iH_{j+1/2}^{(d)}(kr)e^{i\phi/2} \end{pmatrix} e^{ij\phi}. \qquad (2.79)$$

The angular momenta j are half integers, so that $h_j^{(d)}$ are single-valued. At $0 \leq r < a$, the solutions that are well-behaved at the origin are

$$\chi_j(r, \phi) = \begin{pmatrix} J_{j-1/2}(k'r)e^{-i\phi/2} \\ iJ_{j+1/2}(k'r)e^{i\phi/2} \end{pmatrix} e^{ij\phi} \qquad (2.80)$$

with $k' = (E - V_0)/(\hbar v_F) = X'/a$. Equation (2.80) can be used for both positive and negative k'. In the latter case, a n-p junction forms at the boundary of the scatterer.

In the partial wave method, the scattering wavefunction Ψ is expanded as follows. At $r > a$, it is given by

$$\Psi = \frac{1}{\sqrt{2}} \begin{pmatrix} 1 \\ 1 \end{pmatrix} e^{ikx} + \frac{e^{-\frac{i\pi}{4}}}{2\sqrt{2}} \sum_j i^j \left(e^{2i\delta_j} - 1\right) h_j^{(1)}, \qquad (2.81)$$

where the coefficient in front of the sum is chosen to match the coefficient in a similar expansion of the incident plane wave (the first term). At $r < a$, we have

$$\Psi = \frac{e^{-\frac{i\pi}{4}}}{2\sqrt{2}} \sum_j i^{(j-1/2)} B_j \chi_j. \qquad (2.82)$$

By imposing the continuity of the wavefunction at $r = a$, it is straightforward to find

$$e^{2i\delta_j} = -\frac{s_j^*}{s_j}, \tag{2.83}$$

$$s_j = H^{(1)}_{j+1/2}(X)J_{j-1/2}(X') - H^{(1)}_{j-1/2}(X)J_{j+1/2}(X'), \tag{2.84}$$

$$B_j = \frac{H^{(1)}_{j+1/2}(X)H^{(2)}_{j-1/2}(X) - H^{(1)}_{j-1/2}(X)H^{(2)}_{j+1/2}(X)}{s_j}. \tag{2.85}$$

Applying the asymptotic expansion for Hankel function [Eq. (2.92)] at large argument, the second term of Eq. (2.81) yields the scattering amplitude $f(\phi)$ [Eq. (2.6)].

2.9 Debye and ray series

To derive the ray series, we first decompose $e^{2i\delta_j}$ in Eq. (2.83) into the Debye series[Gra00]

$$e^{2i\delta_j} = R_{22} + \sum_{p=1}^{\infty} T_{21}T_{12}(R_{11})^{p-1}, \tag{2.86}$$

where

$$R_{22} = \frac{H^{(2)}_{j+1/2}(X)H^{(2)}_{j-1/2}(X') - H^{(2)}_{j-1/2}(X)H^{(2)}_{j+1/2}(X')}{d_j}, \tag{2.87}$$

$$T_{21} = \frac{H^{(2)}_{j-1/2}(X)H^{(1)}_{j+1/2}(X) - H^{(2)}_{j+1/2}(X)H^{(1)}_{j-1/2}(X)}{-d_j}, \tag{2.88}$$

$$d_j \equiv H^{(1)}_{j-1/2}(X)H^{(2)}_{j+1/2}(X') - H^{(1)}_{j+1/2}(X)H^{(2)}_{j-1/2}(X'). \tag{2.89}$$

Coefficient R_{11} (T_{12}) is obtained from R_{22} (T_{12}) by interchanging 1 with 2 and X' with X. These R's and T's should not be confused with the plane-wave reflection and

transmission coefficients such as R_{in} and T_{in} in Sec. 2.3.

The scattering amplitude Eq. (2.6) can be now written as

$$f(\phi) = -\frac{i}{\sqrt{2\pi k}} \sum_{p=0}^{\infty} \sum_{j} D_p e^{i(j-1/2)\phi} , \qquad (2.90)$$

with $D_0 = R_{22}$, $D_1 = T_{12}T_{21} - 1$ and $D_p = T_{12}T_{21}R_{11}^{p-1}$ for $p > 1$. Using the Poisson summation formula, we obtain

$$\sum_{j} D_p e^{i(j-1/2)\phi} = \sum_{m=-\infty}^{\infty} \int_{-\infty}^{\infty} d\lambda D_p e^{i\lambda(\phi+2m\pi)} , \qquad (2.91)$$

with $\lambda = j - 1/2$. For $|\lambda - X| > X^{1/3}$, we can use the Debye expansion of the Hankel function,

$$H_\lambda^{(1,2)}(X) \simeq \left(\frac{2}{\pi}\right)^{1/2} (X^2 - \lambda^2)^{-1/4}$$
$$\times \exp\left\{\pm i\left[\sqrt{X^2 - \lambda^2} - \lambda\cos^{-1}(\lambda/X) - \pi/4\right]\right\} , \qquad (2.92)$$

valid for $|\lambda| < x$, to approximate D_p. After some tedious algebra, we find

$$D_p \simeq \begin{cases} C_1(\alpha)e^{2i\delta_1} - 1, & p = 1 , \\[2mm] C_p(\alpha)e^{2i\delta_p}, & p \neq 1 , \end{cases} \qquad (2.93)$$

where $C_p(\alpha)$ is defined in Eq. (2.34) and δ_p is given by

$$\delta_p = -\left[X\cos\alpha - \lambda\left(\frac{\pi}{2} + \alpha\right) - \frac{\pi}{4}\right]$$
$$+ p\left[X'\cos\beta - \lambda\left(\frac{\pi}{2} + \beta\right) - \frac{\pi}{4}\right] , \qquad (2.94)$$

with

$$\alpha = -\sin^{-1}\left(\frac{\lambda}{X}\right), \quad \beta = -\sin^{-1}\left(\frac{\lambda}{X'}\right). \tag{2.95}$$

It can be shown that D_p becomes very small at $\lambda > X$ for all p. (For $p = 1$, having -1 term in D_1 is essential for this property.) Thus, the infinite integration limits in Eq. (2.91) can be replaced by $\pm X$. The integrand has a saddle-point determined by the condition

$$2\frac{d\delta_p}{d\lambda} + \phi + 2m\pi = 0. \tag{2.96}$$

Applying the saddle-point approximation, we obtain Eq. (2.29b).

2.10   Acknowledgement

Chapter 3

Topological insulators are tunable waveguides for hyperbolic phonon polaritons

3.1 Introduction

Bismuth-based topological insulators (TIs) have attracted much interest for their unusual electron surface states (SSs), which behave as Dirac fermions. [HK10, QZ11] However, bulk optical response of these compounds [RKB77, LFP$^+$10, CR11, ATU$^+$12, DPVN$^+$12, DOL$^+$13, WBVA$^+$13, PCH$^+$13, CPR$^+$14, RTS$^+$14, AED$^+$15, ADDG$^+$15, PCL$^+$15] is also remarkable. The quintuple-layered structure of these materials causes a strong anisotropy of their phonon modes. The E_u phonons that involve atomic displacements in the plane parallel to the basal plane (henceforth, x–y or $\perp$–plane) have lower frequencies than A_{2u}, the c-axis (henceforth, z-axis)

vibrations.[CR11] For Bi_2Se_3, the dominant $\perp$- and z-axis phonon frequencies,

$$\omega^{\perp}_{1,to} = 64\,\text{cm}^{-1} \quad = 1.9\,\text{THz}\,,$$
$$\omega^{z}_{1,to} = 135\,\text{cm}^{-1} = 4.1\,\text{THz}\,,$$

<div align="right">(3.1)</div>

differ more than twice. As a result, this and similar TIs can exhibit a giant anisotropy of the dielectric permittivity. There is a range of ω where the permittivity tensor is indefinite: the real part of $\epsilon^z(\omega)$ is positive, while that of $\epsilon^{\perp}(\omega)$ is negative. Media with such characteristics are referred to as hyperbolic [GNJ12, PIBK13, SLZ14] because the isofrequency surfaces of their extraordinary rays in the momentum space $\mathbf{k} = (k^x, k^y, k^z)$ are shaped as hyperboloids [Fig. 3.1(a)]. In the THz domain, the widest band of frequencies where Bi_2Se_3 behaves as a hyperbolic medium (HM) is between the aforementioned dominant frequencies, $\omega^{\perp}_{to,1} < \omega < \omega^{z}_{to,1}$; however, other hyperbolic bands also exist in this TI (both at THz frequencies, see Sec. 3.2, and at visible frequencies, see Ref. [EVT$^+$14]). It is important that the approximate equation for the extraordinary isofrequency surfaces,

$$\frac{(k^x)^2 + (k^y)^2}{\epsilon^z(\omega)} + \frac{(k^z)^2}{\epsilon^{\perp}(\omega)} = \frac{\omega^2}{c^2}\,,$$

<div align="right">(3.2)</div>

is valid up to $|\mathbf{k}|$ of the order of the inverse lattice constant. Accordingly, rays of momenta $|\mathbf{k}|$ greatly exceeding the free-space photon momentum ω/c can propagate through hyperbolic materials without evanescent decay. At such $\mathbf{k}$ the hyperboloids can be further approximated by cones, which means that the group velocity $\mathbf{v} = \partial\omega/\partial\mathbf{k}$
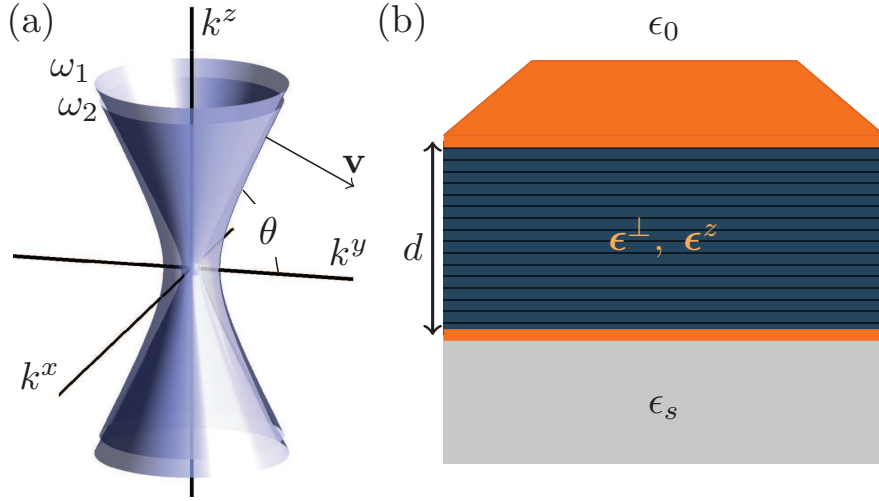
Figure 3.1: (Color online) (a) Hyperboloidal isofrequency surfaces of HP^{2}s for two frequencies ω_1 and ω_2 ($\omega_2 > \omega_1$). The asymptote angle θ with respect to the k^x–k^y plane is shown; the group velocity **v** makes the same angle with respect to the k^z-axis. (b) Model geometry: a TI slab of thickness d sandwiched between a substrate of permittivity ϵ_s and a superstrate of permittivity ϵ_0. The two thin (orange) layers represent the top and the bottom surfaces states.

of the rays makes a *fixed* angle θ (or $-\theta$) with respect to the z-axis, with

$$\tan \theta(\omega) = i \, \frac{[\epsilon^{\perp}(\omega)]^{1/2}}{[\epsilon^z(\omega)]^{1/2}} \,, \tag{3.3}$$

see Fig. 3.1(a). We refer to these deeply subdiffractional, highly directional modes as the hyperbolic phonon polaritons (HPP or HP^2, for short).

Our interest to HP^2 of TIs is stimulated by recent discovery [DFM$^+$14, Jac14] and further exploration of similar collective modes in other systems such as hexagonal boron nitride [CKC$^+$14, DMA$^+$15, LLK$^+$15, SBB$^+$15] (hBN) and hBN covered by graphene [BJS$^+$13, DML$^+$15, NWW$^+$15] (hBN/G). There is a close analogy between these systems. In fact, except for the difference in the number of Dirac cones ($N = 1$

vs. $N = 4$) and the frequency range where the hyperbolic response occurs (THz *vs.* mid-infrared), the electrodynamics of longitudinal collective modes of Bi_2Se_3 and hBN/G structures is qualitatively the same. (The analogy is the most faithful when graphene and hBN are rotationally misaligned; otherwise, their collective modes are modified by the moiré superlattice effects. [TGP14, NWW$^+$15])

The main goal of this paper is to investigate the interaction of HP^2 with the Dirac plasmons of the topological SS. The latter dominate the charge (and current) density response of the system at frequencies outside the hyperbolic band where HP^2 are absent. Dirac plasmons have been extensively studied in previous literature [CNGP$^+$09, HDS09, RCQZ10, FAB$^+$11, FRA$^+$12, CBAG$^+$12, GPN12, PAPM12, GdA14, BFL$^+$14b, DOL$^+$13, SGSB13, SETH13, QLX14, LDC$^+$14, Sta14, AED$^+$15, ADDG$^+$15] on both TI and graphene. The basic properties of the Dirac plasmons can be introduced on the example of a hypothetical TI material with a frequency-independent permittivity $\epsilon^z > 0$ and the permittivity $\epsilon^\perp(\omega)$ dominated by a single phonon mode. Such an idealized material is hyperbolic in a single frequency interval $\omega_{to} < \omega < \omega_{lo}$ where $\epsilon^\perp(\omega) < 0$. Its Dirac plasmons exist at $\omega < \omega_{to}$ and $\omega > \omega_{lo}$ where $\epsilon^\perp(\omega) > 0$. In the setup shown in Fig. 3.1(b), where the TI slab borders media of constant permittivities $\epsilon_0 > 0$ and $\epsilon_s > 0$, there are two plasmon modes. At large enough in-plane momenta $q \equiv [(k^x)^2 + (k^y)^2]^{1/2}$ these modes are confined to the opposite interfaces and electromagnetically decoupled. In the relevant range of momenta $q < q_*$, the dispersion of the plasmon bound to the top interface is given by

$$q(\omega) \simeq \frac{4}{N} \frac{\epsilon_0 + \epsilon_1}{e^2 |\mu|} (\hbar\omega)^2, \quad \hbar\omega \ll |\mu|, \tag{3.4}$$

where

$$\epsilon_1(\omega) = [\epsilon^\perp(\omega)]^{1/2} [\epsilon^z(\omega)]^{1/2}, \tag{3.5}$$

is the effective permittivity of the TI and μ is the chemical potential of the SSs measured from the Dirac point. At frequencies far below ω_{to} or far above ω_{lo}, function $\epsilon_1(\omega)$ can be approximated by a real constant, which yields $\omega \propto \sqrt{q}$. This typical two-dimensional (2D) plasmon dispersion describes the low-frequency part of the full curve sketched in Fig. 3.2(a). The plasmon dispersion for the bottom interface is obtained by replacing ϵ_0 with ϵ_s (unless $\epsilon_s \gg \epsilon_0$, in which case the range $q > q_*$ is relevant where the dispersion is approximately linear, see Sec. 3.3.2).

Equation (3.4) implies that the nature of the plasmon modes should change drastically when ω enters the hyperbolic frequency band where $\epsilon_1(\omega)$ [Eq. (3.5)] is imaginary and strongly ω-dependent. This equation predicts a complex q, which suggests that the Dirac plasmons become leaky modes that rapidly decay into the HP^2 bulk continuum. However, this is not quite correct. We will show that nonleaky, i.e., propagating modes can survive in thin enough TI slabs where the HP^2 continuum is broken into discrete subbands of *waveguide* modes. The latter hybridize with plasmons to form hyperbolic plasmon phonon polaritons (HPPP or HP^3, for short), the primary target of our investigation, see Figs. 3.2(b) and (c). We explore the following properties and manifestations of the collective charge modes of the TIs: i) the mode dispersion in the momentum-frequency space, ii) the dependence of such dispersions on the surface doping and the thickness of the slab, iii) the unusual real-space dynamics of the HP^3 rays, including a polaritonic analog of the Goos-Hänchen (GH) effect. [GH47, BA13]

The remainder of the paper is organized as follows. In Sec. 3.2 we specify the model and the basic equations. In Sec. 3.3 we present our results for the dispersion of

61
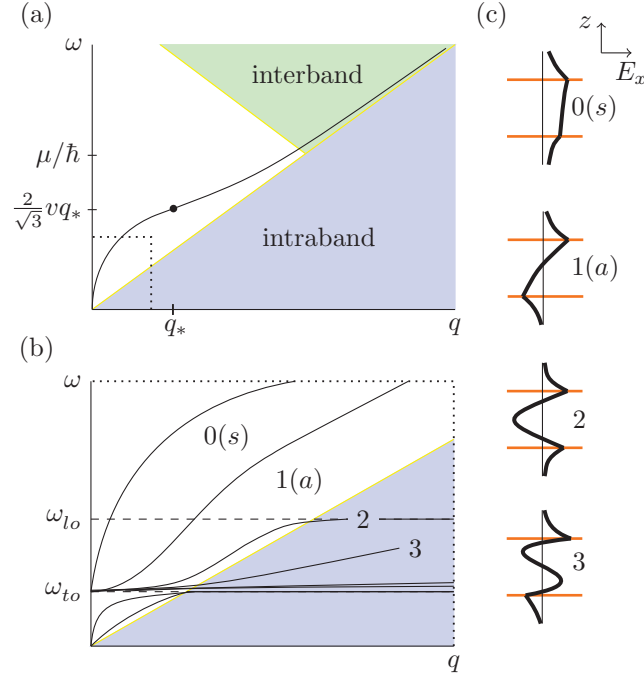
Figure 3.2: (Color online) Schematic illustrations of the collective mode spectra in idealized model systems. (a) The plasmon dispersion of Dirac fermions confined to the interface of two bulk media of constant positive permittivity ϵ_0 and ϵ_s. The dispersion crosses over from $\omega \simeq v\sqrt{qq_*/2}$ to $\omega \simeq vq$ at a characteristic momentum q_* [Eq. (3.26)]. The shaded areas indicate the electron-hole continua where the plasmons (and any other charged collective modes) are damped. (b) The dispersion of hybrid HP^3 modes for a slab of a hypothetical TI material that has a single in-plane phonon mode at ω_{to} and constant $\epsilon^z > 0$. Permittivity $\epsilon^\perp$ is negative at $\omega_{to} < \omega < \omega_{lo}$ and positive at other ω. The dotted boundary corresponds to the dotted line in (a). Outside the band $\omega_{to} < \omega < \omega_{lo}$, only plasmonic modes 0 and 1 exist. In the degenerate case $\epsilon_0 = \epsilon_s$ they correspond to the symmetric (s) and antisymmetric (a) combinations of the top and bottom interface plasmons. Inside that band, multiple branches of HP^3 are formed due to hybridization of the plasmons with the HP^2 waveguide modes. The frequencies of all the branches other than 0 and 1 tend to ω_{lo} at large momenta. (c) Schematic in-plane electric field profiles of the first few HP^3 modes (thick curves). The number of nodes in each profile (the points where they cross with the vertical lines $E_x = 0$) is equal to the modal index.

the three different types of collective modes (plasmons, HP^{2}s, and HP^{3}s). In Sec. 3.4, which is the centerpiece of this work, we discuss waveguiding and launching of the HP^2 modes and also their tunable GH shifts. We explain how these phenomena can be probed experimentally using the imaging capabilities of the scattering-type scanning near-field optical microscopy (s-SNOM). [KH04, ABJR12] In Sec. 3.5 we give concluding remarks and an outlook for the future. Finally, in Appendix we discuss signatures of the phonon-plasmon coupling measurable by the s-SNOM operating in the spectroscopic mode.

3.2 Model

Our model for the bulk permittivities of the TI is

$$\epsilon^\alpha(\omega) = \epsilon^\alpha_\infty + \sum_{j=1,2} \frac{\omega^{\alpha\,2}_{p,j}}{\omega^{\alpha\,2}_{to,j} - \omega^2 - i\gamma^\alpha_j \omega}\,, \quad \alpha = \perp, z\,. \tag{3.6}$$

In the case of Bi$_2$Se$_3$, we choose the parameters based on available experimental [RKB77, LFP$^+$10, DPVN$^+$12] and theoretical [CR11] literature as follows: $\epsilon^\perp_\infty = 29$, $\epsilon^z_\infty = 17.4$, $\omega^\perp_{to,1} = 64\,\mathrm{cm}^{-1}$, $\omega^\perp_{p,1} = 704\ \mathrm{cm}^{-1}$, $\omega^\perp_{to,2} = 125\,\mathrm{cm}^{-1}$, $\omega^\perp_{p,2} = 55\,\mathrm{cm}^{-1}$, $\omega^z_{to,1} = 135\,\mathrm{cm}^{-1}$, $\omega^z_{p,1} = 283\,\mathrm{cm}^{-1}$, $\omega^z_{to,2} = 154\,\mathrm{cm}^{-1}$, $\omega^z_{p,2} = 156\,\mathrm{cm}^{-1}$, and $\gamma^\alpha_j = 3.5\,\mathrm{cm}^{-1}$. [Note that $\omega^\perp_{to,1}$ and $\omega^z_{to,1}$ were already listed in Eq. (3.1).] The real parts of functions $\epsilon^\perp(\omega)$ and $\epsilon^z(\omega)$ are plotted in Fig. 3.3. The regions where at least one of them is negative are shaded. They include region A, $\omega^\perp_{to,1} < \omega < \omega^z_{to,1}$, where Bi$_2Se_3$ is a HM of type II ($\Re\mathrm{e}\,\epsilon_z > 0$, $\Re\mathrm{e}\,\epsilon^\perp < 0$); region C, $\omega^z_{to,2} < \omega < 163\,\mathrm{cm}^{-1}$ where it is a HM of type I ($\Re\mathrm{e}\,\epsilon_z < 0$, $\Re\mathrm{e}\,\epsilon^\perp > 0$), and region B, $\omega^z_{to,1} < \omega < 146\,\mathrm{cm}^{-1}$, where it exhibits the Reststrahlen behavior ($\Re\mathrm{e}\,\epsilon_z < 0$, $\Re\mathrm{e}\,\epsilon^\perp < 0$). Since regions B and C are narrow,

in our discussion of HP^2 and HP^3 modes we focus on region A. In this discussion we often refer to hBN as an example of a simpler material. The type II hyperbolic band of hBN is bounded by the frequencies [DFM$^+$14, CKC$^+$14]

$$\omega_{to} = 1376\,\text{cm}^{-1}, \quad \omega_{lo} = 1614\,\text{cm}^{-1}. \tag{3.7}$$

In this band $\epsilon^\perp(\omega)$ of hBN can be modelled similar to Eq. (3.6) but using a single Lorentzian oscillator while ϵ^z can be considered ω-independent and positive.

In the case of Bi_2Se_3, we also have to specify our assumptions about the electronic response. We consider only frequencies smaller than the bulk gap $0.3\,\text{eV}$ of Bi_2Se_3 at which the electronic contribution to the permittivities [included in Eq. (3.6) via ϵ_∞^α] is purely real. Additionally, we assume that the valence bulk band is completely filled, the conduction one is empty, with no free carriers present in the bulk. However, such carriers populate the gapless SS described by the massless 2D Dirac equation. The chemical potential μ, which is located inside the bulk band gap, determines the doping of these SS. For simplicity, we ignore any virtual or real electronic transitions between the surface and the bulk states, which should not change the result qualitatively, except perhaps for the additional damping from these transitions.

The fundamental current/density response functions of the SS are the sheet conductivity σ and polarizability P, which are related in the standard way:

$$\sigma(q,\omega) = \frac{i\omega}{q^2}\,e^2 P(q,\omega). \tag{3.8}$$

Within the random-phase approximation for Dirac fermions, $P(q,\omega)$ can be com-
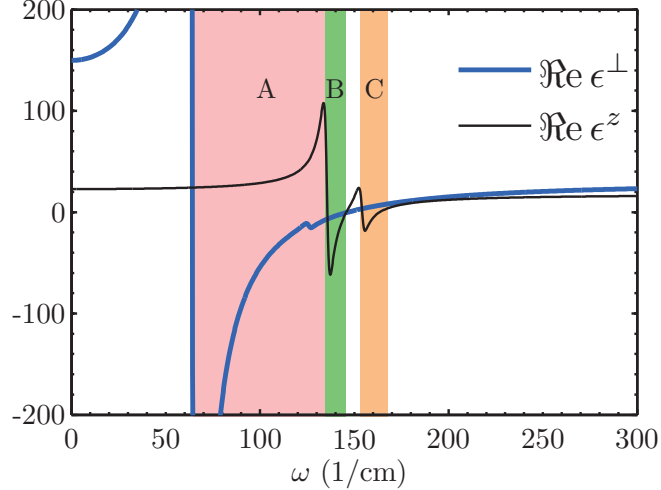
Figure 3.3: (Color online) The real parts of the tangential and axial permittivities of Bi_2Se_3. The sign changes of the permittivities are due to the E_u and A_{2u} phonons. Surface- and bulk-confined collective modes exist inside the spectral regions where at least one of the permittivitties is negative. They include type II hyperbolic region A ($\Re e\,\epsilon^\perp < 0$, $\Re e\,\epsilon^z > 0$), Reststrahlen region B ($\Re e\,\epsilon^\perp, \Re e\,\epsilon^z < 0$), and type I hyperbolic region C ($\Re e\,\epsilon^\perp > 0$, $\Re e\,\epsilon^z < 0$).

puted [WSSG06, HDS07] analytically:

$$P(q,\omega) = -\frac{Nk_F}{2\pi\hbar v} - \frac{iN}{16\pi\hbar v}\frac{q^2}{\sqrt{q^2 - k_\omega^2}}$$
$$\times \left[G\left(\frac{k_\omega + 2k_F}{q}\right) - G\left(\frac{k_\omega - 2k_F}{q}\right) - i\pi \right], \qquad (3.9)$$
$$G(x) = ix\sqrt{1 - x^2} - i\arccos x\,.$$

Here the branch cut for the square root and logarithm functions is the negative real semi-axis, k_ω is defined by $k_\omega = (\omega + i\gamma_e)/v$, phenomenological parameter $\gamma_e > 0$ is the electron scattering rate, v is the Fermi velocity, and $k_F = |\mu|/(\hbar v)$ is the Fermi momentum. Equation (3.9) is a good approximation at small μ. At large doping, trigonal warping [LC14] and other details of realistic band-structure [LDC+14] should be included. Since the above formula is a bit cumbersome, it may be helpful to

mention some properties of $\sigma(q, \omega)$. For example, if $\gamma_e = +0$, the real part of $\sigma(q, \omega)$ is nonvanishing only inside the two shaded areas in Fig. 3.2(a), which together form the so-called electron-hole continuum. [CNGP$^+$09, BFL$^+$14b] (This real part is a measure of dissipation, i.e., Landau damping.) For doped system at small momenta and frequencies, $q, k_\omega \ll k_F$, the expression for the conductivity can be reduced to

$$\sigma(q, \omega) \simeq \frac{Ne^2}{2\pi\hbar} \frac{k_F}{\sqrt{q^2 - k_\omega^2}} \frac{ik_\omega}{ik_\omega - \sqrt{q^2 - k_\omega^2}} . \tag{3.10}$$

At $q \ll \omega/v$, it further simplifies to the Drude formula

$$\sigma \simeq \frac{Ne^2}{4\pi\hbar^2} \frac{|\mu|}{\gamma_e - i\omega} , \quad \mu \neq 0 . \tag{3.11}$$

For an undoped system, one finds instead

$$\sigma(q, \omega) = \frac{N}{16} \frac{e^2}{\hbar} \frac{ik_\omega}{\sqrt{q^2 - k_\omega^2}} \tag{3.12}$$

$$\simeq \frac{N}{16} \frac{e^2}{\hbar} , \quad q \ll \frac{\omega}{v} . \tag{3.13}$$

In order to find the dispersion of the collective modes of the TI slab we use two computational methods. One method, which is advantageous for deriving analytical results, is to look for the poles of the response function $r_P(q, \omega)$. This function is the total P- (also known as the TM-) polarization reflectivity of the system measured when an external field is incident from the medium labeled "ϵ_0" in Fig. 3.1(b). It must be immediately clarified that $r_P(q, \omega)$ has no poles at simultaneously real q and ω if the dissipation parameters γ and γ_e are nonzero. At least one of these arguments must be complex. Whenever one refers to the dispersion relation of a mode, one means
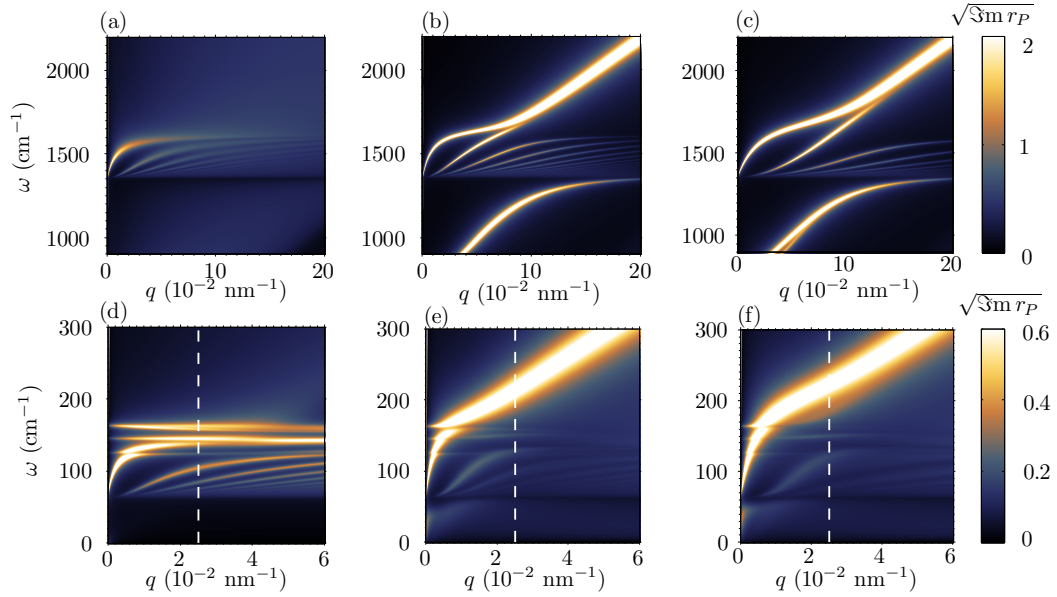
Figure 3.4: (Color online) Collective mode dispersions of graphene-hBN-graphene (G/hBN/G) and Bi_2Se_3 slabs rendered using the false color maps of $\Im m\, r_P$. The parameters of the calculation for G/hBN/G are: (a) $d = 60$ nm, $\mu = 0$, (b) $d = 60$ nm, $\mu = 0.29$ eV, (c) $d = 30$ nm, $\mu = 0.29$ eV. The other parameters are $v = 1.00 \times 10^8$ cm/s, $\gamma_e = 1.00$ THz, $\epsilon_0 = 1$, and $\epsilon_s = 1.5$. The parameters of the calculation for Bi_2Se_3 are: (d) $d = 120$ nm, $\mu = 0$, (e) $d = 120$ nm, $\mu = 0.29$ eV, (f) $d = 60$ nm, $\mu = 0.29$ eV. In these three plots $v = 0.623 \times 10^8$ cm/s, $\gamma_e = 1$ THz, $\epsilon_0 = 1$, and $\epsilon_s = 10$. Equal doping of the top and bottom SS is assumed. The vertical dashed lines indicate a characteristic momentum probed by the s-SNOM experiments simulated in Fig. 3.7 below.

the relation between the real parts of q and ω. The other method, which is especially convenient for numerical simulations, is to identify the sought dispersion curves with the maxima of $\Im m\, r_P(q, \omega)$ at *real* arguments. As long as the imaginary parts of q and ω (which give information about the propagation length and lifetime of the mode) are small, both methods give the same dispersions. An extra benefit of working with real q and ω is that the corresponding $r_P(q, \omega)$ is the input for further calculations we discuss in Appendix 3.6 where we model s-SNOM experiments for the system in hand.

Our procedure for calculating function $r_P(q, \omega)$ can be explained as follows.

Taking a more general view for a moment, we regard the entire system including the substrate and superstrate as a stack of layers $j = 0, 1, \ldots, M$ of thickness d_j, tangential permittivity $\epsilon_j^\perp$, and axial permittivity ϵ_j^z. (In the present case, $M = 2$, the TI slab is layer $j = 1$ and $d_1 = d$.) Additionally, we assume that the interface of the layers j and $j + 1$ possesses the sheet conductivity $\sigma_{j,j+1}$. We observe that the P-polarization reflectivity $r_{j,j+1}$ of $j, j + 1$ interface in isolation is given by the formula (see, e.g., Ref. [DML$^+$15])

$$r_{j,j+1} = \frac{Q_{j+1} - Q_j + \dfrac{4\pi}{\omega}\sigma_{j,j+1}}{Q_{j+1} + Q_j + \dfrac{4\pi}{\omega}\sigma_{j,j+1}}, \tag{3.14}$$

$$Q_j = \frac{\epsilon_j^\perp}{k_j^z}, \quad k_j^z = \sqrt{\epsilon_j^\perp}\sqrt{\frac{\omega^2}{c^2} - \frac{q^2}{\epsilon_j^z}}, \tag{3.15}$$

where k_j^z and q are, respectively, the axial and the tangential momenta inside layer j. Let r_j be the reflectivity of a subsystem composed of layers $j, \ldots, M$. By this definition, $r_{M-1} = r_{M-1,M}$. The crucial point is that the desired $r_P \equiv r_0$ can be found by the backward recursion

$$r_j = r_{j,j+1} - \frac{(1 - r_{j,j+1})(1 - r_{j+1,j})r_{j+1}}{r_{j+1,j}r_{j+1} - \exp(-2ik_{j+1}d_{j+1})}, \tag{3.16}$$

where $r_{j+1,j}$ is the right-hand hand of Eq. (3.14) with Q_j and Q_{j+1} interchanged. For $M = 2$, one recursion step suffices, which gives us, after some algebra, [DML$^+$15]

$$r_P = \frac{r_{12}(r_{01} + r_{10} - 1) - r_{01}\exp(-2ik_1d_1)}{r_{10}r_{12} - \exp(-2ik_1d_1)}. \tag{3.17}$$

Hence, function $r_P(q, \omega)$ has poles whenever

$$r_{10}(q, \omega) r_{12}(q, \omega) = \exp\left(-2i k_1^z d\right).\tag{3.18}$$

For large in-plane momenta $q \gg (\omega/c) \max |\epsilon_j^z|^{1/2}$, we can use the approximations $k_1^z \simeq q \tan\theta$ and

$$r_{10} \simeq \frac{\epsilon_0 - \epsilon_1 - \frac{2q}{q_{\text{top}}}}{\epsilon_0 + \epsilon_1 - \frac{2q}{q_{\text{top}}}}, \qquad q_{\text{top}} \equiv \frac{i\omega}{2\pi\sigma_{\text{top}}},\tag{3.19}$$

where $\sigma_{\text{top}} = \sigma_{\text{top}}(q, \omega)$ is the sheet conductivity of the SS at the top interface. Let us also define the "phase shifts" ϕ_{top} and ϕ_{bot} for inner reflections from the top and bottom interfaces, respectively: $r_{10} = -\exp(2i\phi_{\text{top}})$, $r_{12} = -\exp(2i\phi_{\text{bot}})$. Note that in general ϕ_{top} and ϕ_{bot} are complex numbers. Specifically, we take

$$\phi_{\text{top}} = \arctan\left[i\,\frac{\epsilon_0}{\epsilon_1}\left(1 - \frac{2}{\epsilon_0}\frac{q}{q_{\text{top}}}\right)\right],\tag{3.20}$$

$$\phi_{\text{bot}} = \arctan\left[i\,\frac{\epsilon_s}{\epsilon_1}\left(1 - \frac{2}{\epsilon_s}\frac{q}{q_{\text{bot}}}\right)\right].\tag{3.21}$$

where the standard definition of $\arctan z$ is assumed, with the branch cuts $(-i\infty, -i)$, $(i, i\infty)$ in the complex-z plane; q_{bot} is defined analogously to q_{top} but with the sheet conductivity σ_{bot} of the bottom SS instead of σ_{top}. Equation (3.18) can now be transformed to

$$q_n = -\frac{2}{\delta}(n\pi + \phi_{\text{top}} + \phi_{\text{bot}}), \qquad \delta \equiv 2d \tan\theta,\tag{3.22}$$

where the integer subscript n labels possible multiple solutions. Admissible n must satisfy the condition $\Im m\, r_P(q_n, \omega) > 0$. Our numerical results for r_P computed from Eq. (3.17) and analytic approximations for the solutions of Eq. (3.22) are presented

in Sec. 3.3.

3.3　Collective mode dispersions

The false color maps of function $\Im m\, r_P(q,\omega)$ provide a convenient visualization of the collective mode spectra. Examples of such maps computed for Bi_2Se_3 slabs are presented in the bottom row of Fig. 3.4. Their counterparts for graphene-hBN-graphene (G/hBN/G) structures are shown in the top row to facilitate the interpretation. The bright lines in Fig. 3.4 are the dispersion curves of the collective modes. The apparent widths of those lines give an idea how damped the modes are. Below we discuss these results in more detail.

3.3.1　Hyperbolic waveguide modes

Figures 3.4(a) and 3.4(d) depict the $\Im m\, r_P$ maps for, respectively, G/hBN/G and Bi_2Se_3 slabs, when they are undoped, $\mu = 0$. No Dirac plasmons exist in such systems, so that the collective modes are limited to HP^{2}s. In Fig. 3.4(a) we see a single family of such modes whereas in 3.4(d) one can actually distinguish three of them. Let us start with the former, simpler case. The key to understanding the nature of these modes is that inside the hyperbolic band $\omega_{to} < \omega < \omega_{lo}$ the z-axis momentum $k_1^z \simeq q \tan\theta$ of the modes is nearly real. Hence, the HP^{2}s form standing waves inside the slab. The integer n in Eq. (3.22) corresponds to the number of nodes of these waves, see Fig. 3.2(c). For G/hBN/G the requisite condition $\Im m\, r_P > 0$ is satisfied by all nonegative integers n due to the fact that $\Im m \tan\theta > 0$. This inequality also ensures that $\Im m\, q > 0$. An analytical approximation for the dispersion curves of an undoped slab is obtained by neglecting the fractions q/q_{top}, q/q_{bot} in Eqs. (3.20), (3.21), in

which case Eq. (3.22) yields $q(\omega)$ directly. Within this approximation, momenta q_n at given ω are equidistant:

$$q_{n+1} - q_n \simeq -\frac{2\pi}{\delta} = -\frac{\pi}{d}\frac{1}{\tan\theta(\omega)} \ . \tag{3.23}$$

The dispersion of the HP^2 waveguide modes is dominated by the factor $1/\tan\theta(\omega)$ in Eqs. (3.22), (3.23), which, if all damping is neglected, changes from zero to infinity as ω increases from ω_{to} to ω_{lo}. This is precisely what we see in Fig. 3.4(a): all the dispersion curves start at ω_{to} at $q = 0$ and increase toward ω_{lo} at large q.

Equation (3.23) is general and it applies to Bi$_2$Se$_3$ as well. The three families of collective modes seen in Fig. 3.4(d), belong to the spectral regions A, B, and C of Fig. 3.3. In region A, which is the widest of the three, we see a set of HP^2 modes very similar to those in Fig. 3.4(a). They start at $\omega_{to,1} = 64\,\mathrm{cm}^{-1}$ at $q = 0$ and monotonically increase toward $\omega_{to,2} = 135\,\mathrm{cm}^{-1}$ at large q. In region C, $154 < \omega\,(\mathrm{cm}^{-1}) < 163$, we again find a family of HP^2 modes but this time with a negative dispersion. This behavior is typical of type I HM ($\Re\mathrm{e}\,\epsilon^\perp > 0$, $\Re\mathrm{e}\,\epsilon^z < 0$). The shape of the dispersion can be understood noticing that the real part of $1/\tan\theta(\omega)$ is positive, varying from ∞ to 0 (if the phonon damping γ_j^α is neglected) while admissible n are now $n \leq 0$. [In hBN, this type I behavior is also realized [CKC$^+$14, DML$^+$15, LLK$^+$15] but the corresponding frequency range is below the axis cutoff in Fig. 3.4(a).] Lastly, in region B, $135 < \omega\,(\mathrm{cm}^{-1}) < 146$, function $\tan\theta(\omega)$ is almost purely imaginary, which implies that the collective modes do not form standing waves but are exponentially confined to the interfaces. Also, there are only two such modes, $n = 0$ and $n = 1$. In this respect these surface-bound HP^2 modes are similar to the Dirac plasmons, see Sec. 3.1 above and Sec. 3.3.2 below. However, their dispersion is completely different from

those of the plasmons, e.g., the dispersion of the upper ($n = 1$) mode has a negative slope, see Fig. 3.4(d). Similar collective excitations have been studied in literature devoted to other systems, e.g., anisotropic superconductors, [SWJ+14] which can be consulted for details and references. Due to narrowness of regions B and C, some of the described features may be difficult to see in Fig. 3.4(a) and probably challenging to observe in experiments. For this reasons, we will mostly refrain from discussing regions B and C further.

One implication of Eq. (3.23) is that the HP^2 dispersion is widely tunable: the scaling law $q_n \propto d^{-1}$ provides a practical way to engineer a desired wavelength of the waveguide modes simply by tailoring the slab thickness d, as has been previously demonstrated using hBN slabs. [DFM+14]

3.3.2 Surface plasmons

Examples of the collective mode spectra at finite doping are shown in Fig. 3.4(b, c) for G/hBN/G and 3.4(e, f) for Bi_2Se_3. The spectra are dramatically different inside and outside the hyperbolic frequency bands. A key to understanding this difference is again the value of the momentum $k_1^z \simeq q \tan \theta(\omega)$. Outside the hyperbolic bands, it is almost purely imaginary, and so the collective excitations are exponentially confined to the surfaces of the slab. These surface modes are the Dirac plasmons introduced in Sec. 3.1. Having in mind applications to near-field experiments, we are particularly interested in momenta q of the order of a few times $10^5 \, \text{cm}^{-1}$, i.e., the region nearby the dashed lines $q = 0.0025 \, \text{nm}^{-1}$ in Fig. 3.4. If ϵ_1 is real, there are at most two solutions of Eq. (3.22), one for $n = 0$ and the other for $n = 1$. However, the distinct $n = 1$ dispersion curves are visible only in Fig. 3.4(b, c) for G/hBN/G and none of

them is close enough to the range of q we are interested in. Therefore, we focus on the $n = 0$ branch.

The shape of the plasmon dispersion curves in TI slabs and double-layer graphene systems was a subject of many previous theoretical studies [HDS09, PAPM12, SGSB13, Sta14, LDC$^+$14] whose basic conclusions are reproduced by the following analysis. To the right of the dashed lines in Fig. 3.4(b, e) and for $d \sim 100\,\mathrm{nm}$, the dimensionless product $2k_1^z d = q\delta$ is typically large by absolute value and almost purely imaginary. This implies that the plasmons of the two interfaces are decoupled. Taking into account that $\epsilon_0 < \epsilon_s$ and $q_{\mathrm{top}} = q_{\mathrm{bot}}$ in Fig. 3.4, one can show that the dispersion of the $n = 0$ mode is controlled by the properties of the top interface. In the first approximation this dispersion can be obtained setting $\phi_{\mathrm{top}} \to -i\infty$, which yields

$$q_0 \approx \frac{\epsilon_0 + \epsilon_1}{2}\, q_{\mathrm{top}}\,, \quad q_0 \gg |\delta|^{-1}. \tag{3.24}$$

For $\mu = 0$, momentum $q_{\mathrm{top}} = q_{\mathrm{top}}(q_0, \omega)$ is imaginary, cf. Eqs. (3.13) and (3.19). Hence, for real ϵ_1, Eq. (3.24) has no real solutions: as already mentioned, undoped SSs do not support plasmons. Indeed, Figs. 3.4(a) and (d) contain no bright lines outside the hyperbolic bands. On the other hand, if $\mu \neq 0$, we can use Eq. (3.11) to transform Eq. (3.24) to Eq. (3.4), which predicts a parabolic dispersion curve $\omega \propto \sqrt{q}$ if ϵ_1 is constant. Such parabolas are seen in the upper halves of Figs. 3.4(b, c) and (e, f) although they appear rectilinear because of the restricted range of q.

As smaller momenta Eq. (3.24) no longer holds. The correct approximation for the $n = 0$ mode is obtained by setting the left-hand side of Eq. (3.22) to zero. This

yields $\phi_{\text{top}} = -\phi_{\text{bot}}$ and

$$q_0 \simeq \frac{\epsilon_0 + \epsilon_s}{2} \frac{1}{q_{\text{top}}^{-1} + q_{\text{bot}}^{-1}} \simeq \frac{2}{N} \frac{\epsilon_0 + \epsilon_s}{e^2 |\mu|} (\hbar\omega)^2 . \qquad (3.25)$$

Thus, both the low-q and high-q parts of the $n = 0$ dispersion curve are parabolic but with different curvatures. The crossover between these two parabolas occurs via a rapid increase of $\epsilon^{\perp}(\omega)$, and so, $\epsilon_1(\omega)$ at frequencies immediately above the hyperbolic bands. It takes place at $\omega > 1614\,\text{cm}^{-1}$ for G/hBN/G and $\omega > 163\,\text{cm}^{-1}$ for Bi$_2$Se$_3$, which generates the inflection points seen on the curves in, respectively, Fig. 3.4(b, c) and (e, f).

As indicated schematically in Fig. 3.2(a), at very large q the plasmon dispersion should have another inflection point. Using the more accurate Eq. (3.10) instead of Eq. (3.11), we find the following analytical result for the frequency of the $n = 0$ mode as a function of q:

$$\omega(q) \simeq v \frac{q + q_*}{\sqrt{1 + (2q_*/q)}} , \qquad q_* = \frac{2e^2}{\hbar v} \frac{N k_F}{\epsilon_0 + \epsilon_1} . \qquad (3.26)$$

This equation predicts a crossover from the parabolic to the linear dispersion $\omega \simeq vq$ above $q = q_*$. However, this occurs far outside the plot range of Fig. 3.4.

Returning to Eq. (3.25), we notice that it does not contain the bulk permittivities. Hence, it should continue to hold for a range of ω inside the hyperbolic bands. A physical picture of this mode ["$0(s)$" in Fig. 3.2(c)] is in-phase oscillations of the charges of both Dirac fermion layers, i.e., the system behaving as a single 2D layer with the combined oscillator strength. As ω decreases further into the hyperbolic bands, the length scale $|\delta|$ increases. The strength of the inequality $q_0|\delta| \ll 1$ and so

the accuracy of Eq. (3.25) becomes progressively lower [in fact, Eq. (3.27) below gives a better approximation]. At $\omega = \omega_{to}$ for G/hBN/G and similarly, at $\omega = \omega_{to,1}^{\perp}$ for Bi_2Se_3, this inequality is violated completely, which is consistent with the termination of these branches at $q = 0$ in Figs. 3.4(b) and (e). Similar analysis can be applied to Figs. 3.4(c) and (f) where d is twice smaller than in, respectively, Figs. 3.4(b) and (e). Because of that, the plasmon dispersion in the region $q|\delta| < 1$ is shifted to smaller q. The dispersions in the large-q regions are virtually unaffected since the stronger surface confinement of the plasmons makes them insensitive to d.

One qualitative difference between G/hBN/G and Bi_2Se_3 is the richer phonon spectrum of the latter. This leads to the avoided crossings of the plasmon branch with the dispersion lines of the HP^2 modes in regions B and C of Bi_2Se_3, cf. Fig. 3.4(b, c) and 3.4(e, f). The small shifts caused by those crossings are somewhat masked by the considerable linewidth of the $n = 0$ line due to relatively stronger phonon damping. In turn, higher electronic damping rate $\gamma_e \sim \omega_{to,1}^{\perp}$ due to disorder scattering in Bi_2Se_3 effectively eliminates the plasmon excitations in the lower spectral region $\omega < \omega_{to,1}^{\perp}$, see Fig. 3.4(e, f). Therefore, we do not discuss it here.

3.3.3 Hybrid modes

From now on we turn to the subject of our primary interest, the hyperbolic collective modes of a doped TI. In this short section we address their dispersion law. Comparing Fig. 3.4(d) for $\mu = 0$ with Fig. 3.4(e, f) for $\mu > 0$, we observe significant shifts in the dispersion of the $n = 0$ mode in the upper half of the hyperbolic band $\omega_{to,1}^{\perp} < \omega < \omega_{to,1}^{z}$ of Bi_2Se_3. Similar shifts are seen in hBN near ω_{lo}, cf. Fig. 3.4(a) with Fig. 3.4(b, c). These shifts result from hybridization of HP^2 and Dirac plasmons

into combined HP^3 waveguide modes. In general, calculation of these shifts requires solving Eq. (3.22) numerically. However, near the bottom of the hyperbolic band where these shifts become small, they can be also found analytically. Thus, Eq. (3.25) gets replaced by

$$q_0 \simeq \frac{\epsilon_0 + \epsilon_s}{\epsilon^\perp d + 2q_{\text{top}}^{-1} + 2q_{\text{bot}}^{-1}} , \quad |\epsilon_1| \gg \epsilon_0, \epsilon_s , \tag{3.27}$$

which shows explicitly that q_0 goes to zero as ω approaches $\omega_{to,1}^\perp$ where $\epsilon^\perp$ sharply increases.

Unlike in Fig. 3.4(a, d), in 3.4(b, c, e, f) the higher-order $n > 1$ modes are more difficult to see because of their lower relative intensity compared to those of the plasmon $n = 0$ (and $n = 1$) modes. Nevertheless, these modes remain well defined (underdamped). Near the bottoms of the respective hyperbolic bands their momenta q_n still form an equidistant sequence except with a spacing

$$q_{n+1} - q_n \simeq \frac{2\pi}{l - \delta} , \tag{3.28}$$

which is modified compared to Eq. (3.23). This result can be obtained from Eq. (3.22) by approximating the finite differences such as $\phi_{\text{top}}(q_{n+1}) - \phi_{\text{top}}(q_n)$ by means of the derivative. Parameter l is defined by

$$l = -2 \frac{\partial \phi_{\text{top}}}{\partial q} - 2 \frac{\partial \phi_{\text{bot}}}{\partial q} . \tag{3.29}$$

The physical meaning of this quantity is clarified in the next Section.
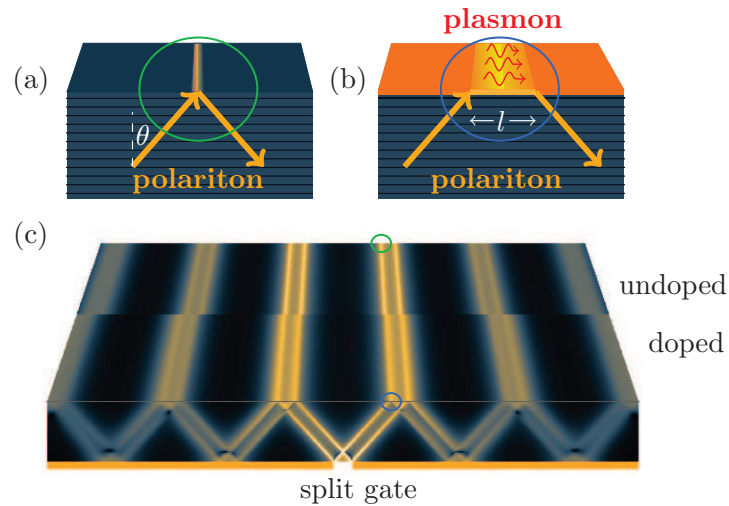
Figure 3.5: (Color online) Polaritonic GH effect in TI slabs. (a) Schematics of the HP^2 ray reflection in the absence of the SS. (b) The same with the SS. The wavy lines symbolize virtual Dirac plasmons. The GH shift l is indicated. (c) The electric field distribution inside and/or at the upper surfaces of two slabs with equal $\delta = -2.2d$ but different doping. The lower ("doped") and the upper ("undoped") parts of the image are computed for $\lambda_p = a$ and 0, respectively. The split gate — a pair of metallic half-planes separated by a distance $2a$ — launches highly directional HP^2 rays that bounce inside the slabs creating periodic "hot stripes" at their upper surfaces. The period is larger in the "doped" slab. The two small circles, one in the undoped and one in doped part, are the representative locations of the HP^2 reflections. Their enlarged views are shown in, respectively, (a) and (b).

3.4 Goos-Hänchen effect

In this Section we consider the problem of the plasmon-polariton mixing from the point of view of real-space trajectories of the HP^2 excitations. The question we consider is how polariton wavepackets propagate inside the slab and, in particular, how they reflect off its interfaces. As mentioned in Sec. 3.1, for a given ω, the angle θ between the z-axis and the group velocity $\mathbf{v}$ vector of HP^{2}s is nearly independent of q. Therefore, monochromatic HP^2 wavepackets propagate as highly directional rays. Naively, one would then expect that the polariton rays should zigzag inside the slab returning to each interface periodically with the repeat distance of $2d\,|\tan\theta| = |\delta|$. Although such geometrical optics picture is adequate for insulating hyperbolic materials, [SGRBF15] it is not quite correct for TI with gapless doped SS. The geometrical optics neglects a lateral shift or displacement of the rays after each reflection [compare Figs. 3.5(a) and (b)], which is analogous to the GH effect of light. The GH effect was first discussed in the context of the total internal reflection of light. As explained below, it can be understood from two complementary points of view. In the wave picture, it originates from the momentum dependence of the reflection phase shift. In the particle picture, the GH effect is due to the quasi-classical tunneling (excitation of evanescent waves) along the interface. To define such a displacement one usually considers a wavepacket with a smooth envelope (for example, a Gaussian), in which case the displacement is the shift in the position of its maximum.

While the GH effect [GH47] was discovered measuring the reflection of light off an air-metal interface, the displacement $\mathbf{l}$ of the reflected ray is a general wave phenomenon [BA13] that arises due to the dependence of the reflection phase shift ϕ on the lateral momentum $\mathbf{q} = (k^x, k^y)$. For example, the GH effect should also occur

for surface plasmons. [HLMB11] The expression for $\mathbf{l}$ has the form [Art48]

$$\mathbf{l} = -\Re e \frac{\partial \phi}{\partial \mathbf{q}}. \tag{3.30}$$

It seems to be another general rule that the momentum dependence of ϕ is significant only if the interface supports electromagnetic modes with either a large propagation length or a long decay length if such modes are evanescent. In the original photonic GH effect this is the case under the conditions of the total internal reflection. The magnitude $|\mathbf{l}|$ of the GH displacement can be interpreted as the decay length of the evanescent transmitted wave. Alternatively, a large GH shift can occur if the interface supports surface plasmons or polaritons. [TO63, TB71, Chu86] Experimental demonstration of the GH effect enhanced by surface plasmons of the air-metal interface has been reported. [YHL+04]

Comparing Eqs. (3.29) and (3.30), we recognize the length scale l in the former as the sum of the GH shifts due to the top and the bottom interfaces. Therefore, we conclude that the Dirac plasmons must act as the transient interface modes for the HP^2 rays bouncing inside the TI slab. Using Eqs. (3.20), (3.30), and taking into account that $\Re e\,\epsilon_1 \ll \Im m\,\epsilon_1$, we find the GH shift at the top interface to be

$$l_{\text{top}} = \frac{4}{q_{\text{top}}} \frac{\Im m\,\epsilon_1}{\left(\epsilon_0 - \frac{2q}{q_{\text{top}}}\right)^2 + |\epsilon_1|^2}. \tag{3.31}$$

A few comments on this result can be made. First, the GH shift is positive in our case, which means the displacement is in the same direction as the in-plane group velocity of the ray. Second, l_{top} depends on the permittivity of the environment. For example, at fixed q, it vanishes if ϵ_0 is very large. Conversely, for fixed ϵ_0, the GH

shift reaches its maximum

$$l_{\max} = \frac{2}{\pi} \frac{\lambda_p \epsilon_0 \Im m \, \epsilon_1}{(\Re e \, \epsilon_1)^2 + (\Im m \, \epsilon_1)^2} \,, \quad \lambda_p \equiv \frac{2\pi}{\epsilon_0 q_{\mathrm{top}}} \,, \tag{3.32}$$

at $q = \pi/\lambda_p$. Finally, $l_{\max}$ depends linearly on the characteristic size λ_p of the Dirac plasmon wavelength and inversely on the absolute value $|\epsilon_1| \approx \Im m \, \epsilon_1$ of the effective permittivity of the hyperbolic medium.

In Fig. 3.6, we show $l_{\max}$ for Bi_2Se_3 and G/hBN/G systems as a function of ω spanning their respective hyperbolic bands. The relative shift, $l_{\max}/\lambda_p$, is greater in G/hBN/G because $|\epsilon_1|$ is smaller. Yet the absolute $l_{\max}$ at the same $\mu = 0.3\,\mathrm{eV}$ is greater in Bi_2Se_3 (where it is $\sim 200\,\mathrm{nm}$) because it is hyperbolic at lower frequencies and λ_p is larger at smaller ω.

One possible setup for experimental detection of the GH effect in TI is shown in Fig. 3.5(c). It differs from Fig. 3.1(b) in the addition of a split gate between the TI slab and the substrate. If this gate is made of a good conductor with large permittivity, it would suppress the GH shift at the bottom surface. However, it would serve another useful purpose. Previously, it has been demonstrated [DMA+15] that in the presence of an external oscillating field, thin metallic disks or stripes can launch HP^2 in hBN. The split gate is to perform the same function here. The HP^2s are preferentially emitted from the regions of highly concentrated field near the sharp metallic edges. We expect the rays to zigzag away from their launching points returning to the top surface with the period $l - \delta$, which is the sum of $-\delta \approx |\delta|$ due to the roundtrip inside the slab and $l = l_{\mathrm{top}}$ due to the GH shift at the top surface. Since l depends q_{top}, which is controlled by doping, the GH effect can be detected by measuring the positions of the electric field maxima ["hot stripes" in Fig. 3.5(c)] as a function of
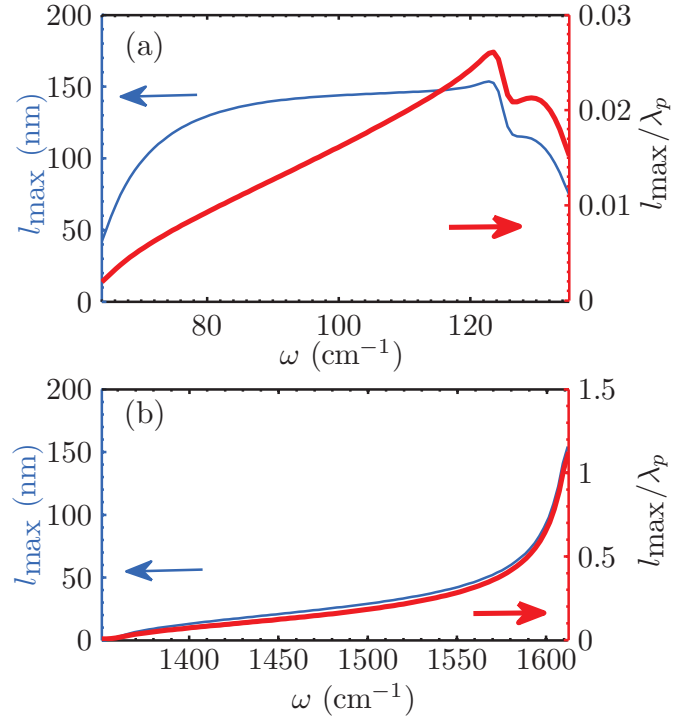
Figure 3.6: (Color online) Maximum GH shift $l_{\max}$ (in absolute units and as a fraction of λ_p) for (a) TI slab and (b) G/hBN/G structure with the same chemical potential $\mu = 0.3\,\text{eV}$.

μ in the experiment. Although l is quite small, the shifts accumulate after multiple reflections, which can facilitate their detection, as in the original work of Goos and Hänchen. [GH47]

To model the response of the system shown in Fig. 3.5(c) quantitatively we proceed as follows. We approximate the half-planes of the split gate by perfect conductors in the $z = 0$ plane with the edges at $x = \pm a$. Let $V(x, 0)$ be the scalar potential at $z = 0$ due to the external uniform field and all the charges induced on the gate. (Here and below the common factor $e^{-i\omega t}$ is omitted.) Let $\widetilde{V}(k^x)$ be the Fourier transform of $V(x, 0)$. Using the notations for the reflection coefficients introduced in Sec. 3.2, we express the potential $V(x, z)$ inside the slab $0 \leq z \leq d$ by the integral

$$V(x, z) = \int \frac{dk^x}{2\pi} \widetilde{V}(k^x) t(k^x, z) e^{ik^x x}, \tag{3.33}$$

$$t(k^x, z) = \frac{e^{i|k^x|z \tan\theta} - r_{10}(k^x) e^{i|k^x| \tan\theta (2d-z)}}{1 - r_{10}(k^x) r_{12}(k^x) e^{i|k^x|\delta}}. \tag{3.34}$$

For a consistency check we can consider the large-x behavior of this inverse Fourier transform, which should be dictated by the poles of the integrand. These poles can be recognized as the HP^3 momenta q_n [Eq. (3.22)]. Since q_n form the equidistant sequence [Eq. (3.28)], their superposition should indeed create beats of period $l - \delta$, in agreement with our ray trajectories picture, Fig. 3.5(b).

Explicit calculation of $V(x, 0)$ requires a self-consistent solution of the Maxwell equations for our complicated multilayer system, which is computationally intensive. Fortunately, very similar results for $V(x, z)$ are obtained with little effort by approximating the true $V(x, 0)$ with the "bare" potential that would exist in the TI is removed, that is, if $d = \lambda_p = 0$. At distances less than c/ω from the gap in the gate,

this bare potential has the simple analytical form,

$$V(x,0) = \frac{V_0}{2} \times \begin{cases} +1, & x \leq -a, \\ -\frac{2}{\pi} \arcsin(x/a), & |x| < a, \\ -1, & x \geq a, \end{cases} \qquad (3.35)$$

familiar from classical electrostatics. Its Fourier transform is given by

$$\widetilde{V}(k^x) = \frac{iV_0}{k^x} J_0(k^x a), \qquad (3.36)$$

where $J_0(x)$ is the Bessel function of the first kind and V_0 is potential difference between the two parts of the gate. The tangential electric field corresponding to this potential,

$$E_x = \frac{V_0}{\pi\sqrt{a^2 - x^2}}, \qquad (3.37)$$

exhibits an inverse square-root divergence at the edges, which enables the localized HP^2 emission.

Carrying out the quadrature in Eq. (3.33) numerically, we have calculated the components and also the amplitude of the electric field $E = \sqrt{E_x^2 + E_z^2}$ over an interval of x a few $|\delta|$ in length and z varying from 0 to d. Our results for $E = E(x, z)$ for two doping levels, corresponding to $\lambda_p = 0$ (undoped SS) and $\lambda_p = a$ (doped SS) are illustrated by the false color plots in Fig. 3.5(c). These plots are superimposed on perspective projections of the two slabs (doped and undoped), which are placed next to each other for easy comparison. The remaining parameters of the calculations are $\delta = -2.2d$ and $a = 0.1d$. We see that a finite shift of the "hot stripes" at the top surface $z = d$ exists in the doped case. This seems to vindicate our intuition

but actually the situation is a bit more subtle. The problem is that the momentum distribution of our source [Eq. (3.36)] is very different from what we assumed it to be in the beginning of our discussion of the GH effect. This distribution is not narrow and not centered at some finite k^x. Instead, it has positive and negative k^x harmonics of equal strength and a long power-law tail at $|k^x| \gg 1/a$. The reason why the GH shift persists in our case is the spatial separation of the k^x harmonics: due to the directionality of the HP^2 propagation, the stripes to the left (right) of the launching points are created predominantly by negative (positive) k_x. Since $\mathbf{l}$ has the same direction as $\mathbf{q} = (k^x, 0)$, the stripes shift away from the origin on both sides of the y-axis. A formal derivation of this result can be done by splitting the integral in Eq. (3.33) into the $k_x > 0$ and the $k_x < 0$ parts and identifying the relevant poles $k_x = q_n$ using contour integration methods.

From numerical experiments with different a, we found that the largest shift of the stripes is obtained for $a \sim \lambda_p$. This can be explained by arguing that the shift is maximized when the characteristic $k^x \sim \pi/a$ contributing to the integral in Eq. (3.33) is close to the momentum π/λ_p at which $l = l_{\max}$ in Eq. (3.31).

Experimental detection of the "hot stripes" and their doping-dependent GH shift is possible via the s-SNOM imaging. This technique involves measuring the light scattered by the tip of an atomic force microscope brought to the sample and scanned along its surface. [KH04, ABJR12] Using clever signal processing methods, it is possible to isolate the genuine near-field component of this scattered light, which originates from conversion of evanescent electromagnetic waves emanating from the sample into free-space photons. In the proposed experiment, the evanescent waves are due to the HP^2 modes launched by the split gate. The spatial resolution of the s-SNOM

imaging is set by the tip curvature radius R. For typical $R = 20$–40 nm, it is barely sufficient to observe the predicted GH shifts in hBN/G, Fig. 3.6(b). Nevertheless, detecting the cumulative shift after several stripe periods should be feasible. The prior success of s-SNOM imaging experiments of surface plasmons and polaritons in graphene and hBN structures [FAB$^+$11, CBAG$^+$12, DFM$^+$14, DMA$^+$15, LLK$^+$15, DML$^+$15, SBB$^+$15, NWW$^+$15] gives us a firm confidence in this approach. Note that if a doped graphene layer only partially covers the top surface of hBN, one literally gets the situation depicted in Fig. 3.5(c), where the doped and undoped regions are positioned side by side.

In the case of Bi$_2$Se$_3$ where the GH shift ~ 200 nm [Fig. 3.6(a)] is much larger, the spatial resolution of the s-SNOM is even less of an issue. The main obstacle is the scant availability of suitable THz sources. We are optimistic that in a near future this problem can be overcome as well.

3.5 Summary and outlook

Recent experiments [DOL$^+$13, ADDG$^+$15] have shown that coupling between Dirac plasmons and bulk phonons of bismuth-based TIs should be strong. In this paper we have studied this interaction taking into account the anisotropic phonon spectrum of such TIs. We have predicted that a TI slab can act as a tunable waveguide for phonon polaritons, with the doping of the surface states being the tuning parameter. In additional to the change in dispersion, the phonon-plasmon coupling can cause measurable real-space shifts of the polariton rays. Similar phenomena have been recently studied in artificial structures made by stacking graphene layers on top of hBN. The present work indicates that the TIs are a promising alternative platform for

realizing highly tunable, strongly confined, low-loss electromagnetic modes in a *natural* material. Additionally, while hBN/G waveguides operate in mid-infrared frequencies, Bi_2Se_3 and similar compounds extend the same functionality to the technologically important THz domain.

We envision several directions for further work in this field. One is to attempt a multi-source coherent control of polariton emission and propagation using ultrafast laser pulses. A variety of such techniques has been developed [FSW+07] in the context of THz polaritonics of $LiNbO_3$ and $LiTiO_3$. (Incidentally, a theoretical proposal [JKHF+13] of integrating graphene into such materials would lead to polariton waveguides similar in functionality and perhaps also tunability to those studied in the present work.) Another intriguing direction is to explore oscillating spin currents which were predicted to accompany charge density currents produced by Dirac plasmons. [RCQZ10] It may be also interesting to study the effect of optical hyperbolicity [EVT+14] on the high-energy bulk plasmons of the TIs. [CKH+13, OSA+14] Finally, it may be worthwhile to investigate new applications that can be enabled by tunable hyperbolic polaritons. Harnessing such types of modes for hyperlensing [JAN06, SE06, LLX+07] or focusing [DMA+15, LLK+15] has been widely discussed. The present work shows that the GH effect and its dependence on doping and dielectric environment of the TI can be another avenue for applications, for example, THz chemical sensing or characterization of spatially inhomogeneous TI samples. We hope our work can stimulate these and other future studies.

3.6 Near-field spectra

A fully realistic modeling of the s-SNOM imaging experiments proposed in Sec. 3.4 is an unwieldy task requiring a repeated solution of the Maxwell equations for a system with complicated material properties, a hierarchy of widely different length scales, and no special symmetries. In this Appendix we present some results of less ambitious calculations that simulate a simpler structure depicted in Fig. 3.1(b). Although no split gate is present in this structure, the measured signal is still expected to reveal characteristics of the collective modes. In this case these modes are excited by the sharp tip itself. Hence, the tip plays the role of both the launcher and the detector of the HP^3 modes. Unfortunately, this implies that only the local response can be measured, which is a superposition of responses due to a distribution of momenta up to $q_t \sim 1/R$ rather than one specific q.

We assume that the TI slab and the substrate are infinite and uniform in x and y coordinates, so that the imaging capability of the s-SNOM is irrelevant. Instead, the quantity of interest is the frequency dependence of the measured near-field signal $s(\omega)$. A few more explanations about our calculational scheme are in order. We model the tip as a metallic spheroid with the curvature radius $R = 40\,\text{nm}$ and total length $720\,\text{nm}$. We use the quasistatic approximation but include the radiative corrections included perturbatively. This model [ZAF+12, JZCN+] has been successful for simulating many recent s-SNOM experiments, and should be especially suitable in the THz domain where no antenna resonances or other strong retardation effects [MKG+14] should appear. Our calculations incorporate the so-called far-field factors, [ZAF+12, JZCN+, MKG+14] which are expressed in terms of $r_P(q, \omega)$ at $q \sim \omega/c$. This factors account for the fact that the incident wave is originally created
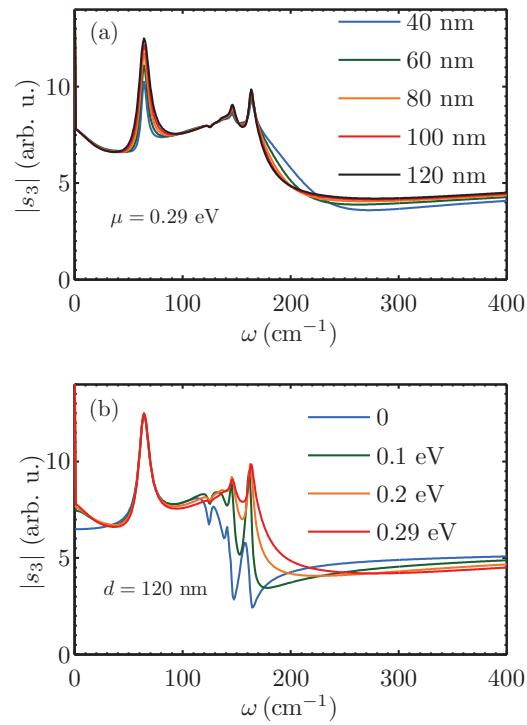
Figure 3.7: (Color online) Simulation of the s-SNOM signal s_3 for Bi_2Se_3 slabs on a substrate with $\epsilon_s = 10$. (a) Fixed $\mu = 0.29\,\text{eV}$ and different d. (b) Fixed $d = 120\,\text{nm}$ and different μ.

by a far-field source and the scattered wave is ultimately measured by a far-field detector. Finally, what we compute is not the full scattering amplitude s but its third harmonic s_3, which is what experimentalists typically report. The idea is that in the experiment the tip is made to oscillate at some low frequency Ω, so that s is periodic with this fundamental tapping frequency. The third Fourier harmonic of s, which is s_3, gives a good representation of the genuine near-field signal.

Naively, one can think of $s_3(\omega)$ as a weighted average of the surface reflectivity $r_P(q, \omega)$ over q. The weighting function has a broad maximum near $q = q_t$, which in this case is equal to $q_t = 0.025\,\mathrm{nm}^{-1}$ [the dashed lines in Fig. 3.4]. The presence of strong maxima of $\Im m\, r_P$ due to collective modes with momenta $q \lesssim q_t$ tends to enhance $s_3(\omega)$. In a more rigorous picture, [JZCN$^+$] the maxima of $s_3(\omega)$ correspond not to the resonances of the sample alone but to those of the coupled tip-sample system. The coupling can decrease the resonance frequencies by as much as [ZAF$^+$12, JZCN$^+$, MKG$^+$14] 10–20 cm^{-1} compared to those seen in $\Im m\, r_P$ maps.

Our results for Bi$_2$Se$_3$ slabs of various thickness d and chemical potential μ are shown in Fig. 3.7. Pairs of distinct peaks as well as smaller additional features are readily seen. In each trace, the stronger and sharper peak is located close to $\omega_{to,1}^{\perp} = 64\,\mathrm{cm}^{-1}$. The height of this peak decreases as d decreases [Fig. 3.7(a)]. However, its position is independent of d [Fig. 3.7(a)] or μ [Fig. 3.7(b)], which suggests that it is not related to the dispersive HP^3 modes. Indeed, we have verified that this prominent peak is almost entirely due to the far-field factor $|1 + r_P|^2$, which has a narrow maximum at $\omega_{to,1}^{\perp}$ where $r_P \approx 1$.

Each of the doped samples also produces smaller peaks in $s_3(\omega)$, of which the most prominent ones are those located near $\omega = 146\,\mathrm{cm}^{-1}$ and $\omega = 163\,\mathrm{cm}^{-1}$, the

upper boundaries of regions B and C of Fig. 3.3. The position and especially the strength of the peaks is μ-dependent. As μ increases, the peaks grow in height and gradually shift to higher frequencies, see Fig. 3.7(b). These peaks are due to the surface modes: the $n = 1$ mode of region B and the $n = 0$ mode just above region C, see Fig. 3.4(d, e). The increase of the peak heights with μ can be qualitatively explained by the increase of the absolute value of r_P. The shift in position is unfortunately more difficult to interpret without a better understanding of the effective weighting function that relates $\Im m\, r_P(q, \omega)$ to $s_3(\omega)$.

While $\mu > 0$ traces are due to combined action of plasmons and phonon-polaritons, the $\mu = 0$ one is expected to reveal the phonon-polariton response. Interestingly, that trace exhibits a sharp dip at $\omega = 163\,\mathrm{cm}^{-1}$, see Fig. 3.7(b). We have checked that this dip is not caused by the far-field factor. However, its relation to the HP^2 modes of Fig. 3.4(d) is not obvious to us.

The thickness dependence of s_3 is illustrated in Fig. 3.7(a). As one can see, the near-field peak at $\omega = 163\,\mathrm{cm}^{-1}$ has a broad high-frequency side, which systematically expands as d decreases. This trend reflects the blue shift of the $n = 0$ mode dispersion in thinner slabs, compare Fig. 3.4(e) and (f).

Overall, our simulations predict that the near-field response of $\mathrm{Bi}_2\mathrm{Se}_3$ slabs should exhibit systematic spectral changes with doping and thickness that are measurable by the s-SNOM. Such experiments may provide insights into properties of tunable HP^3 modes of these novel systems.

3.7   Acknowledgement

This chapter, in full, is a reprint of the material as it appears in Physical Review B: Wu, Jhih-Sheng; Basov, Dimitri; Fogler, Michael,"Topological insulators are tunable waveguides for hyperbolic polaritons", Phys. Rev. B 92, 205430 (2015). The dissertation author was the primary investigator and author of this paper.

References

[ABJR12]   Joanna M. Atkin, Samuel Berweger, Andrew C. Jones, and Markus B. Raschke. Nano-optical imaging and spectroscopy of order, phases, and domains in complex solids. *Adv. Phys.*, 61(6):745–842, 2012.

[ADDG$^+$15]   Marta Autore, Fausto D'Apuzzo, Alessandra Di Gaspare, Valeria Giliberti, Odeta Limaj, Pascale Roy, Matthew Brahlek, Nikesh Koirala, Seongshik Oh, Francisco Javier García de Abajo, and S. Lupi. Plasmon-Phonon Interactions in Topological Insulator Microrings. *Adv. Opt. Mat.*, 3:1257–1263, 2015.

[AE06]   I. L. Aleiner and K. B. Efetov. Effect of Disorder on Transport in Graphene. *Phys. Rev. Lett.*, 97:236801, Dec 2006.

[AED$^+$15]   Marta Autore, Hans Engelkamp, Fausto DApuzzo, Alessandra Di Gaspare, Paola Di Pietro, Irene Lo Vecchio, Matthew Brahlek, Nikesh Koirala, Seongshik Oh, and Stefano Lupi. Observation of magnetoplasmons in bi2se3 topological insulator. *ACS Photonics*, 2(9):1231–1235, 2015.

[Art48]   Kurt Artmann. Berechnung der Seitenversetzung des totalreflektierten Strahles. *Ann. Phys.*, 437(1-2):87–102, 1948.

[ATU$^+$12]   Ana Akrap, Michaël Tran, Alberto Ubaldini, Jérémie Teyssier, Enrico Giannini, Dirk van der Marel, Philippe Lerch, and Christopher C. Homes. Optical properties of Bi_2Te_2Se at ambient and high pressures. *Phys. Rev. B*, 86:235207, 2012.

[BA13]   K Y Bliokh and A Aiello. Goos-anchen and Imbert-Fedorov beam shifts: an overview. *J. Opt.*, 15(1):014001, 2013.

[BBHW10]   J Berezovsky, M F Borunda, E J Heller, and R M Westervelt. Imaging coherent transport in graphene. Part I: mapping universal conductance fluctuations. *Nanotechnology*, 21(27):274013, July 2010.

[Ber66]   M. V. Berry. Uniform approximation for potential scattering involving a rainbow. *Proc. Phys. Soc.*, 89(3):479, 1966.

[BFL+14a]   D. N. Basov, M. M. Fogler, A. Lanzara, Feng Wang, and Yuanbo Zhang. Colloquium: Graphene spectroscopy. *Rev. Mod. Phys.*, 86:959–994, 2014.

[BFL+14b]   D. N. Basov, M. M. Fogler, A. Lanzara, Feng Wang, and Yuanbo Zhang. Colloquium: Graphene spectroscopy. *Rev. Mod. Phys.*, 86:959–994, Jul 2014.

[BJS+13]   Victor W. Brar, Min Seok Jang, Michelle Sherrott, Josue J. Lopez, and Harry A. Atwater. Highly Confined Tunable Mid-Infrared Plasmonics in Graphene Nanoresonators. *Nano Lett.*, 13(6):2541–2547, 2013.

[BTB09]   J. H. Bardarson, M. Titov, and P. W. Brouwer. Electrostatic Confinement of Electrons in an Integrable Graphene Quantum Dot. *Phys. Rev. Lett.*, 102:226803, Jun 2009.

[CBAG+12]   Jianing Chen, Michela Badioli, Pablo Alonso-González, Sukosin Thongrattanasiri, Florian Huth, Johann Osmond, Marko Spasenović, Alba Centeno, Amaia Pesquera, Philippe Godignon, Amaia Zurutuza Elorza, Nicolas Camara, F Javier García de Abajo, Rainer Hillenbrand, and Frank H L Koppens. Optical nano-imaging of gate-tunable graphene plasmons. *Nature*, 487(7405):77–81, 2012.

[CF06]   Vadim V. Cheianov and Vladimir I. Fal'ko. Selective transmission of Dirac electrons and ballistic magnetoresistance of n-p junctions in graphene. *Phys. Rev. B*, 74:041403, Jul 2006.

[CFA07]   V. V. Cheianov, V. Fal'ko, and B. L. Altshuler. The Focusing of Electron Flow and a Veselago Lens in Graphene p-n Junctions. *Science*, 315(5816):1252–1255, 2007.

[CFU56]   C. Chester, B. Friedman, and F. Ursell. An extension of the method of steepest descents. *Proc. Cambridge Phil. Soc.*, 53:599–611, 1956.

[Chu86]   S. L. Chuang. Lateral shift of an optical beam due to leaky surface-plasmon excitations. *J. Opt. Soc. Am. A*, 3(5):593–599, 1986.

[Chý76]   P. Chýlek. Partial-wave resonances and the ripple structure in the Mie normalized extinction cross section. *J. Opt. Soc. Am.*, 66(3):285, March 1976.

[CKC+14]   Joshua D. Caldwell, Andrey V. Kretinin, Yiguo Chen, Vincenzo Giannini, Michael M. Fogler, Yan Francescato, Chase T. Ellis, Joseph G. Tischler, Colin R. Woods, Alexander J. Giles, Minghui Hong, Kenji Watanabe, Takashi Taniguchi, Stefan A. Maier, and Kostya S. Novoselov. Sub-diffractional volume-confined polaritons in the natural hyperbolic material hexagonal boron nitride. *Nat. Comm.*, 5:5221, 2014.

[CKH+13]   Judy J. Cha, Kristie J. Koski, Kevin C. Y. Huang, Ken Xingze Wang, Weidong Luo, Desheng Kong, Zongfu Yu, Shanhui Fan, Mark L. Brongersma, and Yi Cui. Two-Dimensional Chalcogenide Nanoplates as Tunable Metamaterials via Chemical Intercalation. *Nano Lett.*, 13(12):5913–5918, Dec 2013.

[CNGP+09] A. H. Castro Neto, F. Guinea, N. M. R. Peres, K. S. Novoselov, and A. K. Geim. The electronic properties of graphene. *Rev. Mod. Phys.*, 81:109–162, Jan 2009.

[CPP07]   József Cserti, András Pályi, and Csaba Péterfalvi. Caustics due to a Negative Refractive Index in Circular Graphene *p-n* Junctions. *Phys. Rev. Lett.*, 99:246801, Dec 2007.

[CPR+14]   B. C. Chapler, K. W. Post, A. R. Richardella, J. S. Lee, J. Tao, N. Samarth, and D. N. Basov. Infrared electrodynamics and ferromagnetism in the topological semiconductors Bi_2Te_3 and Mn-doped Bi_2Te_3. *Phys. Rev. B*, 89:235308, 2014.

[CR11]   Wei Cheng and Shang-Fen Ren. Phonons of single quintuple Bi_2Te_3 and Bi_2Se_3 films and bulk materials. *Phys. Rev. B*, 83:094301, 2011.

[DFM+14]   S. Dai, Z. Fei, Q. Ma, A. S. Rodin, M. Wagner, A. S. McLeod, M. K. Liu, W. Gannett, W. Regan, K. Watanabe, T. Taniguchi, M. Thiemens, G. Dominguez, A. H. Castro Neto, A. Zettl, F. Keilmann, P. Jarillo-Herrero, M. M. Fogler, and D. N. Basov. Tunable Phonon Polaritons in Atomically Thin van der Waals Crystals of Boron Nitride. *Science*, 343(6175):1125–1129, 2014.

[DMA+15]   S. Dai, Q. Ma, T. Andersen, A. S. Mcleod, Z. Fei, M. K. Liu, M. Wagner, K. Watanabe, T. Taniguchi, M. Thiemens, F. Keilmann, P. Jarillo-Herrero, M. M. Fogler, and D. N. Basov. Subdiffractional focusing and guiding of polaritonic rays in a natural hyperbolic material. *Nat. Commun.*, 6:6963, 2015.

[DML+15]   S. Dai, Q. Ma, M. K. Liu, T. Andersen, Z. Fei, M. D. Goldflam, M. Wagner, K. Watanabe, T. Taniguchi, M. Thiemens, F. Keilmann, G. C. A. M. Janssen, S.-E. Zhu, P. Jarillo-Herrero, M. M. Fogler, and D. N. Basov. Graphene on hexagonal boron nitride as a tunable hyperbolic metamaterial. *Nat. Nano*, 10:682–686, 2015.

[DOL+13]   P Di Pietro, M Ortolani, O Limaj, A Di Gaspare, V Giliberti, F Giorgianni, M Brahlek, N Bansal, N Koirala, S Oh, P Calvani, and S Lupi. Observation of Dirac plasmons in a topological insulator. *Nat. Nano.*, 8(8):556–60, 2013.

[DPVN+12] P. Di Pietro, F. M. Vitucci, D. Nicoletti, L. Baldassarre, P. Calvani, R. Cava, Y. S. Hor, U. Schade, and S. Lupi. Optical conductivity of bismuth-based topological insulators. *Phys. Rev. B*, 86:045439, 2012.

[DSAHR11] S. Das Sarma, Shaffique Adam, E. H. Hwang, and Enrico Rossi. Electronic transport in two-dimensional graphene. *Rev. Mod. Phys.*, 83:407–470, May 2011.

[EBT+96] M. A. Eriksson, R. G. Beck, M. Topinka, J. A. Katine, R. M. Westervelt, K. L. Campman, and A. C. Gossard. Cryogenic scanning probe characterization of semiconductor nanostructures. *Appl. Phys. Lett.*, 69(5):671, 1996.

[EVT+14] Moritz Esslinger, Ralf Vogelgesang, Nahid Talebi, Worawut Khunsin, Pascal Gehring, Stefano de Zuani, Bruno Gompf, and Klaus Kern. Tetradymites as Natural Hyperbolic Materials for the Near-Infrared to Visible. *ACS Photonics*, 1(12):1285–1289, 2014.

[FAB+11] Zhe Fei, Gregory O Andreev, Wenzhong Bao, Lingfeng M Zhang, Alexander S McLeod, Chen Wang, Margaret K Stewart, Zeng Zhao, Gerardo Dominguez, Mark Thiemens, Michael M Fogler, Michael J Tauber, Antonio H Castro-Neto, Chun Ning Lau, Fritz Keilmann, and Dimitri N Basov. Infrared nanoscopy of Dirac plasmons at the graphene-SiO$_2$ interface. *Nano Lett.*, 11(11):4701–5, 2011.

[FKM07] Liang Fu, C. L. Kane, and E. J. Mele. Topological insulators in three dimensions. *Phys. Rev. Lett.*, 98:106803, Mar 2007.

[FNS07] M. M. Fogler, D. S. Novikov, and B. I. Shklovskii. Screening of a hypercritical charge in graphene. *Phys. Rev. B*, 76:233402, Dec 2007.

[FRA+12] Z Fei, A. S. Rodin, G O Andreev, W Bao, A. S. McLeod, M Wagner, L M Zhang, Z Zhao, M Thiemens, G Dominguez, M M Fogler, A. H Castro Neto, C N Lau, F Keilmann, and D N Basov. Gate-tuning of graphene plasmons revealed by infrared nano-imaging. *Nature*, 487(7405):82–5, 2012.

[FSW+07] T. Feurer, Nikolay S. Stoyanov, David W. Ward, Joshua C. Vaughan, Eric R. Statz, and Keith A. Nelson. Terahertz Polaritonics. *Ann. Rev. Mater. Res.*, 37(1):317–350, 2007.

[FZWL11] Zhen-Guo Fu, Ping Zhang, Zhigang Wang, and Shu-Shen Li. Multiple scattering theory of quasiparticles on a topological insulator surface. *Appl. Phys. Lett.*, 99(23):–, 2011.

[GdA14] F. Javier García de Abajo. Graphene Plasmonics: Challenges and Opportunities. *ACS Photon.*, 1(3):135–152, 2014.

[GG13]   A. K. Geim and I. V. Grigorieva. Van der waals heterostructures. *Nature*, 499(7459):419–425, Jul 2013. Perspectives.

[GH47]   F. Goos and H. Hänchen. Ein neuer und fundamentaler Versuch zur Totalreflexion. *Ann. Phys.*, 436(7-8):333–346, 1947.

[GKB⁺08]   G. Giovannetti, P. A. Khomyakov, G. Brocks, V. M. Karpan, J. van den Brink, and P. J. Kelly. Doping Graphene with Metal Contacts. *Phys. Rev. Lett.*, 101:026803, Jul 2008.

[GNJ12]   Y. Guo, C. L. Newman, W. Cortes, and Z. Jacob. Applications of hyperbolic metamaterial substrates. *Adv. OptoElectron.*, 2012:452502, 2012.

[Gor09]   R. V. Gorbachev. *Fabrication and transport properties of graphene-based nanostructures.* Ph.D. thesis, University of Exeter, Exeter, UK, 2009.

[GPN12]   A. N. Grigorenko, M. Polini, and K. S. Novoselov. Graphene plasmonics. *Nature Photon.*, 6(11):749–758, 2012.

[Gra00]   W. T. Grandy. *Scattering of Waves from Large Spheres.* Cambridge University Press, 2000.

[Gui08]   F. Guinea. Models of Electron Transport in Single Layer Graphene. *J. Low Temp. Phys.*, 153(5-6):359–373, October 2008.

[HA08]   Prabath Hewageegana and Vadym Apalkov. Electron localization in graphene quantum dots. *Phys. Rev. B*, 77:245426, Jun 2008.

[HBF13]   R. L. Heinisch, F. X. Bronold, and H. Fehske. Mie scattering analog in graphene: Lensing, particle confinement, and depletion of Klein tunneling. *Phys. Rev. B*, 87:155409, Apr 2013.

[HDS07]   E. H. Hwang and S. Das Sarma. Dielectric function, screening, and plasmons in two-dimensional graphene. *Phys. Rev. B*, 75:205418, 2007.

[HDS08]   E. H. Hwang and S. Das Sarma. Single-particle relaxation time versus transport scattering time in a two-dimensional graphene layer. *Phys. Rev. B*, 77:195412, May 2008.

[HDS09]   E. H. Hwang and S. Das Sarma. Plasmon modes of spatially separated double-layer graphene. *Phys. Rev. B*, 80:205405, 2009.

[HK10]   M. Z. Hasan and C. L. Kane. Colloquium. *Rev. Mod. Phys.*, 82:3045–3067, Nov 2010.

[HLMB11]   Felix Huerkamp, Tamara A. Leskova, Alexei A. Maradudin, and Björn Baumeier. The Goos-Hänchen effect for surface plasmon polaritons. *Opt. Expr.*, 19(16):15483–15489, 2011.

[HZZ09]   X. Hong, K. Zou, and J. Zhu. Quantum scattering time and its implications on scattering sources in graphene. *Phys. Rev. B*, 80:241415, Dec 2009.

[Jac14]   Zubin Jacob. Nanophotonics: Hyperbolic phonon-polaritons. *Nat. Mater.*, 13(12):1081–1083, 2014.

[JAN06]   Zubin Jacob, Leonid V. Alekseyev, and Evgenii Narimanov. Optical Hyperlens: Far-field imaging beyond the diffraction limit. *Opt. Express*, 14(18):8247–8256, 2006.

[JKHF+13] Dafei Jin, Anshuman Kumar, Kin Hung Fung, Jun Xu, and Nicholas X. Fang. Terahertz plasmonics in ferroelectric-gated graphene. *Appl. Phys. Lett.*, 102(20):201118, 2013.

[JZCN+]   B.-Y. Jiang, L. M. Zhang, A. H. Castro Neto, D. N. Basov, and M. M. Fogler. Generalized spectral method for near-field optical microscopy. arXiv:1503.00221.

[KGG09]   M. I. Katsnelson, F. Guinea, and A. K. Geim. Scattering of electrons in graphene by clusters of impurities. *Phys. Rev. B*, 79:195426, May 2009.

[KH04]   Fritz Keilmann and Rainer Hillenbrand. Near-field microscopy by elastic light scattering from a tip. *Phil. Trans. Roy. Soc. London, Ser. A*, 362(1817):787–805, 2004.

[KN07]   M.I. Katsnelson and K.S. Novoselov. Graphene: New bridge between condensed matter physics and quantum electrodynamics. *Solid State Commun.*, 143(1–2):3 – 13, 2007.

[KNG06]   M. I. Katsnelson, K. S. Novoselov, and A. K. Geim. Chiral tunnelling and the Klein paradox in graphene. *Nat. Phys.*, 2:620–625, 2006.

[LC14]   J. P. F. LeBlanc and J. P. Carbotte. Dielectric screening of surface states in a topological insulator. *Phys. Rev. B*, 89:035419, 2014.

[LDC+14]   Mingda Li, Zuyang Dai, Wenping Cui, Zhe Wang, Ferhat Katmis, Jiayue Wang, Peisi Le, Lijun Wu, and Yimei Zhu. Tunable THz surface plasmon polariton based on a topological insulator/layered superconductor hybrid structure. *Phys. Rev. B*, 89:235432, 2014.

[LFP+10]   A. D. LaForge, A. Frenzel, B. C. Pursley, Tao Lin, Xinfei Liu, Jing Shi, and D. N. Basov. Optical characterization of bi_2se_3 in a magnetic field: Infrared evidence for magnetoelectric coupling in a topological insulator material. *Phys. Rev. B*, 81:125120, 2010.

[LHRDS11]   Qiuzi Li, E. H. Hwang, E. Rossi, and S. Das Sarma. Theory of 2D Transport in Graphene for Correlated Disorder. *Phys. Rev. Lett.*, 107:156601, Oct 2011.

[LL75]   L. D. Landau and E. M. Lifshitz. *The Classical Theory of Fields*. Butterworth-Heinemann, 1975.

[LL77]   L. D. Landau and E. M. Lifshitz. *Quantum Mechanics*. Butterworth-Heinemann, 1977.

[LLK+15]   Peining Li, Martin Lewin, Andrey V. Kretinin, Joshua D. Caldwell, Kostya S. Novoselov, Takashi Taniguchi, Kenji Watanabe, Fabian Gaussmann, and Thomas Taubner. Hyperbolic phonon-polaritons in boron nitride for near-field optical imaging and focusing. *Nat. Comm.*, 6:7507, 2015.

[LLX+07]   Zhaowei Liu, Hyesog Lee, Yi Xiong, Cheng Sun, and Xiang Zhang. Far-field optical hyperlens magnifying sub-diffraction-limited objects. *Science*, 315(5819):1686, 2007.

[ManKanS14] A. Mreńca, K. Kolasiński, and B. Szafran. Imaging localization of quasibound states in graphene antidots. *Phys. Rev. B*, 90:035314, Jul 2014.

[MKG+14]   Alexander S. McLeod, P. Kelly, M. D. Goldflam, Z. Gainsforth, A. J. Westphal, Gerardo Dominguez, Mark H. Thiemens, Michael M. Fogler, and D. N. Basov. Model for quantitative tip-enhanced spectroscopy and the extraction of nanoscale-resolved optical constants. *Phys. Rev. B*, 90:085136, 2014.

[MMP11]   A. Matulis, M. Ramezani Masir, and F. M. Peeters. Application of optical beams to electrons in graphene. *Phys. Rev. B*, 83:115458, Mar 2011.

[MP86]   P. Muralt and D. W. Pohl. Scanning tunneling potentiometry. *Appl. Phys. Lett.*, 48(8):514–516, 1986.

[MP08]   A. Matulis and F. M. Peeters. Quasibound states of quantum dots in single and bilayer graphene. *Phys. Rev. B*, 77:115423, Mar 2008.

[NMCCN16]   K. S. Novoselov, A. Mishchenko, A. Carvalho, and A. H. Castro Neto. 2d materials and van der waals heterostructures. *Science*, 353(6298), 2016.

[Nus69]   H. M. Nussenzveig. High-Frequency Scattering by a Transparent Sphere. II. Theory of the Rainbow and the Glory. *J. Math. Phys.*, 10(1):125–176, 1969.

[NWW⁺15]   G. X. Ni, H. Wang, J. S. Wu, Z. Fei, M. D. Goldflam, F. Keilmann, B. Özyilmaz, A. H. Castro Neto, X. M. Xie, M. M. Fogler, and D. N. Basov. Plasmons in Graphene Moiré Superlattices. *Nat. Mat.*, XXX:In Press, 2015.

[OGM06]   P. M. Ostrovsky, I. V. Gornyi, and A. D. Mirlin. Electron transport in disordered graphene. *Phys. Rev. B*, 74:235443, Dec 2006.

[OSA⁺14]   Jun-Yu Ou, Jin-Kyu So, Giorgio Adamo, Azat Sulaev, Lan Wang, and Nikolay I. Zheludev. Ultraviolet and visible range plasmonics in the topological insulator $Bi_1.5Sb_{0.5}Te_{1.8}Se_{1.2}$. *Nat. Comm.*, 5:5139, 2014.

[PAPM12]   Rosario E. V. Profumo, Reza Asgari, Marco Polini, and A. H. MacDonald. Double-layer graphene and topological insulator thin-film plasmons. *Phys. Rev. B*, 85:085443, 2012.

[PCG⁺14]   Vincenzo Parente, Gabriele Campagnano, Domenico Giuliano, Arturo Tagliacozzo, and Francisco Guinea. Topological defects in topological insulators and bound states at topological superconductor vortices. *Materials*, 7(3):1652–1686, 2014.

[PCH⁺13]   K. W. Post, B. C. Chapler, Liang He, Xufeng Kou, Kang L. Wang, and D. N. Basov. Thickness-dependent bulk electronic properties in Bi_2Se_3 thin films revealed by infrared spectroscopy. *Phys. Rev. B*, 88:075121, 2013.

[PCL⁺15]   K. W. Post, B. C. Chapler, M. K. Liu, J. S. Wu, H. T. Stinson, M. D. Goldflam, A. R. Richardella, J. S. Lee, A. A. Reijnders, K. S. Burch, M. M. Fogler, N. Samarth, and D. N. Basov. Sum-rule constraints on the surface state conductance of topological insulators. *Phys. Rev. Lett.*, 115:116804, Sep 2015.

[Per10]   N. M. R. Peres. Colloquium. *Rev. Mod. Phys.*, 82:2673–2700, 2010.

[PIBK13]   Alexander Poddubny, Ivan Iorsh, Pavel Belov, and Yuri Kivshar. Hyperbolic metamaterials. *Nat. Photon.*, 7(12):948–957, 2013.

[PLV⁺11]   V. Parente, P. Lucignano, P. Vitale, A. Tagliacozzo, and F. Guinea. Spin connection and boundary states in a topological insulator. *Phys. Rev. B*, 83:075424, Feb 2011.

[QLX14]   Junjie Qi, Haiwen Liu, and X. C. Xie. Surface plasmon polaritons in topological insulators. *Phys. Rev. B*, 89:155420, 2014.

[QZ11]   Xiao-Liang Qi and Shou-Cheng Zhang. Topological insulators and superconductors. *Rev. Mod. Phys.*, 83(4):1057–1110, 2011.

[RCQZ10]   S. Raghu, Suk Bum Chung, Xiao-Liang Qi, and Shou-Cheng Zhang. Collective Modes of a Helical Liquid. *Phys. Rev. Lett.*, 104:116401, 2010.

[RKB77]   W. Richter, H. Köhler, and C. R. Becker. A Raman and far-infrared investigation of phonons in the rhombohedral V2VI3 compounds Bi_2Te_3, Bi_2Se_3, Sb_2Te_3 and $Bi_2(Te_{1-x}Se_x)_3$ $(0 < x < 1)$, $(Bi_{1-y}Sb_y)_2Te_3$ $(0 < y < 1)$. *Phys. Stat. Sol. (b)*, 84:619, 1977.

[RMMP11]   M. Ramezani Masir, A. Matulis, and F. M. Peeters. Scattering of dirac electrons by circular mass barriers: Valley filter and resonant scattering. *Phys. Rev. B*, 84:245413, Dec 2011.

[RMP13]   M. Ramezani Masir and F.M. Peeters. Scattering of dirac electrons by a random array of magnetic flux tubes. *J. Comput. Electronics*, 12(2):115–122, 2013.

[RMVP11]   M. Ramezani Masir, P. Vasilopoulos, and F. M. Peeters. Graphene in inhomogeneous magnetic fields: bound, quasi-bound and scattering states. *J. Phys.: Condens. Matter*, 23:315301, 2011.

[RTS+14]   Anjan A. Reijnders, Y. Tian, L. J. Sandilands, G. Pohl, I. D. Kivlichan, S. Y. Frank Zhao, S. Jia, M. E. Charles, R. J. Cava, Nasser Alidoust, Suyang Xu, Madhab Neupane, M. Zahid Hasan, X. Wang, S. W. Cheong, and K. S. Burch. Optical evidence of surface state suppression in Bi-based topological insulators. *Phys. Rev. B*, 89:075138, 2014.

[SBB+15]   Zhiwen Shi, Hans A. Bechtel, Samuel Berweger, Yinghui Sun, Bo Zeng, Chenhao Jin, Henry Chang, Michael C. Martin, Markus B. Raschke, and Feng Wang. Amplitude- and Phase-Resolved Nanospectral Imaging of Phonon Polaritons in Hexagonal Boron Nitride. *ACS Photon.*, 2(7):790–796, 2015.

[SE06]   Alessandro Salandrino and Nader Engheta. Far-field subdiffraction optical microscopy using metamaterial crystals: Theory and simulations. *Phys. Rev. B*, 74:075103, 2006.

[SETH13]   Robert Schütky, Christian Ertler, Andreas Trügler, and Ulrich Hohenester. Surface plasmons in doped topological insulators. *Phys. Rev. B*, 88:195311, 2013.

[SGM+07]   F. Schedin, A. K. Geim, S. V. Morozov, E. W. Hill, P. Blake, M. I. Katsnelson, and K. S. Novoselov. Detection of individual gas molecules adsorbed on graphene. *Nature Mater.*, 6:652, 2007.

[SGRBF15] Zhiyuan Sun, Á. Gutiérrez-Rubio, D. N. Basov, and M. M. Fogler. Hamiltonian Optics of Hyperbolic Polaritons in Nanogranules. *Nano Lett.*, 15(7):4455–4460, 2015.

[SGSB13] T. Stauber, G. Gómez-Santos, and L. Brey. Spin-charge separation of plasmonic excitations in thin topological insulators. *Phys. Rev. B*, 88:205427, 2013.

[SHP+11] H Sellier, B Hackens, M. G. Pala, F Martins, S Baltazar, X Wallart, L Desplanque, V Bayot, and S Huant. On the imaging of electron transport in semiconductor quantum structures by scanning-gate microscopy: successes and limitations. *Semicond. Sci. Technol.*, 26(6):064008, June 2011.

[SKL07] A. V. Shytov, M. I. Katsnelson, and L. S. Levitov. Atomic Collapse and Quasĭ Rydberg States in Graphene. *Phys. Rev. Lett.*, 99:246802, Dec 2007.

[SLZ14] Jingbo Sun, Natalia M. Litchinitser, and Ji Zhou. Indefinite by Nature: From Ultraviolet to Terahertz. *ACS Photon.*, 1(4):293–303, 2014.

[Sta14] Tobias Stauber. Plasmonics in Dirac systems: from graphene to topological insulators. *J. Phys.: Condens. Matter*, 26(12):123201, 2014.

[SWJ+14] H. T. Stinson, J. S. Wu, B. Y. Jiang, Z. Fei, A. S. Rodin, B. C. Chapler, A. S. McLeod, A. Castro Neto, Y. S. Lee, M. M. Fogler, and D. N. Basov. Infrared nanospectroscopy and imaging of collective superfluid excitations in anisotropic superconductors. *Phys. Rev. B*, 90:014502, 2014.

[TAT+13] E. Tiras, S. Ardali, T. Tiras, E. Arslan, S. Cakmakyapan, O. Kazar, J. Hassan, E. Janzén, and E. Ozbay. Effective mass of electron in monolayer graphene: Electron-phonon interaction. *J. Appl. Phys.*, 113(4):043708, 2013.

[TB71] T. Tamir and H. L. Bertoni. Lateral Displacement of Optical Beams at Multilayered and Periodic Structures. *J. Opt. Soc. Am.*, 61(10):1397–1413, 1971.

[TGP14] Andrea Tomadin, Francisco Guinea, and Marco Polini. Generation and morphing of plasmons in graphene superlattices. *Phys. Rev. B*, 90:161406, 2014.

[TLS+00] M. A. Topinka, B. J. LeRoy, S. E. J. Shaw, E. J. Heller, R. M. Westervelt, K. D. Maranowski, and A. C. Gossard. Imaging Coherent Electron Flow from a Quantum Point Contact. *Science*, 289(5488):2323–2326, 2000.

[TLW$^+$01]   M. A. Topinka, B. J. LeRoy, R. M. Westervelt, S. E. Shaw, R. Fleischmann, E. J. Heller, K. D. Maranowski, and A. C. Gossard. Coherent branched flow in a two-dimensional electron gas. *Nature*, 410(6825):183–6, March 2001.

[TO63]   T. Tamir and A.A. Oliner. The spectrum of electromagnetic waves guided by a plasma layer. *Proc. IEEE*, 51(2):317–332, Feb 1963.

[vdH57]   H. C. van de Hulst. *Light Scattering by Small Particles*. Courier Dover, Mineola, 1957.

[WBSB14]   T.O. Wehling, A.M. Black-Schaffer, and A.V. Balatsky. Dirac materials. *Advances in Physics*, 63(1):1–76, 2014.

[WBVA$^+$13]   Liang Wu, M. Brahlek, R. Valdés Aguilar, A. V. Stier, C. M. Morris, Y. Lubashevsky, L. S. Bilbro, N. Bansal, S. Oh, and N. P. Armitage. A sudden collapse in the transport lifetime across the topological phase transition in $(Bi_{1-x}In_x)_2Se_3$. *Nat. Phys.*, 9(7):410–414, 2013.

[WMRB13]   Weigang Wang, Ko Munakata, Michael Rozler, and Malcolm R. Beasley. Local Transport Measurements at Mesoscopic Length Scales Using Scanning Tunneling Potentiometry. *Phys. Rev. Lett.*, 110:236802, Jun 2013.

[WSSG06]   B Wunsch, T Stauber, F Sols, and F Guinea. Dynamical polarization of graphene at finite doping. *New J. Phys.*, 8(12):318–318, December 2006.

[YHL$^+$04]   Xiaobo Yin, Lambertus Hesselink, Zhaowei Liu, Nicholas Fang, and Xiang Zhang. Large positive and negative lateral optical beam displacements due to surface plasmon resonance. *Appl. Phys. Lett.*, 85(3):372–374, 2004.

[YM07]   Vladimir I. Yudson and Dmitrii L. Maslov. Universality in scattering by large-scale potential fluctuations in two-dimensional conductors. *Phys. Rev. B*, 75:241408, Jun 2007.

[ZAF$^+$12]   L. M. Zhang, G. O. Andreev, Z. Fei, A. S. McLeod, G. Dominguez, M. Thiemens, A. H. Castro-Neto, D. N. Basov, and M. M. Fogler. Near-field spectroscopy of silicon dioxide thin films. *Phys. Rev. B*, 85:075419, 2012.

[ZF08]   L. M. Zhang and M. M. Fogler. Nonlinear Screening and Ballistic Transport in a Graphene *p-n* Junction. *Phys. Rev. Lett.*, 100:116804, Mar 2008.